Transparent Flexible Electronics
By Directed Integration of Inorganic Micro and Nanomaterials

A DISSERTATION
SUBMITTED TO THE FACULTY OF THE GRADUATE SCHOOL
OF THE UNIVERSITY OF MINNESOTA
BY

Jesse J. Cole

IN PARTIAL FULFILLMENT OF THE REQUIREMENTS
FOR THE DEGREE OF
DOCTOR OF PHILOSOPHY

Advisor: Heiko O. Jacobs

June 2011

© Jesse J. Cole 2011

Acknowledgments

The pursuit of a PhD in Electrical Engineering at the University of Minnesota has been a great challenge over the past five years. I would not have been successful without considerable help and support. While I am thankful to everyone who has helped me through the unfamiliar concepts and the late nights of experiments, there are some specific individuals whose contributions have been particularly significant.

I thank my doctoral advisor Prof. Heiko O. Jacobs for guiding my research over the entirety of graduate school. I have learned a great deal from him even beyond my goals at the outset. First and foremost Heiko taught me how to conduct exploratory research in a professional setting. Heiko also continually challenged me by regularly looking at results from a unique perspective, through allowing me to present these results at conferences, and by offering unconventional experimental work-arounds.

I also thank my doctoral committee members Prof. Phil Cohen, Prof. Uwe Kortshagen, and Prof. Paul Ruden for their input. The access to such world-class faculty directly contributes to what makes the University of Minnesota a place to perform quality experimental research.

I acknowledge NSF-sponsored grants CMMI-0217538 (NanoXerography: The Use of Electrostatic Forces to Pattern Nanoparticles), CMMI-0556161 (Gas Phase NanoWire Integration Process), ECCS-0229087 (CAREER: Directed Assembly of Nanoparticles; A Tool to Enable the Fabrication of Nanoparticle Based Devices), CMMI-0621137 (GOALI: Nanowire Integration Process to Gain Control over Location, Dimension, and Orientation), and CMMI-0755995 (Gas Phase Nanoxerographic Nanomaterial Integration). These NSF-sponsored grants financial supported the reported results by addressing day-to-day costs including the consumable materials, system components, Nanofabrication Center use, and Characterization Facility access all of which were applied toward the experiments conducted during the course of this dissertation. I acknowledge limited nonsponsored funding from the McKnight Land-Grant Professorship program. Finally I acknowledge the Proto-IRG portion of the UMN MRSEC program (seed funding from grant 08616012) under the direction of Prof. Kortshagen which provided financial support as well.

I would also like to thank the UMN EE department for providing two semesters of Teaching Assistantships which both financially supported my research and also gave me valuable teaching experiences in undergraduate junior- and senior-level EE courses.

I would like to thank past and present Jacobs group members including Chad Barry, Xinyu Wang, Robert Knuesel, En-Chiang Lin, Chris Smith, Yu Chen, Shameek Bose, Sechul Park, Michael Motala, Jun Fang, and Forrest Johnson. Bouncing ideas off of interested coworkers has been an enjoyable part of my graduate career.

Lastly I thank my parents and my three younger brothers for their continued encouragement through the trials and tribulations of graduate research.

Abstract

This thesis focuses on nanomanufacturing processes for the heterogeneous integration of nanomaterials. Our approaches involved local adjustment of electrostatics at the surfaces to control material flux. Templating of surface electrostatics was implemented differently for three broad concepts resulting in control over nanomaterial synthesis, deposition, and printing. These three general concepts are:

(A) Tailored ZnO nanowire synthesis and integration out of the liquid phase
(B) Arc discharge synthesis and continuous nanocluster deposition from the gas phase
(C) Contact electrification and xerographic printing of nanoparticles from the gas phase

Concept (A): We report a method to fabricate and transfer crystalline ZnO with control over location, orientation, size, and shape. The process uses an oxygen plasma treatment in combination with a photoresist pattern on Magnesium-doped GaN substrates to define narrow nucleation regions and attachment points with 100 nanometer scale dimensions. Lateral epitaxial overgrowth follows nucleation to produce single crystalline ZnO which were fabricated into LEDs and photovoltaic cells.

Concept (B): We report a gas phase nanoparticle deposition system which shares characteristics with liquid phase electrodeposition. Clusters of charged nanoparticles selectively deposit onto electrically grounded surfaces. Similar to electroplating, the continued deposition of Au nanoparticles onto underlying resistive traces increased overall line conductivity. Alternatively, semiconducting ZnO and Ge nanomaterial sequentially deposited between interdigitated electrodes and served as addressable sensor active areas.

Concept (C): We report patterned transfer of charge between conformal material interfaces through a concept referred to as nanocontact electrification. Nanocontacts of different size and shape are formed between surface functionalized polydimethylsiloxane (PDMS) stamps and other dielectric materials (PMMA, SiO_2). Forced delamination and cleavage of the interface yields a well defined charge pattern with a minimal feature size of 100 nm. The process produces charged surfaces and associated fields that exceed the breakdown strength of air leading to strong long range adhesive forces and force distance curves which are recorded over macroscopic distances. The process is applied to fabricate charge patterned surfaces for nanoxerography demonstrating 200 nm resolution nanoparticle prints and applied to thin film electronics where the patterned charges are used to shift the threshold voltages of underlying transistors by over 500 mV.

Table of Contents

List of Figures

CHAPTER III

CHAPTER IV

CHAPTER V

CHAPTER VI

CHAPTER VII

CHAPTER VIII

Chapter I

Motivation, Background and Project Introductions

1.1 Motivation

Nanomaterials, the building blocks of future nanotechnological devices, are most commonly fabricated using solution chemistry or gas phase chemistry and can provide a variety of functions. The use of nanomaterials as building blocks, however, requires novel deposition methods to enable the creation of functional devices and systems. The primary objective of this thesis is to develop nanomanufacturing processes to synthesize and integrate inorganic nanomaterials with control over location, diameter, length, and geometrical orientation.

1.2 General Background

Metallic and inorganic semiconducting nanomaterials are considered key building blocks in the design of novel nanotechnological devices. Additive concepts are required to integrate, orient, and assemble such building blocks at desired locations. Today there are two classes of emerging techniques to deliver materials to desired locations on surfaces*:* Class 1 Nanocontacts and Printheads look at variances of ink-jet, microcontact, and dip-pen printing and use nanocontacts or print heads to deliver the materials. Concepts include scanning probes to print[1, 2] or manipulate[3] nanomaterials at the sub 100 nm length scale, semi-parallel inkjet based concepts[4, 5] to print materials from suspensions with 10 μm scale resolution, parallel nanotransfer methods[6, 7] to transfer nanomaterials from one substrate to another while retaining a copy of the order. Each of these concepts has advantages and disadvantages: Serial strategies lag in yield and speed. Parallel Nanotransfer and other Nano/Micro-Contact Printing concepts[6, 7] are suitable to transfer nanomaterials and molecules from one substrate to another, but do not offer a route to order or rearrange the materials as part of the printing/transfer process into arbitrary patterns. Class 2 Contact free "receptor" based methods use pre-patterned substrates and unordered materials. A vast variety of programmable or "receptor" based assembly concepts[8-18] that use unordered nanomaterials as an input have been

investigated in recent years. Typically the materials are suspended in solution and are assembled at desired locations (receptors) on a substrate using specific interactions. Most actively investigated areas currently use protein recognition[19, 20], DNA hybridization[9, 21, 22], hydrophobicity/hydrophilicity, surface tension and self-assembled monolayers[10], topography directed concepts[23-25], magnetic[11], dielectrophoretic assembly and transport[22, 26-28], and electrostatic forces [12-18, 25, 27].

Synthesis of Semiconducting Nanoparticles, Nanotubes, -wires, -belts and -ribbons. A variety of gas-phase processes have been developed to synthesize zero, one, and two dimensional semiconducting nanomaterials. Gas-phase processes are attractive due to high processing rates that can be achieved through direct gas-to-nanomaterial conversion. Most well established methods for nanoparticles use high temperature thermal reactions in furnace flow reactors [29-32], the decomposition of precursors through laser light irradiation [33], laser pyrolysis using high power infrared lasers [34-38], or thermal decomposition of precursors using thermal plasmas [39-51]. Similar CVD methods have been developed for the synthesis of one-dimensional and two dimensional semiconducting nanostructures in form of rods, tubes, wires, belts, and hexagons. Two well established methods are vapor-liquid-solid (VLS) and vapor-solid (VS) growth. Both VLS and VS processes involve wire/rod/tube formation from gaseous reactant species at a relatively high temperature using furnace flow reactors. Various semiconductor nanowires and nanorods, including SnO_2 [52], Ge [53], ZnO [54], and Ga_2O_3 [52] can be produced using this method using the same instrumentation.

High quality, single crystal semiconductor nanomaterials can also be produced using solution chemistry where the nucleation and growth is performed at low temperatures. For example, ZnO nanowires [55] and TiO_2 nanorods [56] have been synthesized by hydrothermal and sol-gel techniques, respectively.

Directed Self-Assembly -- The Key To Enable The Manufacturing of Existing Device Prototypes. The ability to assemble these materials in two and three dimensions will enable the mass fabrication of a whole range of novel devices. Examples of such devices are nanoparticle and nanowire based single electron transistors [57-59], single crystal

silicon nanoparticle based transistors [60] (in whose development we are involved), high mobility transistors on flexible substrates [61], resonant tunneling diodes [62], quantum-effect-based lasers [63, 64], photonic bandgap materials, filters, and wave-guides [65-67] to name a few.

Nanomaterial Integration Using Directed Self-Assembly and Nanotransfer. The use of nanoparticles and nanowires as building blocks requires novel assembling and integration strategies. We and others have begun to develop self-assembly and nanotransfer methods to integrate nanomaterials on surfaces. Most actively investigated areas use protein recognition [20], DNA hybridization [21], hydrophobicity/hydrophilicity [68], magnetic interactions [69] to assemble nanoparticles and hydrophobicity/ hydrophilicity [10], Langmuir Blodgett compression [70], electrospinning [71], and microfluidic patterning [72] to assemble nanorods in an aligned fashion.

1.3 ZnO Microcrystal Integration (Chapters III,IV)

To begin the present investigation into nanomaterial assembly it was necessary to choose a material system. ZnO is a promising material for exciton-based opto-electronic devices including light emitting (LED) and laser diodes due to its direct band gap of 3.3 eV at room temperature and a large exciton binding energy of 60 meV.[73-75] This large bandgap makes crystalline ZnO nearly transparent to the naked eye. Fabrication of LEDs based on ZnO homojunctions, however, has been challenging due to the lag of high quality p-doped ZnO. As a consequence there have been a number of reports on n-ZnO/p-GaN heterojunction LEDs. Most recent work has replaced the polycrystalline ZnO thin films[73, 76-78] with ZnO nanowires[74, 79, 80] to potentially benefit from the advantage of the nanowire properties - high crystallinity and fewer grain boundaries. Both forward[80] and reverse bias[79] electroluminescence (EL) was reported. The reverse bias emission was attributed to tunneling breakdown where hot carrier injection and recombination predominantly occurred in the GaN film[75]. Most of the previous devices including our own,[75] however, suffered from defect related emission around 585 nm under the desired forward bias operation. Integration of uniform arrays with control over the dimension and location of the single crystal nanowires has been another challenge that will have to be addressed to produce uniform devices over large areas.

A wet chemical approach is desired for reasons of processing cost when compared with gas-phase methods and a number of patterned and seeded growth methods have been reported. Patterned self-assembled monolayers with hydrophobic and hydrophilic endgroups have been used on silver[81] or silicon substrates[82] yielding densely packed 400nm diameter and 2μm long ZnO nanorods in regions that were 2μm wide with empty areas in between. Out-of-plane orientation varied but has been improved by seeding ZnO nanocrystals through thermal oxidation of zinc acetate.[83] Perfect vertical orientation, however, requires substrates such as GaN, MgAl2O4,[84] or Sapphire[85] which can be partially masked with photoresist to achieve patterned growth. Qualitatively all of these methods produced nanorods in the seeded or unmasked areas with limited control over the location and density on a single component basis. Dense films under continued growth eventually leads to coalescence into a polycrystalline film as the diameter increases with grain boundaries and defects in between. Attempts to reduce the defects have been made. The most successful approach used continued growth in combination with photoresist which can lead to a lateral overgrowth; a previously reported concept to produce high quality GaN thin films;[86] for ZnO on MgAl2O4, lateral growth over patterned photoresist improved the dislocation density by a factor of 100 compared to the window region containing coalesced nanorods.[84] Subsequent growth using a second window yielded continuous ZnO thin films with reduced dislocations.[85]

This thesis resulted in the liquid-phase growth of single crystalline ZnO with control over the dimensions (< 1 % STD) and location (0.7% STD pitch variation) yielding n-ZnO/p-GaN heterojunction arrays with uniform geometrical and optical properties. The process uses an oxygen plasma to surface engineer nucleation areas to produce single crystal ZnO disk type structures on p-type GaN at addressable locations on a surface with tailored >100nm lateral dimensions and sub-100nm lateral positional accuracy. The concept uses a plasma process and photoresist patterns to reveal non-oxidized magnesium sites that nucleate growth during hydrothermal growth at 90^{o}C. Nucleation in non-oxidized areas is followed by epitaxial overgrowth producing patterned areas of ZnO over 2 inch wafers. Adjusting pH increased ZnO deposition yield and enabled formation of high quality ZnO crystals. Transfer printing onto a flexible substrate is also demonstrated.ZnO/GaN micro-LEDs and UV photovoltaic cells were fabricated. The

LEDs possessed strong near band edge electroluminescent emission. Deep-level defect emission in the red and yellow is absent which implies that the ZnO microcrystals are of high quality. A hexagonal star like radiation pattern is observed which is explained by light emission through crystallographic facets.

1.4 Gas Phase Electrodeposition (Chapters V,VI)

Another powerful liquid phase synthesis technique remains traditional electrodeposition which has several unique characteristics absent from emerging direct write[87-89] or transfer techniques[90]. The most important being the ability to locally program the deposition of material (ions[91], nanoparticles[92, 93], and nanowires[94]) by simply applying a bias to an electrode. This characteristic supports programmable selected area deposition for materials and is presently limited to the liquid phase. The closest known gas phase extension to electrodeposition are electrostatic precipitators[95] which employ electrically biased plates to attract charged particles for filter applications.

A gas phase deposition system to deposit material into addressable areas forming vias, interconnects, patterned multimaterial or multilayer films in a programmable fashion had, however, not yet been reported. Such a deposition process would be important in the context of printable electronics since many functional nanomaterials are presently formed in the gas phase. The present thesis describes a system working at atmospheric pressure to form electrically interconnected nanostructured thin films with 60nm lateral resolution and predetermined thickness. The system uses a DC plasma arc discharge between two consumable electrodes as a material source. The use of a DC arc discharge between consumable electrodes is a known concept to produce charged nanomaterials in large quantities; DC arc discharge between graphite electrodes led to the discovery and industrial production of fullerenes and carbon nanotubes[96-99] and the concept has also been extended to produce GaN[100], Pd[101], and Si[102] clusters and particles to name a few.

This letter describes a new deposition system which combines an atmospheric pressure plasma with an electrodynamic deposition process to form nanostructures from sub 20 nm metallic or semiconducting nanoparticles. More specifically, the apparatus

uses a DC arc discharge between two consumable Au or Zn electrodes to continuously generate nanoparticles and a third sample electrode placed nearby for nanoparticle collection. The resist becomes highly charged resulting in the formation of localized electrodynamic nanolenses which focus nanoparticle deposition. The deposition process does not deplete the underlying charge pattern enabling the deposition of tall nanostructures (more than 100 monolayers). While the present paper is limited to two materials we anticipate that the process can be extended to any nanomaterial type that has been formed using high temperature plasma.

1.5 Contact Electrification (Chapters VII,VIII)

The role of surface electrostatics in gas phase electrodeposition later drove investigation of direct printing of surfaces charge to decouple surface charge levels from ions resulting from arc dynamics. The basic phenomenon of electrification by contact is well known and can be attributed to three fundamental processes: material transfer, ion transfer, or electron transfer. Electron transfer dominates if at least one of the materials is a semiconductor or a metal with free electrons.[103] If both materials are insulators, the fundamental charge transfer mechanism cannot be explained on the basis of electronegativity alone and requires the consideration of the chemical nature of all functional groups.[104] This becomes increasingly complicated if polymeric insulators are used. In all cases, contact electrification leads to uncompensated surface charges that impact the force of adhesion. For example, surface force apparatus measurements by Horn et al.[105] demonstrated that the electrostatic force of adhesion between crossed insulating cylinders can exceed 6 joules per m^2 which is comparable to the fracture energies of covalently bonded materials. We note that the reported values [105] were exceptionally large, exceeding anything that had been reported before and perhaps possible considering the breakdown strength of air. Considering the context of soft-lithography[106], nanoimprint lithography, and nanotransfer printing[107], the formation and fracture of conformal contacts have become mainstream and are no longer limited to single point contacts. This enables a new set of investigations into the fundamental science and applications of contact electrification over extended surfaces using multiple contacts of different size and shape.

As a first step in this direction we report on controlled delamination experiments between polydimethylsiloxane (PDMS) and other common dielectrics to quantify and monitor charge transfer and the subsequent electrostatic force of adhesion. In addition to the commonly used tables of electronegativity, we identified that proton exchange reactions established in solution chemistry provide the best approach to explain interfacial charging between the dielectrics that we investigated so far. The dielectrics include polymethyl methacrylate (PMMA), epoxy photoresist (SU-8), polystyrene (PS), polyacrylic acid (PAA), and silicon oxide (SiO_2). The magnitude of electrification can be adjusted through surface functionalization of the PDMS and reach values close to the physical limit near the dielectric breakdown strength of air. The uncompensated charges yield a long range electrostatic attractive force of 150 N/m2. Corresponding force distance curves show a phenomenological relationship between long and short range attractive forces where a controlled increase in the recorded long range electrostatic force equates to a stronger short range adhesion.

The gained knowledge finds several applications: in the context of laterally confined charge patterning with sub 100 nm lateral resolution, it extends previously reported serial scanning probe[16] and electric nanocontact charging techniques as it can pattern samples that are at least 100 times larger than what has been reported while maintaining the same high lateral resolution. Moreover previous[12, 14-16, 108] charging processes required a conducting substrate underneath the dielectric. The reported process eliminates this requirement as well as the requirement that an external voltage has to be applied to the sandwiched structures to inject and transfer charge at the interface. In the context of Nanoxerography, it is demonstrated that the chemically driven charge patterned surfaces prepared by nanocontact electrification can be developed into visible patterns using charge directed deposition of nanoparticles. In the context of transfer printing, it is demonstrated that the strong adhesive forces that stem from uncompensated surface charges can be used to transfer semiconducting components from one substrate to another whereby the size of the components can span 3 orders of magnitudes. Finally, in the context of printable electronics it is demonstrated that a contact with PDMS leads to high levels of uncompensated surface charge which affects transport in nearby semiconducting device layers which is measured in terms of transistor threshold voltage shifts which

exceeded 500mV in the MOSFET devices that have been tested. Threshold voltage shifts were found to depend on the covering material such that threshold voltage was adjusted positively (or negatively) after contacting SiO_2 (or PMMA) covering the n-channel FET.

Chapter II

Introductory Note

For the Set of Six Articles

As outlined in the abstract this thesis presents research results in three areas under the general schema of template electrostatic patterning of surfaces. The following chapters present six articles which are either already published or soon will be. To be specific Chapters III-VIII are reprints of articles published in peer-reviewed scientific articles. Where applicable, the supplemental information is included here as the last section in each chapter.

Chapters III and IV address tailored ZnO nanowire synthesis and integration out of the liquid phase. Chapters V and VI address arc discharge synthesis and continuous nanocluster deposition from the gas phase. Chapters VI and VIII address contact electrification and xerographic printing of nanoparticles from the gas phase.

Chapter III

Patterned Growth and Transfer of ZnO Micro and Nanocrystals with Size and Location Control

Jesse J. Cole, Xinyu Wang, Robert J. Knuesel, and Heiko O. Jacobs,

Reproduced with permission from:
Advanced Materials 20, 1474-1478 (2008)

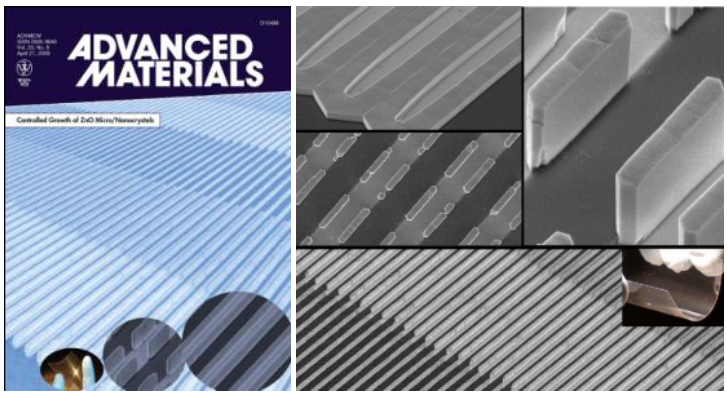

© 2011, WILEY-VCH Verlag GmbH & Co. KGaA, Weinheim.

3.1 Introduction

ZnO micro and nanostructures have been produced using a large number of different synthetic routes[109] and the applications that utilize the unique properties keep increasing. The 3.3eV direct bandgap and 60meV exciton binding energy is exploited in ultraviolet optoelectronics,[73-75] room temperature lasing,[54, 110-112] and solar cells applications;[113-115] extremely long photocarrier lifetimes have been observed yielding UV photodetectors with 10^8 internal gain; [116] the optical properties in combination with n-type conduction support transparent transistor and display applications[117, 118] while the piezoelectricity is utilized in power generation[119] and force sensing applications.[120] The integration of these device prototypes on a wafer scale will require access to ZnO micro and nanostructures with a variety of dimensions at known locations. A wet chemical approach is desired for reasons of processing cost when compared with gas-phase methods and a number of patterned and seeded growth methods have been reported. Patterned self-assembled monolayers with hydrophobic and hydrophilic endgroups have been used silver[81] or silicon substrates[82] yielding densely packed 400nm diameter and 2μm long ZnO nanorods in regions that were 2μm wide with empty areas in between. Out-of-plane orientation varied but has been improved by seeding ZnO nanocrystals through thermal oxidation of zinc acetate.[83] Perfect vertical orientation, however, requires substrates such as GaN, $MgAl_2O_4$,[84] or Sapphire[85] which can be partially masked with photoresist to achieve patterned growth. Qualitatively all of these methods produce nanorods in the seeded or unmasked areas with limited control over the location and density. Continued growth leads to coalescence into a polycrystalline film as the diameter increases with grain boundaries and defects in between. Continued growth in combination with photoresist has also been reported to lead to a lateral overgrowth; a previously reported concept to produce high quality GaN thin films.[86] For ZnO on $MgAl_2O_4$, lateral growth over patterned photoresist improved the dislocation density by a factor of 100 compared to the window region containing coalesced nanorods.[84] Subsequent growth using a second window yielded continuous ZnO thin films with reduced dislocations.[85]

This Communication reports on a new method using oxygen plasma to surface engineer nucleation areas to produce vertical single crystal ZnO nanowire rows and extended wall structures on p-type GaN at addressable locations on a surface with tailored >100nm lateral dimensions and <100 nm lateral positional accuracy. The concept uses a plasma process and photoresist patterns to reveal non-oxidized magnesium sites that nucleate growth. Nucleation in non-oxidized areas is followed by epitaxial overgrowth producing patterned areas of ZnO over 2 inch wafers. Adjusting pH increased ZnO deposition yield and enabled formation of high quality ZnO crystals. Transfer printing onto a flexible substrate is also demonstrated.

3.2 Results and Discussion

Figure 3-1 shows the patterned growth process. Photolithography, oxygen plasma treatment, and solution-based growth are the basic process steps to produce ZnO micro and nanocrystals at exact locations on a surface. The oxygen plasma is used to oxidize Mg dopands to inhibit nucleation and growth in the center area while it etches the resist leaving behind a transitional region to nucleate ZnO growth. Subsequent lateral epitaxial overgrowth yields ZnO structures that are larger in diameter than the initial nucleation region. A Novolac-based resist (Fig. 3-1A) is patterned on a Mg-doped GaN surface (Fig. 3-1B) by standard photolithography, as described in the experimental section. The patterns can directly be used for growth leading to a polycrystalline ZnO film in the exposed GaN areas which shows that the basic developer containing sodium hydroxide and exposure to photoresist do not adversely affect ZnO nucleation on p-type GaN. However, to produce single crystal structures of high quality a plasma treatment is required (Fig. 3-1C). The treatment yields a narrow nucleation region where the oxidation state transitions from fully oxygen passivated to partially and non-oxidized while it removes organic residues on the GaN surface which is required to accomplish uniform growth over the entire wafer (see Experimental section for Additional Transition Region Information). We optimized this process and exposure to a 100-watt, 100 mTorr oxygen plasma for 30 seconds worked best to completely prevent nucleation on fully oxygen passivated Mg-doped GaN. The growth of ZnO (Fig. 3-1D) is carried out in a glass vial following a previously published procedure[81] using zinc acetate and hexamine as

described in the experimental section. The only parameter that was modified was the initial pH. We found that the initial pH of the growth solution is an important additional parameter to control. The glass vial initially contained deionized water at pH 5.5; the slightly acidic nature is attributed to CO_2 absorption from the ambient environment. It was necessary to increase the initial pH to 7.5 by adding small amounts of ammonium hydroxide, NH_4OH, to form continuous extended single crystals.

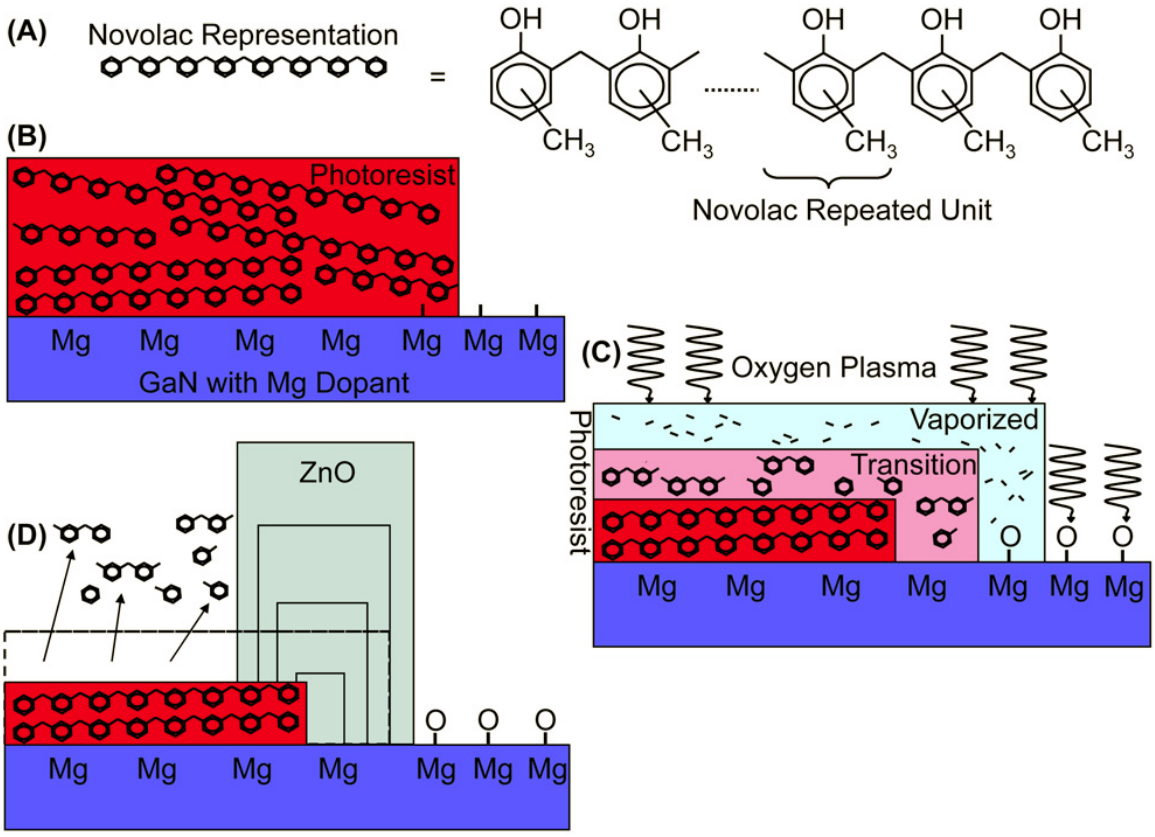

Figure 3-1. *Process steps for producing ZnO crystals through nucleation at the photoresist-GaN interface. (A) Conventionally patterned Novolac-based photoresist on (B) Mg-doped GaN is exposed to an (C) oxygen plasma to deactivate Mg dopands that otherwise act as nucleation sites as well as to produce a transitional region which contains non-oxidized Mg to nucleate growth. (D) Solution growth at different pH and growth time yields individual, and merged laterally overgrown ZnO structures.*

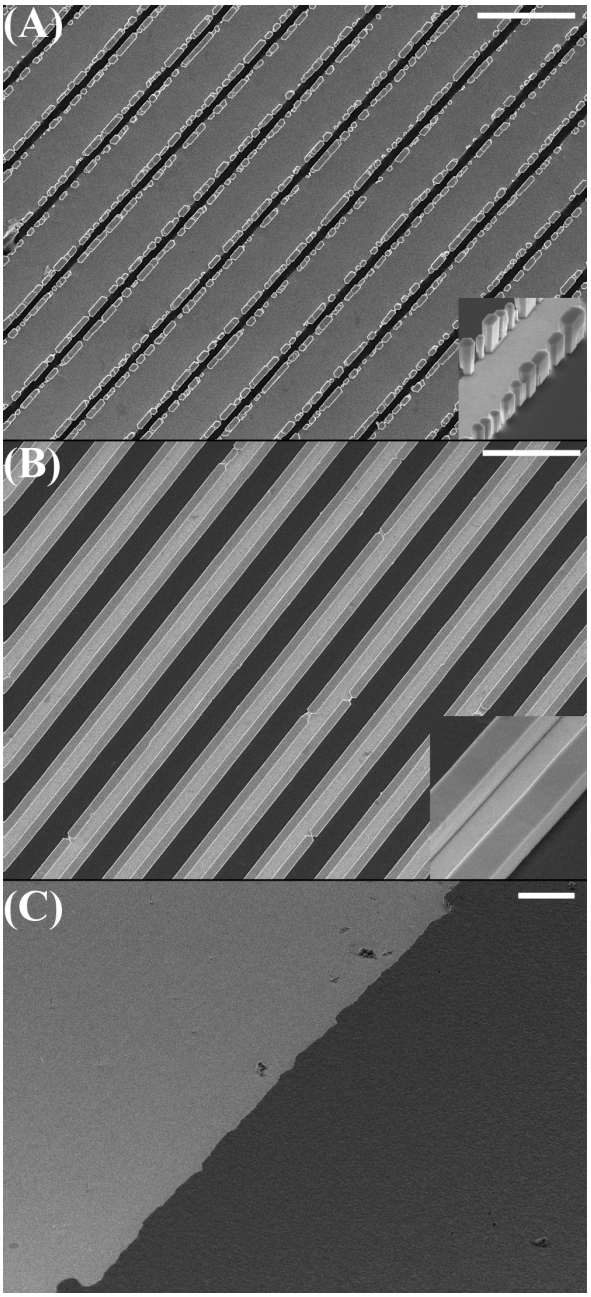

Figure 3-2. *Patterned integration of ZnO structures through passivation/activation of Mg nucleation sites on GaN substrates. (A) Isolated nanorods or (B) extended single crystals form at the GaN-photoresist interface when the initial pH is 5.5 or 7.5, respectively. (C) Control experiment depicting step edge and complete suppression of growth in oxygen plasma treated regions (light) and uniform growth in the Mg doped area (dark). 10 μm scale bars.*

Figure 3-2 shows representative images of ZnO structures that form at the plasma activated interface; with an increase in pH from 5.5 to 7.5 the crystals transition from individual ZnO nanorods (Fig. 3-2A) to single crystal lines with a rectangular 1 μm wide and 0.8 μm tall cross section (Fig. 3-2B). Independent of the pH no nucleation and growth is observed on either the photoresist or the GaN that was fully oxidized. The presence of Mg dopant is the key to accomplish the observed localized nucleation in some areas and passivation in others. A number of control experiments have been carried out which support this claim. First, we were not able to produce single crystals with high dimensional control on undoped and n-doped ($5x10^{17}$ cm^{-3} Si) GaN samples in concurrent growth experiments (90 minutes, 90°C, 25mM zinc acetate, 25 mM hexamethylenetetramine, initial pH 7.5) with p-doped ($5x10^{18}$ cm^{-3} Mg) GaN control substrates. The undoped and n-type samples produced ZnO structures with uncontrolled nucleation sites. While we did find that ZnO could be hydrothermally grown on undoped and n-type GaN, this ZnO deposition was minimal and potentially related to surface contamination. Second, complete deactivation of the nucleation sites through oxygen plasma treatment was only observed using Mg doped substrates. We also found that the photolithographic process was not the primary cause of the suppressed growth in exposed regions. As a control experiment we partially covered the bare p-type GaN using a glass slide to produce a partially oxidized surface using the oxygen plasma and observed that subsequent growth revealed a 1.5μm-thick continuous polycrystalline ZnO film in the non-oxidized areas, and no ZnO in the area that was fully exposed to the plasma.

The observation of the increased nucleation in the magnesium rich areas can be explained by looking at the electronegativity: Magnesium is an alkaline earth metal that exhibits greater ionic characteristics and lower electronegativity than the group III element gallium. Mg-O (oxygen electronegativity: 3.5) is more energetically stable than Mg-N (nitrogen electronegativity: 3.1). The enhanced ionic characteristic of Magnesium within the GaN lattice should lead to an enhanced concentration and attachment of precursor ions such as OH^-, Zn^{2+}, and their complexes. The affinity of OH^- and subsequent localized decomposition of $Zn(OH)_2$ is expected to lead to a preferential nucleation and growth in the Mg-rich region. Second, plasma oxidized Mg sites should suppress OH^- attachment and nucleation in areas towards the center of exposed GaN.

This is consistent with the experiment and most likely the reason of the high selectivity in the growth that we observed. It is possible for MgO to adsorb OH^- and also for isolated MgO site behavior to vary from bulk behavior. However the point of zero charge for bulk MgO is widely accepted as 12 and implies that MgO preferentially adsorbs H^+ for the experimental pH range described here. Considering the MgO point of zero charge, we speculate that ZnO nucleation on oxidized Mg locations may be possible if growth pH is held above pH 12. In summary, Mg sites are active and readily oxidized. Non-oxidized Mg sites nucleate growth whereas the formation of an ionic Mg-O bond through plasma oxidation deactivates nucleation. Once nucleation has occurred and facets are produced the ZnO growth continues independent of the substrate. In other words the presence of the substrate is no longer relevant and growth does not deviate from conventional ZnO hydrothermal deposition. For example, HMT increases the aspect ratio but does not completely stop lateral growth. With an initial pH of 7.5 and assuming that ZnO growth occurs immediately upon immersion in the growth solution, the growth rate can be estimated at 2.8Å/second along the c-axis and 0.8Å/second along the a- or b-axis crystallographic direction.

Figure 3-3 shows a set of ZnO wall and interdigitated electrode type structures formed using a two step lithography/oxidation sequence to illustrate that lithographic processing does not adversely affect previously oxidized nucleation sites. Oxidized areas can be formed using a sequence of sequential masking and oxidation steps yielding more complex patterns. The first sequence used photolithography, plasma oxidation, and removal of resist to produce parallel lines of fully oxidized GaN. Next we repeated the process whereby the photoresist pattern crosses the original pattern at controlled angles; the wall structures (Figs. 3A,B) had an angle of 90°, and the interdigitated electrode structures (Figs. 3C) had an angle of roughly 1° between the initial oxidized GaN strips and final photoresist trenches; the resist is not removed during the second step to yield narrow nucleation regions and illustrated structures.

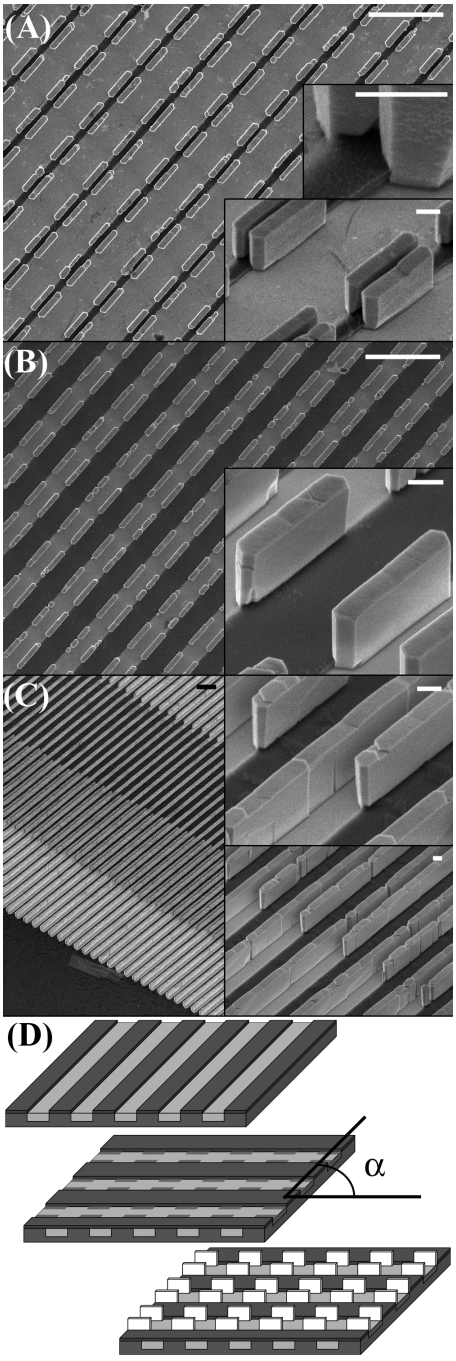

Figure 3-3. *ZnO structures fabricated by multiple oxidation steps. Angle between initially oxidized GaN strips and final ZnO nucleation strips was varied from 90° (A,B) to approximately 1° (C), resulting in walls and interdigitated electrode type structures, respectively. Increasing the angle α between first (D top) and second (D middle) oxidation steps decreased lengths of the resulting ZnO crystals (D bottom). 10 μm scale bars in (A,B,C). 1 μm scale bars in insets.*

Using the photomasks the structures can be placed with ~100 nm nearest-neighbor positional accuracy calculated by measuring the center-to-center distance (90 nm STD, Figure 2B; 120 nm STD, Figure 3A) of the ZnO crystals that have been produced The use of higher resolution e-beam patterns could reduce these numbers. Lateral overgrowth leads to well defined crystals with a narrow size distribution. We measured a variation of 60 nm or smaller (5% STD) considering the lateral width perpendicular to photoresist barrier (Fig. 2B, 3A). This confinement was not as narrow using the oxide-only-barrier; walls limited to 5 μm (Fig. 3A) in the longitudinal direction using an oxide-only-barrier varied by 80 nm (1.4% STD).

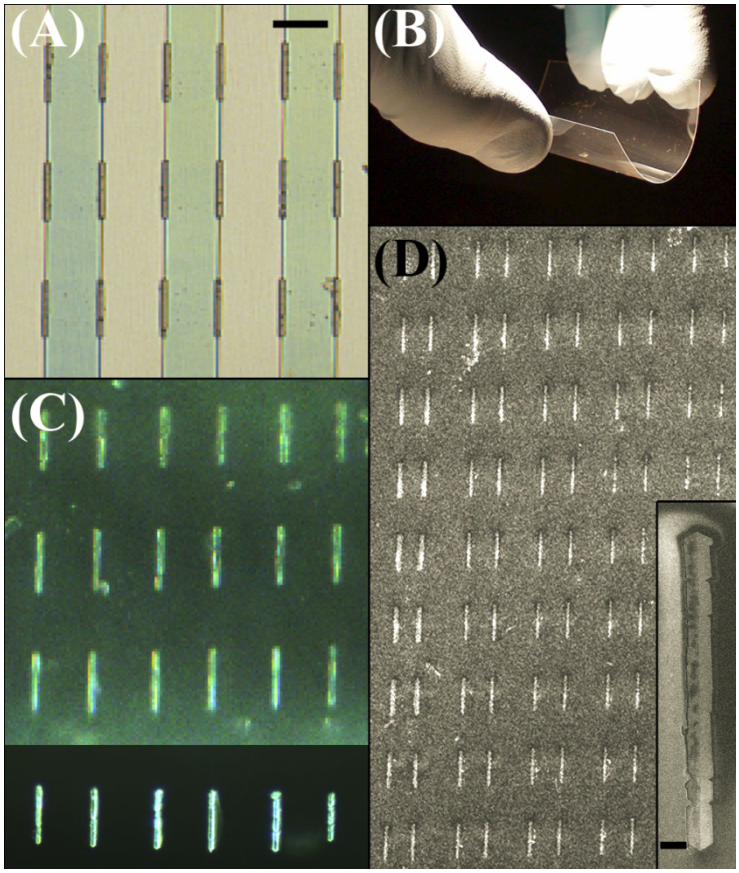

Figure 3-4. *ZnO transfer to a flexible substrate. Fabricated ZnO prior (A) and after transfer (B-D) onto a 200μm thick epoxy-PET flexible substrate. Dark field (C), fluorescence (C, inset), and SEM (D) micrographs of ZnO epoxy composite structure after transfer. 25μm scale bar in (A). 2μm scale bar in (D inset).*

The size and area of the attachment points to GaN can be a fraction of the overall ZnO crystal size. The inset of Fig 3-3A shows the trunk of the produced structures; approximately 50% of the footprint sits on the photoresist in this case. This allows detachment and transfer of overgrown ZnO crystals to flexible substrates through interfacial cleavage/delamination at the ZnO/GaN interface. Figure 3-4 shows a first example transferring a 10x10 array of 25 μm long and 2 μm wide crystals onto an epoxy thin film. We supported the ZnO structures prior transfer by spin-coating a 10μm thin layer of SU-8 2010 onto the structure (2500 RPM, 95^{o}C/120s soft-bake, 20s UV exposure, and 95^{o}C/120s hard bake). The use of a low viscosity SU-8 solution helped to form a conformal initial coating. Subsequently we applied a second 200 μm thick layer (100 RPM, 95^{o}C/300s soft-bake, 120s UV exposure, and 95^{o}C/1h hard bake) to produce a film with sufficient mechanical strength. The entire epoxy film (Fig. 3-4A) including the ZnO can be delaminated through rapid thermal cooling induced stress by placing the sample on an unheated copper plate at the end of the final hard bake cycle. The film tends to curl and was further attached to a polyethylene terephthalate (PET) film to characterize the flexible and optically transparent ZnO and SU-8 composite structure (Fig. 3-4B,C,D).

3.3 Conclusion

The reported nucleation and growth process provides a new route towards the production of ZnO micro and nanostructures at known locations (~100nm-STD) with well defined dimensions (4%-STD). The resulting structures are attractive for a number of applications that aim at integrating ZnO devices such as ultraviolet LEDs[73-75], laser cavities[121], waveguides[54, 110-112], high gain photodetectors[116], solar cells[113-115], sensors, piezoelectric actuators[120] or micro-power generators[119] at exact known locations. A first step towards the transfer of the structures onto flexible substrates has been made. Measurements of the electrical and optical properties are underway and will be published elsewhere.

3.4 Experimental

Photoresist Patterning: Mg-doped GaN was used as a substrate, with doping concentration $5x10^{18}$ cm^{-3}, TDI inc., Silver Spring, MD. The substrate was photolithographically patterned conventionally. Following a dehydration prebake at 115°C for 60 seconds, Shipley 1805 photoresist was spun at 3000 RPM, soft-baked at 105°C for 60 seconds, exposed using a Karl Suss MA-6 Mask Aligner, and developed in Microposit 351 developer for 30 seconds. Shipley 1805 is a Novolac-based photoresist that can require descum processing after patterning. The only descum process used here was exposure to the oxygen plasma, which also provided a means for ZnO nucleation control.

ZnO Crystal Synthesis: The ZnO growth solution was prepared by adding zinc acetate, $Zn(CH_3COO)_2$, and hexamine, $(CH_2)_6N_4$, to 70 mL of deionized water such that the solution contained 25mM of each compound. The pH was adjusted by adding ammonium hydroxide, NH_4OH, to the initially acidic solution and checked in real time with an electronic pH probe. The probe was removed to prevent unwanted pH probe electrolyte solution from leaking into the growth solution. Patterned and oxidized GaN samples were inserted into the growth solution. To grow the ZnO crystals, the solution was heated in an oven to 90°C for times ranging between 10 minutes to 3 hours. GaN samples were held in the growth solution with glass slides, because metal clips were corroded by the growth solution, reducing uniformity in ZnO deposition. Following the growth, samples were removed from solution and briefly rinsed with DI water.

Additional Transition Region Information: The transitional region consists of a gradient of Mg dopand sites which were partially shielded from the oxidative effects of the plasma, yet permits ZnO to deposit in solution. The oxygen plasma etching of photoresist is widely used in industry and has been successfully modeled by the Hougen-Watson method as the ion-assisted chemical etch of Novolac polymer chains by oxygen radicals. Oxygen radicals impact and react with the photoresist to break covalent C-C bonds (3.6 eV per bond) to separate the original polymer chains and/or remove some material as volatile products such as CO_x and H_2. Oxygen plasma etching results from breakage of carbon bonds responsible for chain cohesion, then atomization of shortened chain constituents to expose unreacted long photoresist chains below. The process can be

interrupted, which leaves a transitional region that includes a photoresist layer with shortened polymer chains and substrate surface region that transitions from "no" to "full" oxygen plasma exposure. We have conducted oxygen plasma etching experiments which support the model. Photoresist was patterned on a substrate, then half of the substrate was covered with a glass slide. The substrate was exposed to oxygen plasma, such that slide-covered areas were protected from plasma exposure. Exposure to oxygen plasma was found to cause lateral etching of the photoresist. The lateral photoresist etch rate was experimentally determined as 125nm/min. The reaction time required to vaporize the photoresist implies that a sub-100nm transition region forms at the point where photoresist chains transition from initial polymer chain length to shortened volatile hydrocarbons.

Chapter IV

Integration of ZnO Microcrystals with Tailored Dimensions Forming Light Emitting Diodes and UV Photovoltaic Cells

Jesse J. Cole, Xinyu Wang, Robert J. Knuesel and Heiko O. Jacobs,

Reproduced with permission from:

Nano Letters 8(5), (1477-1481) (2008)

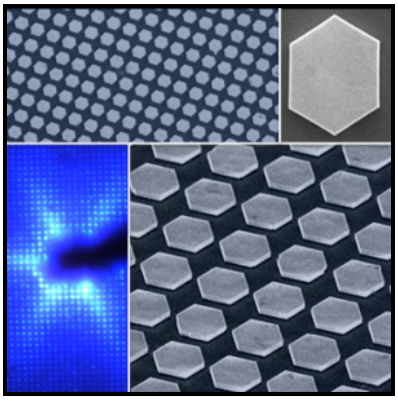

© 2011 American Chemical Society

4.1 Introduction

ZnO is a promising material for exciton-based opto-electronic devices including light emitting (LED) and laser diodes due to its direct band gap of 3.3 eV at room temperature and a large exciton binding energy of 60 meV.[73-75] Fabrication of LEDs based on ZnO homojunctions, however, has been challenging due to the lag of high quality p-doped ZnO. As a consequence there have been a number of reports on n-ZnO/p-GaN heterojunction LEDs. Most recent work has replaced the polycrystalline ZnO thin films[73, 76-78] with ZnO nanowires[74, 79, 80] to potentially benefit from the advantage of the nanowire properties - high crystallinity and fewer grain boundaries. Both forward[80] and reverse bias[79] electroluminescence (EL) was reported. The reverse bias emission was attributed to tunneling breakdown where hot carrier injection and recombination predominantly occurred in the GaN film[75]. Most of the previous devices including our own,[75] however, suffered from defect related emission around 585 nm under the desired forward bias operation. Integration of uniform arrays with control over the dimension and location of the single crystal nanowires has been another challenge that will have to be addressed to produce uniform devices over large areas. A wet chemical approach is desired for reasons of processing cost when compared with gas-phase methods and a number of patterned and seeded growth methods have been reported. Patterned self-assembled monolayers with hydrophobic and hydrophilic endgroups have been used on silver[81] or silicon substrates[82] yielding densely packed 400nm diameter and 2μm long ZnO nanorods in regions that were 2μm wide with empty areas in between. Out-of-plane orientation varied but has been improved by seeding ZnO nanocrystals through thermal oxidation of zinc acetate.[83] Perfect vertical orientation, however, requires substrates such as GaN, $MgAl_2O_4$,[84] or Sapphire[85] which can be partially masked with photoresist to achieve patterned growth. Qualitatively all of these methods produced nanorods in the seeded or unmasked areas with limited control over the location and density on a single component basis. Dense films under continued growth eventually leads to coalescence into a polycrystalline film as the diameter increases with grain boundaries and defects in between. Attempts to reduce the defects have been made. The most successful approach used continued growth in combination with photoresist which can lead to a lateral overgrowth; a previously reported concept to

produce high quality GaN thin films;[86] for ZnO on $MgAl_2O_4$, lateral growth over patterned photoresist improved the dislocation density by a factor of 100 compared to the window region containing coalesced nanorods.[84] Subsequent growth using a second window yielded continuous ZnO thin films with reduced dislocations.[85]

This Letter reports the growth of single crystals ZnO with control over the dimensions (< 1 % STD) and location (0.7% STD pitch variation) yielding n-ZnO/p-GaN heterojunction arrays with uniform geometrical and optical properties. The process uses an oxygen plasma to surface engineer nucleation areas to produce single crystal ZnO disk type structures on p-type GaN at addressable locations on a surface with tailored >100nm lateral dimensions and sub-100nm lateral positional accuracy. The concept uses a plasma process and photoresist patterns to reveal non-oxidized magnesium sites that nucleate growth during hydrothermal growth at 90^oC. Nucleation in non-oxidized areas is followed by epitaxial overgrowth producing patterned areas of ZnO over 2 inch wafers. ZnO/GaN micro-LEDs and UV photovoltaic cells were fabricated. The LEDs possessed strong near band edge electroluminescent emission. Deep-level defect emission in the red and yellow is absent which implies that the ZnO microcrystals are of high quality. A hexagonal star like radiation pattern is observed which is explained by light emission through crystallographic facets.

4.2 Results and Discussion

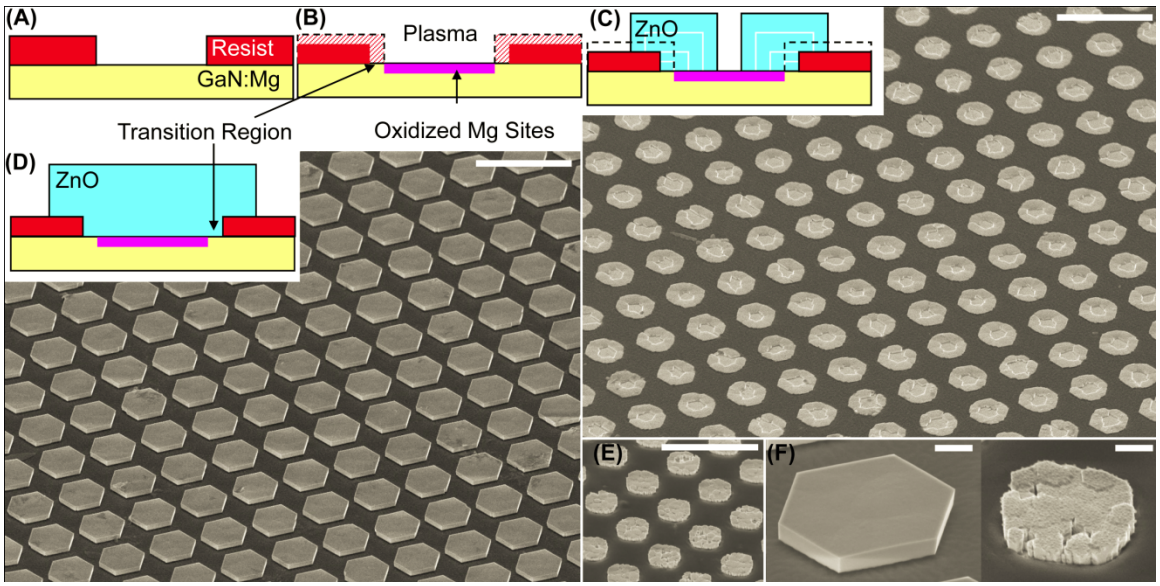

Figure 4-1. *Procedure and results of controlled ZnO microcrystal nucleation and growth involving oxygen plasma treatment. (A) Conventionally patterned photoresist on Mg-doped GaN is exposed to (B) an oxygen plasma to deactivate Mg dopants that otherwise act as nucleation sites. The process produces a transitional region which contains non-oxidized Mg to nucleate growth. Solution growth forms rings (C) that merged into well defined continuous ZnO microcrystals under continuous growth (D). Control experiments without oxygen plasma treatment (E) yield polycrystalline ZnO with grain boundaries and pinhole defects. High magnification SEM images shows a side-by-side comparison of topology difference between plasma-treated (F left) and control samples (F right). 10μm scale bars in (A)-(E), 1 μm scale bars in (F). SEM images taken at 45 degree tilt.*

Figure 1 shows the patterned growth process and the resulting ZnO crystals. Photolithography, oxygen plasma treatment, and solution-based growth are the basic process steps to produce ZnO crystals at exact locations on a surface. The patterned surface (Fig. 4-1A) is formed on a Mg-doped GaN substrate, doping concentration $5x10^{18}$ cm^{-3}, TDI inc., Silver Spring, MD. Following a prebake at 115°C for 60 seconds, Shipley 1805 photoresist was spun at 3000 RPM, soft-baked at 105°C for 60 seconds, exposed using a Karl Suss MA-6 Mask Aligner, and developed in Microposit 351 developer for 30 seconds. The patterns can directly be used for growth leading to a polycrystalline ZnO

film in the exposed GaN areas which shows that the basic developer containing sodium hydroxide and exposure to photoresist do not adversely affect ZnO nucleation on p-type GaN. However, to transition from polycrystalline to the illustrated single crystal structures plasma treatment was found to be the key (Fig. 4-1B). The treatment yields a nucleation region (Fig. 4-1C inset) at the GaN/Photoresist interface. ZnO deposited initially in the ring-shaped regions (Fig. 4-1C), then merged by lateral overgrowth over a longer growth time of 3 hours to become the well-faceted hexagonal crystals (Fig. 4-1D). The current understanding of the process involves the Mg dopant, which is the least electronegative atom within the GaN matrix. Non-oxidized Mg is expected to have an affinity to OH^- which reacts with Zn^{2+} to form ZnO during hydrothermal growth. The oxygen plasma however, reduces this affinity as Mg becomes oxidized. The transitional region is formed as the resist is partially etched away by the plasma process. This process leaves behind a gradient where the level of oxidation is reduced from fully to non-oxidized that nucleates ZnO growth. This hypothesis is consistent with other control experiments; oxygen plasma treated Mg doped GaN test samples for example did not nucleate growth under the same growth conditions. We optimized this process and exposure to a 100-watt, 100 mTorr oxygen plasma for 30 seconds was used to produce the illustrated structures. Nucleation in the transition region is followed by lateral epitaxial overgrowth. All growth experiments were carried out in a glass vial following a previously published procedure.[81] In short, growth is initiated by adding zinc acetate, $Zn(CH_3COO)_2$, and hexamine, $(CH_2)_6N_4$, to 70 mL of deionized water such that the solution contained 25mM of each compound. To grow the ZnO crystals, the solution was heated in an oven to 90°C for times ranging between 10 minutes to 3 hours. Following the growth, samples were removed from solution and briefly rinsed with DI water. While this is the basic process we found that the initial pH of the growth solution is an important additional parameter required for high quality crystals. It was necessary to increase the initial pH from 5.5 to 7.5 by adding small amounts of ammonium hydroxide, NH_4OH. The illustrated example used a photoresist pattern with 3μm diameter circular openings and 6μm center-to-center spacing, and 3 hours growth time to produce the well-faceted hexagonal crystals. The largest interior dimensions of the hexagonal crystals were 4μm, indicating that ZnO laterally overgrew the photoresist hole by approximately

0.5μm. Lateral overgrowth occurred over the oxidized GaN as well, such that ZnO filled the photoresist holes to completely cover the GaN surface. Using the photomasks the structures can be placed with a positional accuracy (40 nm STD for 6 um pitch = 0.7%) calculated by measuring the center-to-center distance between the ZnO crystals that have been produced. The size distribution was smaller than 1% (STD).

Inspection of Figure 1D, Figure 4-1F (left) and other samples shows minimal pinhole defects per area of oxygen-plasma treated ZnO crystal. Non-oxygen plasma treated control samples (Fig. 4-1E) and (Fig. 4-1F, right) show significant numbers of pinhole defects and grain boundaries. More images of control samples are provided in the Supplemental Material. Supplemental Figure 4-S1 is a top-down SEM image of an oxygen plasma treated sample where the growth was terminated prior to completion yielding a single pinhole that is located in the center of each crystal. The control sample (Figure 4-S2) without plasma treatment depicts randomly distributed pinhole defects and regions that resemble the morphology of a polycrystalline film. The average number of pinholes and grain boundaries is at least a factor of 10 larger for the non-plasma treated samples where the growth starts randomly in the open areas.

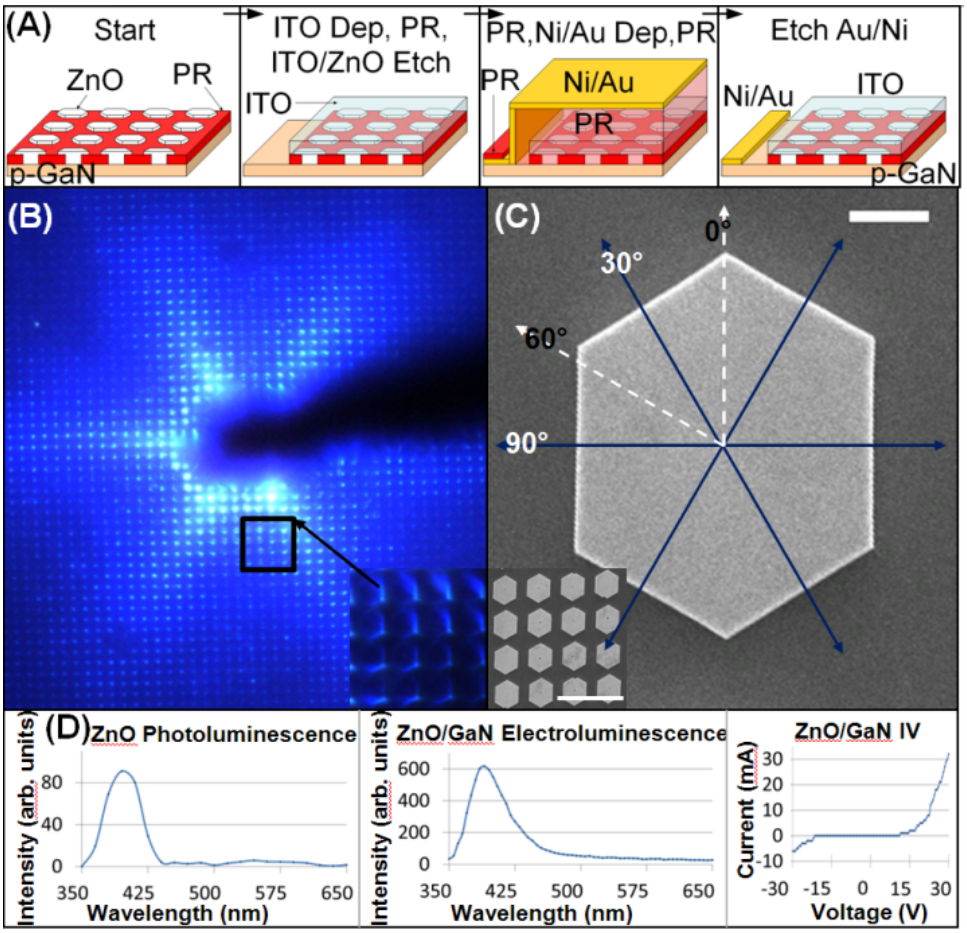

74

Figure 4-2. *Fabrication and characterization of ZnO microcrystal heterojunction n-ZnO/p-GaN ultraviolet LED. (A) Processing Steps. (B) Forward bias emission revealing a six-pointed star which is attributed to facet-to-facet (B inset, C inset) hexagonal propagation with reduced coupling along the 0° and 60° directions (C). (D) Photoluminescence spectrum of the ZnO, forward bias LED electroluminescence spectrum, and LED IV curve show near-band-edge emission at 3.19eV and absence of defect peaks in the wavelength range 450 to 650nm. 1μm scale bar in C. 10 μm scale bar in C inset.*

Figure 4-2 shows an array of ultraviolet heterojunction n-ZnO/p-GaN LEDs produced using the growth process to study the electro-optical properties. In short, the device was formed using the hexagonal ZnO disks that completely filled the openings in the insulating photoresist matrix. The process was more effective in eliminating pinholes and shorts between the RF sputter coated ITO top contact and GaN when compared to

our earlier designs. The processing is reduced to contacting the GaN substrate using two photolithographic steps. In the first step we used Shipley 1813 photoresist to form a 2mm by 2mm sized window to the GaN using a 30 second ITO and ZnO etch in 37% HCl. In the second step we form the bottom contact which is located 1 mm away from the ITO pad using electron-beam evaporated 60 nm Ni and then 300 nm Au, photolithography, GE-6 gold and NE-9 nickel etch and photoresist removal by rinsing with acetone, methanol, and isopropyl alcohol. This overgrowth method provides an advantage over earlier designs that required deposition of an insulating layer and polishing or etching to expose the top of the ZnO.[74, 75] The new process does not require these process steps since the ZnO crystals completely fill the openings in the insulating photoresist matrix. There are other cost advantages for solution processing of ZnO over alternative PECVD, MBE, or sputtering methods. A potential disadvantage is that some lithography is needed. However, masks can be reused, and fabrication is effective over large area substrates.

Figure 4-2B shows the electroluminescence of the resulting device under forward bias, revealing a six-pointed star of violet light under a 10x optical microscope objective which cannot be explained by the layout of the array which has a square lattice. Higher resolution analysis using a 50x objective (Fig. 4-2B inset) showed areas of high light intensity to match directions perpendicular to the hexagonal ZnO facets (Fig. 4-2C) which suggests that some light is transmitted and coupled preferentially along directions perpendicular to ZnO facets. We have not yet changed the dimension and spacing between the ZnO microcrystal LEDs to study coupling or lasing. Figure 4-2D shows PL and EL spectra as recorded using a scanning monochromator and photomultiplier tube attached to the upright microscope to collect light from selected areas with a minimal spot size of 50 μm. As PL excitation we used a handheld ultraviolet mercury vapor lamp and 254nm filter with a sub-350nm cutoff, UVP, model UVGL-58. Hydrothermally grown ZnO was delaminated from the GaN substrate for ZnO photoluminescence measurement, however EL measurements required an intact junction between n-ZnO and the p-GaN substrate. Comparison between the illustrated EL and PL spectra yields the following observation: the forward bias EL spectrum matches the PL spectrum of the ZnO crystals. The location of the PL peak near the approximately 390nm ZnO band edge suggests that photo-generated electrons and holes do not recombine at ZnO defects in the

visible. Photoluminescence of the bare GaN substrate (not shown) similarly showed at 390nm peak and lacked defects in the visible portion of the spectrum, allowing the conclusion that both the ZnO and GaN used here were high quality materials. Moreover, the electroluminescence spectrum (Fig. 4-2D) shows the absence of any peaks in the 450 to 650nm wavelength range, where deep-level ZnO crystal defects commonly radiate light.[75, 122] The absence of deep-level radiative defects in electroluminescence indicates that the p-GaN/n-ZnO interface generated using plasma-defined nucleation is a high quality photonic junction.

Previous work by others have shown that the defect peak wavelengths of ZnO varies widely depending on synthesis-related defect incorporation, on post-processing treatment including exposure to gases, or annealing under various temperature. Defects common to ZnO include zinc vacancies, inclusion of hydrogen, and surface defects including pinholes and grain boundaries. Our previously reported device[75] suffered from broad EL emission across the spectral range of these types of defects. The prior method used an unpatterned substrate and produced isolated nanowires that merged under continuous growth similar to those shown in Figure 4-1F (right) but with a slightly higher aspect ratio. Gaps/pinholes in between were filled with insulating SiO_2. The reduction of pinholes/grain boundaries, and the elimination of SiO_2 filler distinguishes this paper from the previous one and is therefore believed to be the primary reason for the improved performance. It has been previously found[84] that dislocation defects propagated from the original crystalline template are reduced in overgrown areas. The provided explanation was that since dislocations “cannot ’bend’ to be incorporated in the wings formed by lateral growth, the wing regions exhibit a much lower dislocation density relative to the regions of growth above the windows.” Whether or not this is the case in ZnO growth over the oxygen plasma treated area cannot be confirmed and would require similar high resolution cross-sectional TEM studies.

Illumination with a 6 watt handheld 365nm ultraviolet lamp caused the ZnO-GaN hexagonal heterojunctions to function as a photovoltaic cell (Fig. 4-3). The maximum open circuit voltage and short circuit junction current density was found to be 450 mV and 6 mA/cm^2, respectively. First order estimates yielded 1-9% electrical quantum efficiency. We do not have a precise number since the size of the active junction is

presently not known with sufficient accuracy. This calculation is based on the following measurements and assumptions. The incident optical power density of the UV lamp was determined to be 3.98mWatts/cm^2 as measured using an optical power meter, Anritsu, model ML9001. The optical power meter was connected to an optical power sensor, Anritsu, model MA9802A calibrated to detect a wavelength of 380nm. The ITO formed a simultaneous contact to about 100-300 ZnO/GaN junctions which was determined from the forward bias emission picture. As individual junction area we used 10 μm^2 to represent the photoresist opening which assumes that the oxygen passivated and overgrown area does not limit transport. The junction efficiency would be larger if this assumption is incorrect. The IV characteristic (Fig. 4-3C) of the 300 junctions yields, V_{mp} = 200mV and I_{mp} = 70nA for the voltage and current at the maximum power point and fill factor of 0.17 = $V_{mp}I_{mp}$ / $V_{oc}I_{sc}$. Considering these numbers and 300 active junctions we obtain 11% = 200mV*70nA / (300*10μm^2*3.98mWatts/cm^2) = electrical power per optical input power. We performed control experiments to test if the oxygen passivated and overgrown area limits transport by comparing the recorded currents with devices that are produced with and without (old process) plasma treatment. The experiment failed to provide a conclusive answer since the old process failed to produce a pinhole free film (Fig. 4-S2) or a device without shorts. While no direct measurement is available we do not think that the presence of an oxygen passivation significantly limits transport since the emission intensity appears uniform across individual crystals and since the calculated photovoltaic cells efficiencies would become larger than what can be anticipated for the given junction.

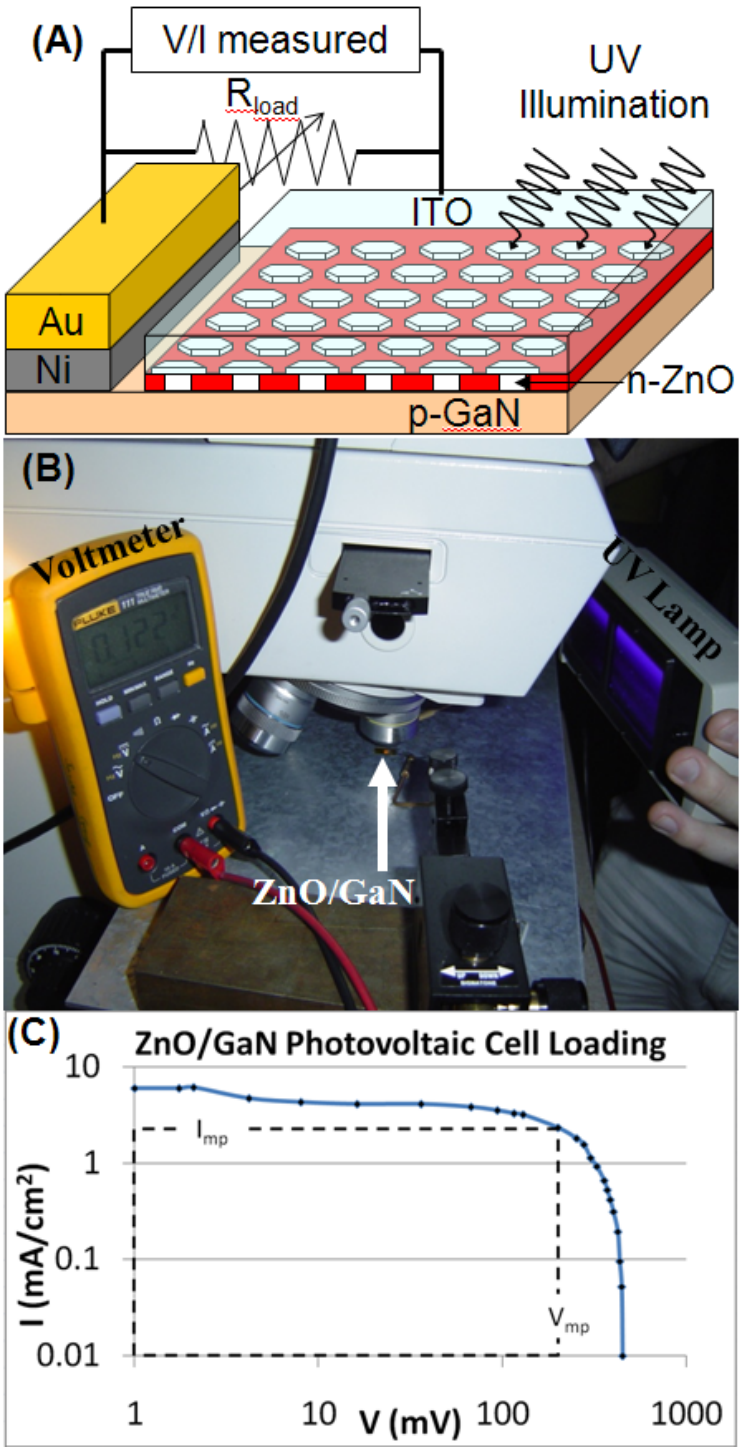

Figure 4-3. *ZnO microcrystal UV photovoltaic cell measurement - (A) schematic, (B) photograph of the experiment, and resulting (C) IV load curve under constant illumination. The loaded device contains approximately 300 junctions with 10 μm² individual area.*

4.3 Conclusion

In summary, the reported nucleation and growth process provides a new route towards the production of ZnO micro and nanostructures at known locations (0.7% STD) with well defined dimensions (<1% STD). The process produces high quality ZnO where deep-level radiative defects are eliminated. In addition to the demonstrated micro-LEDs and micro-photovoltaic cells we anticipate that these two features are attractive for a number of other applications that aim at integrating ZnO based devices such ultraviolet LEDs[73-75], laser cavities[121], waveguides[54, 110-112], high gain photodetectors[116], photovoltaic cells[113-115], sensors, piezoelectric actuators[120] or micro-power generators[119] at exact known locations on a surface. Control over location lead to the hexagonal light emission (Fig. 4-2B) and can ultimately be used to study coupling of light and lasing. It supports the ability to individually contact single ZnO crystals and learn how light propagates form one isolated domain to another. Moreover, it may be possible to transfer single crystal domains from one substrate to another though interfacial delamination which finds applications in the field of flexible transparent electronics.

Chapter V

Continuous Nanoparticle Generation and Assembly by Atmospheric Pressure Arc Discharge

Jesse J. Cole, En-Chiang Lin, Chad R. Barry, and Heiko O. Jacobs

Reproduced with permission from:

Applied Physics Letters 95, 113101 (2009)

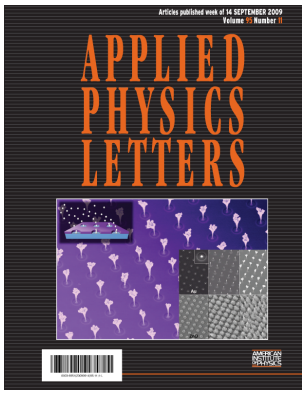

© 2011 American Institute of Physics

5.1 Introduction

The synthesis and the integration of inorganic nanomaterials continues to attract considerable growth as it provides a potential solution to the manufacture of low cost printable electronics, optoelectronics, and solar cells with higher performance than their organic counterpart. There are a number of different methods to the synthesis and integration: wet chemical synthetic routes combined with inkjet printing compete against gas phase synthesis and deposition methods. Solution based processes require the formulation of stable printable inks using organic ligands[123, 124] which are often orthogonal to what is desired from an electronic point of view. Gas phase methods eliminate this requirement providing a larger selection of materials including Si, Ge, GaN, and GaAs. Considering gas phase processes the use of plasmas remains the dominant method in the synthesis, etching, and deposition of thin films and nanomaterials.[125] Typically a distinction is made between low and atmospheric pressure plasmas. Low pressure plasmas provide high uniformity in coatings or etching applications but suffer from low mass flow, deposition, or etch rate. Atmospheric pressure plasmas on the other hand provide a high mass flow, deposition, or etching rates,[126] but typically suffer from lower uniformity. Such atmospheric pressure plasma systems consist of two distinctly different regions. The first region is the visible plasma region which contains high energy electrons and ions at temperatures up to 22000K with electron n_e and ion densities n_i ranging from $10^8 cm^{-3}$ to $10^{15} cm^{-3}$ used to evaporate, sputter, or dissociate precursor materials[127, 128]. High temperature plasmas in the form of DC arc discharges led to the discovery and industrial production of fullerenes and carbon nanotubes[96-99] through erosion of graphite electrodes and have since then emerged to form other technologically relevant nanomaterials including GaN[100], Pd[101], and Si[102] to name a few. The second “cold” region surrounding the visible plasma can be described as low energy room temperature gas with ions, electrons, and neutral or charged nanoparticles and is governed by aerosol science. The fact that these aerosols contain charged nanomaterials at low temperature makes these systems ideally suited for charge directed printing of electronically functional inorganic materials. In other words it is conceivable that plasma systems can be utilized to produce functional charged nanoparticles that feed into nanoxerographic[12, 18, 108, 129, 130] type

processes to print nanoparticles as opposed to μm sized toner particles. Existing nanoxerographic printers provide sub 100nm lateral resolution by depositing charged nanoparticles onto oppositely charged surface areas. Yet these xerographic methods were limited to initial charge concentrations in the dielectric layer that were insufficient to form patterned nanoparticle films with thicknesses exceeding a single or few monolayers.[12, 18, 108, 129, 130] Localized deposition of patterned films with any desired thickness has remained a challenge.

This letter describes a new deposition system which combines an atmospheric pressure plasma with an electrodynamic deposition process to form nanostructures from sub 20 nm metallic or semiconducting nanoparticles. More specifically, the apparatus uses a DC arc discharge between two consumable Au or Zn electrodes to continuously generate nanoparticles and a third sample electrode placed nearby for nanoparticle collection. The resist becomes highly charged resulting in the formation of localized electrodynamic nanolenses which focus nanoparticle deposition. The deposition process does not deplete the underlying charge pattern enabling the deposition of tall nanostructures (more than 100 monolayers). While the present paper is limited to two materials we anticipate that the process can be extended to any nanomaterial type that has been formed using high temperature plasma.

5.2 Results and Discussion

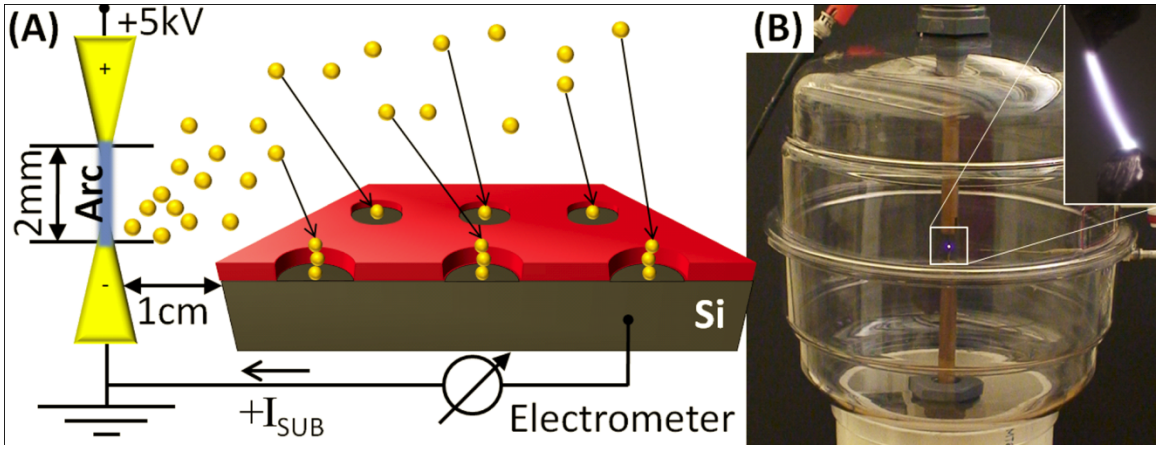

Figure 5-1. *Schematic and photograph of the basic elements. (A) An atmospheric pressure DC arc discharge is established between two consumable electrodes that are separated by 2 mm. (B and inset) The photograph shows the typical appearance of the arc between Au electrodes. Produced positively charged nanoparticles are collected on a grounded substrate outside the plasma region. Flux and deposition of charged particles is monitored using a Keithley (6517A) electrometer.*

Figure 5-1 illustrates the basic elements and dimensions of the apparatus (A). The apparatus was enclosed in (B) a modified polypropylene desiccator sealed to prevent nanoparticle inhalation. A 10kV, 100mA controlled current power supply (Gamma High Voltage Research Inc., RR5-120R/CPC/M994) was used to ignite and maintain a 10W DC arc discharge between two identical consumable electrodes. For consumable electrodes we used Au and Zn in wire form (2 to 5 mm diameter). The materials were clamped into slits in copper rods allowing adjustment of the separation. The anode (top electrodes in A,B) was given a high positive potential and the cathode (bottom in A,B) was grounded. Photographs of the arc (B inset) displayed the expected arc luminescence for atmospheric pressure air conditions (20.95% O_2 by mole). Spectroscopy of blue-white O_2 discharges shows peaks at 419nm[131] due to positive ionization of O_2 into O_2^+, where these ions present in the arc may play a role in nanoparticle charging and formation. The process of nanoparticle formation using atmospheric pressure arcs is

established and we refer to Smirnov[132] for an introduction. In brief high mobility electrons generated by the arc are accelerated by the applied electric field to the anode, producing gas ions as they travel. Incident positive gas ions are brought to the cathode where they impact the cathode tip surface. Erosion is observed only at the cathode because the heavy positive gas ions release more kinetic energy than the electrons when impacting the electrode surface. The eroded material is collected at the sample. During collection an electrometer can be used to measure a positive current, I_{SUB}~1nA, indicating that the deposited nanoparticles are positively charged. The erosion process increases with the arc current. To prevent rapid evaporation of the cathodes all experiments were performed at 10W with controlled arc currents <100mA which is quite similar to what is used in atmospheric pressure arc discharge lamps[128].

Figure 5-2 depicts scanning electron micrographs of gold nanoparticles deposited onto a silicon substrate electrode that was partially shielded using patterned PMMA. After patterning the samples were exposed to 49% HF for 30s before deposition to remove the native SiO_2 layer. Deposition into openings is achieved down to 200nm (A) where electrodynamic focusing allows resolution below 100nm with deposit geometries that depend on resist feature size and time. Initially nanoparticles are focused into clusters at the center of the resist opening (B) then after 15minutes of deposition(C) the deposits broaden. Throughout the lengthy deposition process it can be seen that particles are absent from the resist, suggesting that nanoparticles are repelled from deposition there.

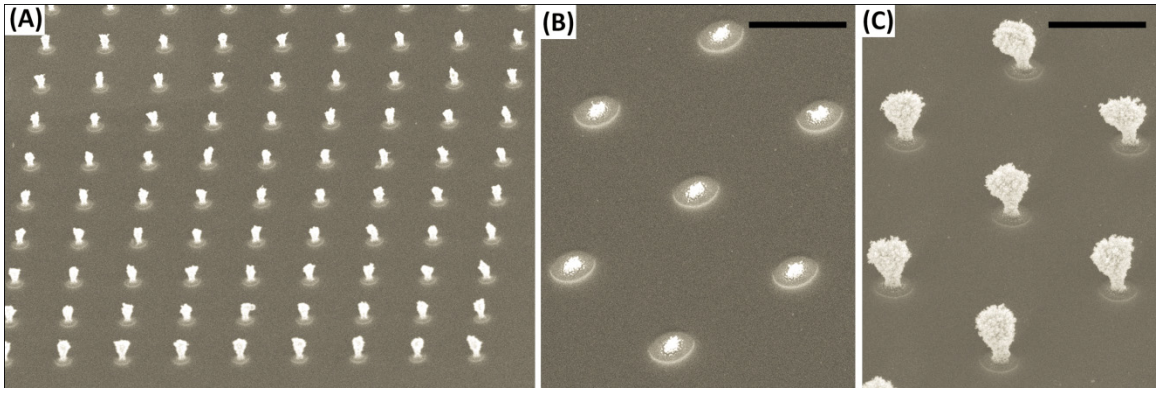

Figure 5-2. *Gold nanoparticle collection in submicron features in 80nm thin PMMA ebeam resist. Continuous charge-based nanoparticle deposition results in three-dimensional deposition into arrays with 200nm diameter openings(A) to 500nm*

openings(B,C). Au nanoparticles are initially focused(B) into the center of the openings then broaden(C) as nanoparticles continue to deposit over 15minutes. Scale bars:1μm in (B,C).

This is quite remarkable and holds for even micron-scale features as shown in Figure 3. Whether depositing metallic Au (A,B,C) over time or semiconducting ZnO (D,E,F) the insulating surfaces appear to self-equilibrate to a sufficiently high potential for the nanoparticle flux to be directed to the grounded regions. The focusing effect and small standard deviation in location of the deposits become apparent using Au nanoparticles and 1 μm circular openings (A inset). Here the Au particles initially deposit into an area that is approximately 7 times smaller in area than the opening but spread out over time yielding tower like structures that can be several micrometers tall (B). Continued deposition causes the tops of towers to broaden (C). These towers contain several hundred layers of 10-20 nm particles. Thin < 1μm deposits (A,B) are very uniform over large areas while thick >2 μm deposits (C) begin to show some level of variations over mm sized areas. For the case of ZnO we observe the more resistive nanomaterial to cause deposit broadening at smaller deposit heights, ultimately resulting in different deposit morphology and porosity (C,F insets).

The process is understood to work in the following way: material deposition does not occur on insulators without a conductive substrate, suggesting field directed assembly to be the dominant mechanism. The arc produces a gas medium of high mobility bipolar gas ions and orders of magnitude lower mobility / heavier charged nanoparticles. After introduction of uncharged resist, we expect adsorption of these charged species to be controlled by drift and diffusion favoring high mobility gas ions initially until a steady state is reached where the resist surface is charged. The system equilibrates and establishes whatever necessary fringing field to funnel material to conducting surfaces where they become neutralized. The process is fundamentally different from known xerographic methods where deposition occurs onto the insulating surface instead of the conductor. It is an electrodynamic instead of electrostatic process which means that films of any desired thickness can be formed without depleting the charge differentials that direct the deposition process.

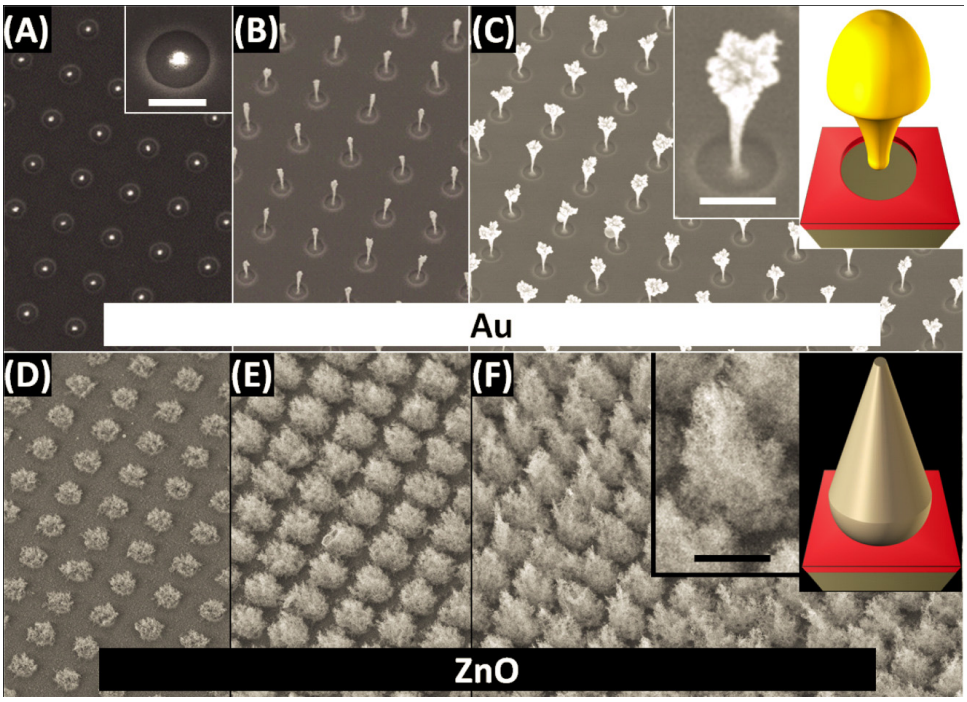

Figure 5-3. *Representative images of Au and ZnO nanoparticle deposits in S1805 photoresist as a function of deposition time increasing from 2 minutes (A,D) to 15 minutes (B,E) to 30 minutes (C,F) at constant 10W arc discharge power. Morphology differences(C,F insets) are attributed to differences in charge-based deposition behavior of the nanomaterials. Scale bars: 1µm in (A inset,C,F).*

5.3 Conclusion

In summary, the reported gas-phase nanomaterial production process was shown to produce nanoparticles of Au and ZnO. Collection of positively charged nanoparticles in predetermined areas is demonstrated over extended periods of time without depleting the Coulomb forces that direct the deposition process. The process works in the gas phase at atmospheric pressure and does not require vacuum equipment. The process eliminates the need to remove particles from the reactor walls to formulate stable suspensions / electronic inks otherwise required if serial inkjet type methods were to be used to print the materials. Methods of self-aligned integration of nanoparticles are important to a number of fields including printable electronics, sensors, or catalysis. The process improves deposition efficiency through the focusing effect; no lift-off is required and material is conserved which is attractive considering material cost. At present we have only varied a few process parameters. Questions of ultimate uniformity, extension to large area deposition using multiple spatially separated discharge regions will require further research.

Chapter VI

Mimicking Electrodeposition in the Gas Phase: a Programmable Concept for Selected Area Fabrication of Multimaterial Nanostructures

Jesse J. Cole, En-Chiang Lin, Chad R. Barry, and Heiko O. Jacobs

Reproduced with permission from:

Small 6(10), 1117-1124 (2010)

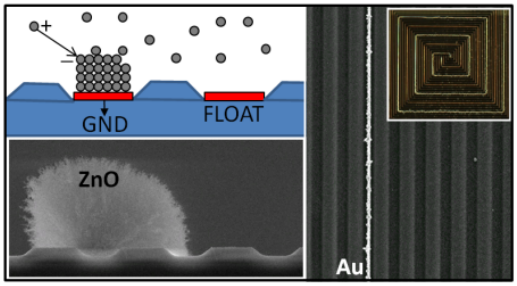

© 2011 Wiley-VCH Verlag GmbH & Co. KGaA, Weinheim

6.1 Introduction

Modern interest in nanotechnology as a platform for functional systems drives the need for techniques to localize deposition of metals, oxides, and semiconducting materials. From a synthesis point of view, these materials are commonly formed in the liquid or gas phase. One of the most powerful liquid phase techniques remains traditional electrodeposition which has several unique characteristics absent from emerging direct write[87-89] or transfer techniques[90]. The most important being the ability to locally program the deposition of material (ions[91], nanoparticles[92, 93], and nanowires[94]) by simply applying a bias to an electrode. This characteristic supports programmable selected area deposition for materials and is presently limited to the liquid phase. The closest known gas phase extension to electrodeposition are electrostatic precipitators[95] which employ electrically biased plates to attract charged particles for filter applications. A gas phase deposition system to deposit material into addressable areas forming vias, interconnects, patterned multimaterial or multilayer films in a programmable fashion has, however, not yet been reported. Such a deposition process would be important in the context of printable electronics since many functional nanomaterials are presently formed in the gas phase. The present report describes a system working at atmospheric pressure to form electrically interconnected nanostructured thin films with 60nm lateral resolution and predetermined thickness. The system uses a DC plasma arc discharge between two consumable electrodes as a material source. The use of a DC arc discharge between consumable electrodes is a known concept to produce charged nanomaterials in large quantities; DC arc discharge between graphite electrodes led to the discovery and industrial production of fullerenes and carbon nanotubes[96-99] and the concept has also been extended to produce GaN[100], Pd[101], and Si[102] clusters and particles to name a few. In these earlier systems, particles coated the reactor walls uniformly.

Here we describe an insitu method which couples the particle source with a localized deposition system to mimicking electrodeposition in a gaseous environment. The approach uses a patterned substrate to funnel the material to specific locations with 60nm standard deviation in positional accuracy and uses an array of electrically biased domains to sequentially program the deposition of more than one material type. This is different from prior work in the field of gas phase nanoxerography where nanoparticles were

deposited onto charged substrate locations using a fixed amount of initial charge inside a dielectric[133] or a PN junction[134]. These prior methods do not allow programming. Moreover the fixed amount of initial charges limits the quantity of charged material that can be attracted before the trapped charges are depleted and screened. In the present case the biased electrodes provide a path for charge neutralization and maintain a constant potential difference that directs the assembly until the external voltage is turned off. This provides control over the amount of material and the type of material that can be deposited onto a desired area. As an application programmable selected area deposition of dissimilar materials is used to fabricate physical sensor arrays containing light and humidity sensitive areas on the same chip. The physics of how the particles are charged in the particular arc discharge system prior to deposition on a substrate at room temperature is discussed and involves diffusional charging through a positive space charge region surrounding the electrode that is consumed by the process forming charged nanoclusters which finally deposit on a low temperature substrate.

6.2 Results and Discussion

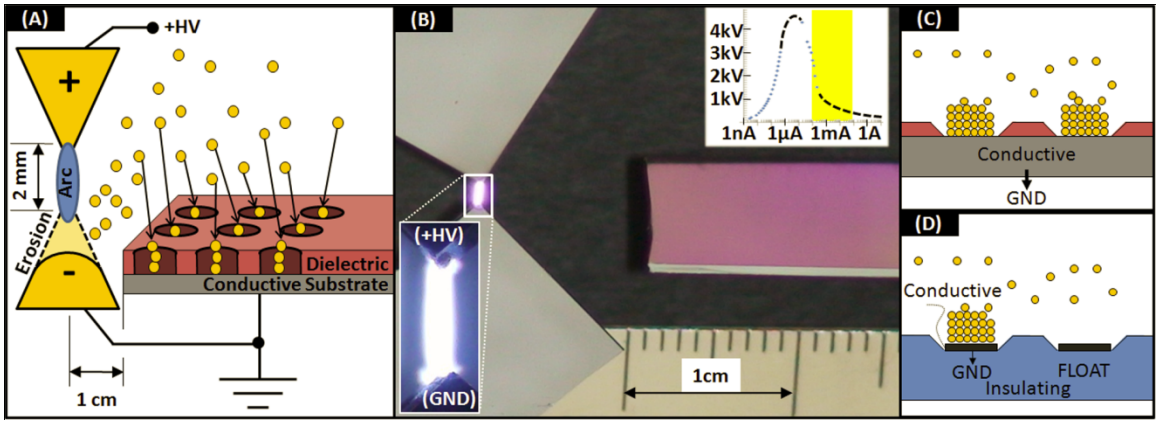

Figure 6-1. *Schematic and photograph of the basic elements of the prototype gas phase nanocluster electrodeposition system. (A) An atmospheric pressure DC arc discharge is established between two consumable electrodes that are separated by 2 mm. (B and zoom) The photograph shows the typical appearance of the arc between silicon electrodes where the cathode at the bottom initially sharp is rounded and consumed over time. (B inset) The arc is operated within the negative differential resistance regime highlighted in the recorded I/V characteristic which is accomplished using a current*

controlled high voltage source as opposed to the positive differential resistance corona discharge region to the left. Produced nanoparticles are collected on a grounded substrate outside the plasma region. (C) The grounded conductive substrate can be partially shielded using a patterned dielectric to accomplish focused assembly into the openings or (D) segmented into separated programmable regions.

Figure 6-1 illustrates the basic elements and dimensions of the apparatus. It uses a 0.1-100 mA DC plasma arc discharge between two consumable electrodes (left side of A, B) to continuously generate nanoparticles and a third sample electrode placed in the region outside of the visible plasma volume (aerosol region) to collect 20 nm Au, 15 nm Si, 15 nm TiO_2, 15 nm ZnO, or 10 nm Ge nanoparticles (right side of A, B). Nanoparticle collection is discussed later in Figure 6-3 (schematic C) and Figure 6-5 (schematic D). Additional details for the apparatus used here are included in the Experimental section. The anode (B, top electrode) was given a high positive potential and the cathode (B, bottom) was electrically grounded. The upper right inset in Figure 1B shows a typical current voltage (I/V) arc characteristic for Si electrodes with 2 mm gap distance. We operated the system in the arc regime to the right that is characterized by the negative differential resistance as opposed to corona regime to the left. Photographs of the arc (B inset) were taken at 10x reduced arc power (1mA, 1kV, and 1W) in order to resolve the electrode showing the expected blue-white arc luminescence for atmospheric pressure air conditions (21% O_2 and 78% N_2 by mole) and red-purple arc luminescence (not shown) after argon purge (>99.9% Ar). Arc luminescence indicates positive ionization of gas species.[135] The process of nanoparticle formation using atmospheric pressure arcs is well established and we refer to Smirnov[132] for an introduction. In brief high mobility electrons generated by the arc are accelerated by the applied electric field to the anode, producing gas ions as they travel. Incident positive gas ions are brought to the cathode where they impact the cathode tip surface. Erosion is observed only at the cathode because the heavy positive gas ions will release more kinetic energy than the electrons when impacting the electrode surface. The erosion process increases with the arc current.[136]

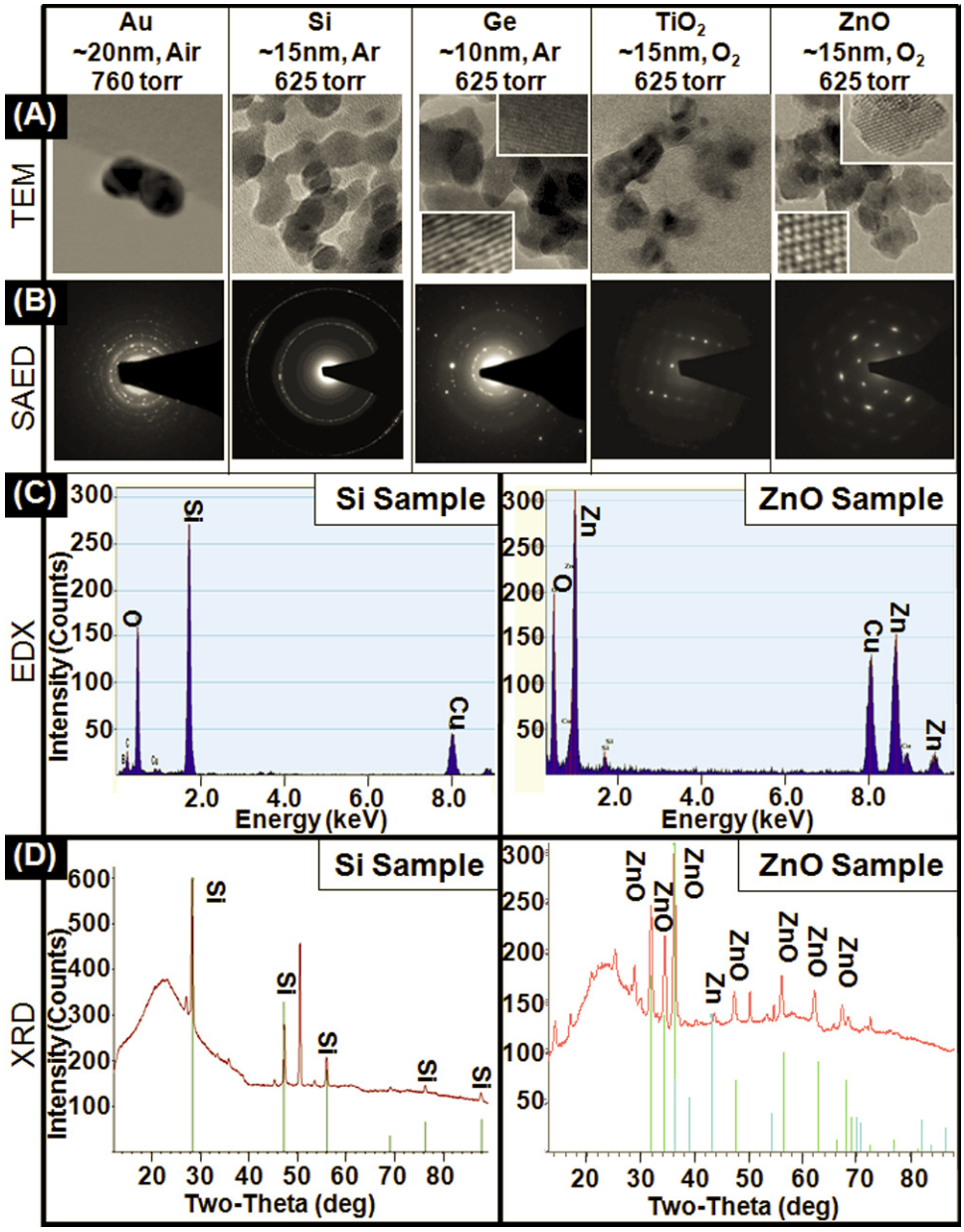

Figure 6-2. *Characterization of nanomaterials produced by atmospheric pressure arc discharge. (A) TEM results show that sub-20nm nanoparticles of Au, Si, Ge, TiO_2 and ZnO were generated, with HRTEM images (A insets) showing fringes for Ge and ZnO particles. (B) SAED confirms high particle crystallinity in all cases. (C) EDX results for Si and ZnO suggest the nanoparticle material type was related to the arc electrode material with a noticeable oxygen presence in its surface sensitive signal. (D) XRD data confirms strong unoxidized Si peaks suggesting minimal oxidation of Si nanoparticle interiors which contrasts the nearly complete oxidation of Zn into ZnO.*

Figure 6-2 provides material specific data to represent a few of the nanomaterials that are formed as a result of cathode erosion at an input power that was limited to 10W to prevent rapid evaporation of the cathodes. The results confirm that DC arc discharge can quickly be adapted to produce a variety of materials which are considered important in the field of printable electronics. The average particle sizes were found to be 20 nm for Au, 15 nm for Si, 10nm for Ge, 15nm for TiO_2, and 15nm for ZnO. EDX (Energy Dispersive X-ray Spectroscopy) for Si and ZnO nanoparticles shows the presence of oxygen in addition to the electrode material. The XRD (X-ray Diffraction) which is sensitive to material deeper than the surface shows strong Si peaks and absence of any significant SiO_2 suggesting that the Si particles have crystalline Si cores with SiO_2 surfaces. This contrasts the case when Zn electrodes where used; here XRD suggests nearly complete oxidation forming ZnO in the semiconducting zincite form. The supplementary information provides further discussions and includes results for Au, Ge, and TiO_2 omitted here for brevity.

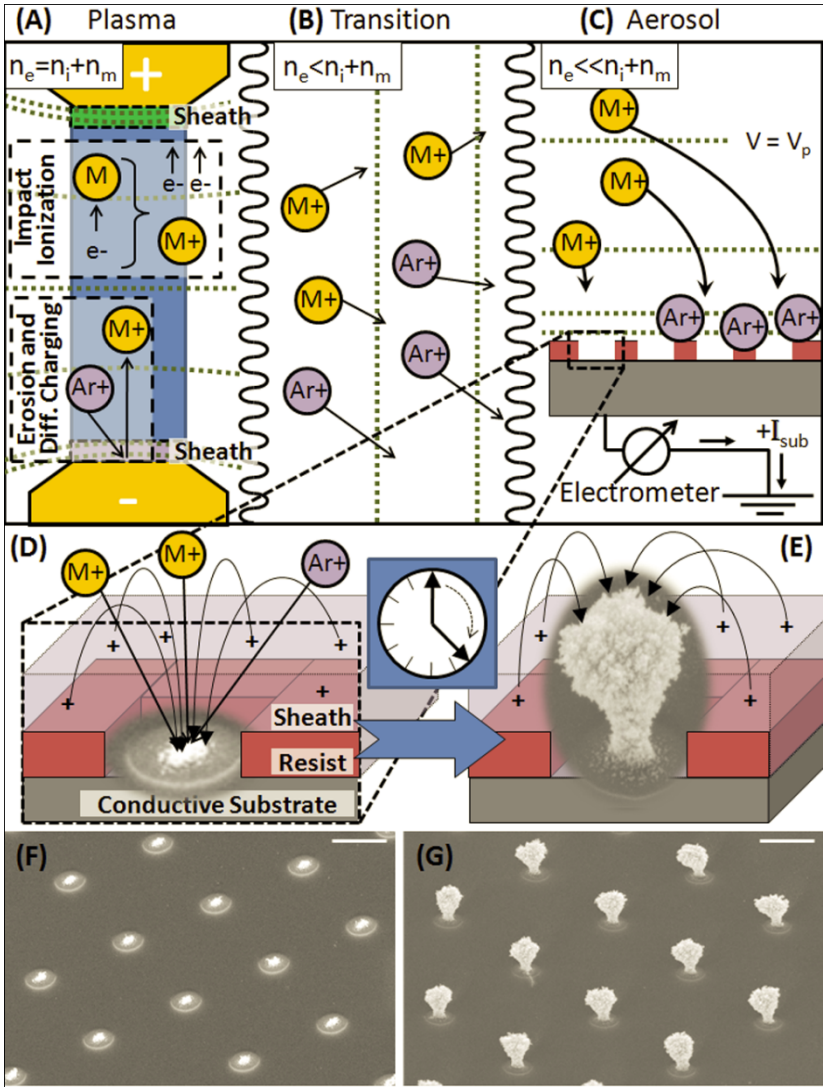

Figure 6-3. *Process details and hypothesis. (A) Nanomaterials in the arc become charged as they leave the positively charged cathode sheath (pink layer) and diffuse away through a (B) transitional region entering a cold (C) aerosol region where they are collected. (C) The collection of M+ and Ar+ ions is monitored using an electrometer that connects the sample to ground recording the steady state neutralization current. (D and E) The nanolens effect visible in the overlaid SEM results is explained using high mobility Ar+ gas ions which cause the patterned dielectric layer (purple) to float up to become positively charged (pink transparent sheath layer). The lower mobility nanoparticles (Au shown) deposit into the openings as a result of the established fringing field. Continuous nanoparticle deposition develops the pattern into tower like structures. 1 μm scale bars in (F,G).*

Figure 6-3 depicts the working hypothesis of the deposition process and provides details as to why the particles become positively charged supporting collection on grounded or negatively biased conducting surfaces. The illustration describes the case for metal electrodes (M) exposed to an argon DC arc discharge but can be extended to all the other materials and carrier gases that we investigated so far. The illustration is divided into three areas: (A) a hot plasma region with free electrons *e*-, *Ar*+ ions, and positive particles *M*+ of concentrations n_e, n_i, and n_m which is quasineutral ($n_e=n_i+n_m$), (B) a warm transitional region, and (C) a cold aerosol region where the positive particle/ion concentration n_i+n_m exceeds the free electron concentration n_e forming a positively charge aerosol ($n_e << n_i+n_m$). The cold aerosol region depicts a flux of positive charged particle *M*+ and ions *Ar*+ which is recorded using the electrometer. Visual inspection of the consumable electrodes show that the nanoparticles originate at the cathode which is eroded and consumed over time while the anode remains largely unaffected by the process. The nanoparticles diffuse through the transition region and deposit onto grounded surfaces causing discoloration visible to the bare eye within a minute. However, the nanoparticles will not coat insulating surfaces. This selectivity between conducting and insulating surfaces is illustrated in the schematic and Scanning Electron Microscope (SEM) micrographs (Figure 6-3D,E,F) where the materials deposit into 300 nm openings in a 100 nm thick insulating film of PMMA resist on top of a grounded Si chip forming tower-like structures (Figures 6-3E,G) as the deposition continues. During deposition a positive net ion current is recorded using the electrometer (Keithley, model 6517A) in the range of 0.1 nA – 20 nA where, 5 nA is a typical value. This current is related to the *M*+ deposition rate. For example if we operate the system in the corona discharge regime this current drops by 2 orders of magnitudes reflected in a reduced deposition rate. The durations to develop the pattern were 2 minutes for (F) and 15 minutes for (G) both using 5 nA deposition current, yielding an average deposition rate of ~70nm/min.

We observe positive charging of nanoparticles, which is somewhat counterintuitive from a plasma physics standpoint.[137] In a plasma surfaces typically acquire a negative surface charge since the electron thermal velocity $\sqrt{[3T_e/m]}$ exceeds the positive gas ion thermal velocity $\sqrt{[3T_i/M]}$ in thermal equilibrium $T_e = T_i$ by roughly three orders of

magnitude due to the smaller electron mass *m*. However, this negative surface charge is compensated by a sheath of positive space charge as illustrated in Figure 3A, pink region.[138][139, 140] Particles that originate at the cathode transit through this region and acquire a net positive charge (Figure 6-3A, bottom inset) through diffusion charging.[141] Electron impact ionization[142] is a second major charging mechanism which may play a role as well (Figure 6-3A, top inset). The charged particles will leave the arc vicinity crossing isopotential lines (dotted gray lines) driven by thermophoresis diffusion and convection to ultimately encounter the sample (Figure 6-3C) where they deposit on grounded or negatively biased surfaces.

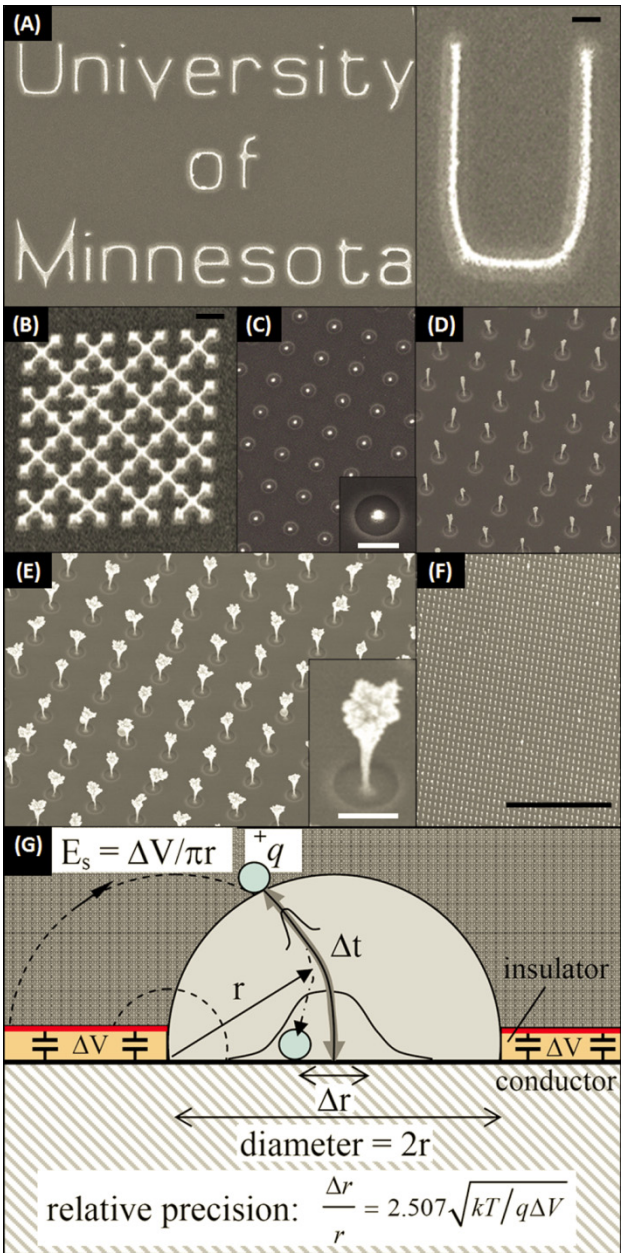

Figure 6-4. *Representative images of nanoparticle deposits limited to Au as a function of deposition time increasing from 2 minutes (A,B,C) to 15 minutes (D) to 30 minutes (E,F) at constant 10W arc discharge power. Particles deposit into openings in 80nm thin PMMA e-beam resist (A,B) or 0.5µm thick Shipley 1805 photoresist (D,E,F) with a minimal lateral resolution of 60 nm. Particles do not deposit on the resist and are initially direct to the centers of resist openings (G). Scale bars: 100nm for (A inset), 1 µm for (B), 1 µm for (C, E insets), and 100 µm for (F).*

Figure 6-4 depicts this selectivity between conducting and insulating surface showing gas-phase plating of <20 nm gold particles forming text, interconnected lines, grids, and arrays of vertical deposits on a silicon substrate that was partially shielded using a 80 nm thick e-beam patterned PMMA layers (A,B) and 500 nm thick S1805 photoresist (C,D,E,F) (details in Experimental section). The text structure (A) and interconnected grid (B) were developed in 120 seconds which illustrates that the gold particles can be deposited with 60nm lateral resolution without finding any particles on the resist itself. This is quite remarkable again showing that the insulting surfaces appear to self-equilibrate to a sufficiently high potential for the nanoparticle flux to be directed only to grounded regions. A focusing effect and a small standard deviation in the location of the deposits become apparent using 1 μm circular openings (C,D,E). Here the particles initially deposit into an area that is approximately 7 times smaller than the opening but spread out over time yielding tower like structures that can be several micrometers tall (D). This focusing effect is a function of the deposition rate and needs to be further investigated. Higher deposition rates appear to defocus the patterns. Continued deposition causes the tops of towers to broaden (E). These towers contain several hundred layers of 5-20 nm particles. Small 1 μm deposits (A,B) are uniform over large areas while tall 2μm deposits (F) begin to show some level of variations over mm sized areas.

Initial focusing of deposited nanoparticles (Figure 6-4G) has been observed previously when a surface was exposed to ions and a low concentration of nanoparticles.[143] The relative precision of focused nanoparticle deposition was found to depend on the insulator surface potential.[143] Initial deposition behavior is sufficiently similar to prior work to prompt a brief discussion of the deposition physics. Here the observed focusing effect and expected precision can be studied by solving Langevin's equations of motion of nanoparticles inside an electric field. To establish an analytical form for the relative precision, we considered a single particle at a radial distance r from the center of a patterned hole, as illustrated in Figure 6-4G. In this case, the uncertainty acquired in the particle trajectory (Δr) due to Brownian motion can be described by the root-mean-square displacement or half-width of the Gaussian bell curve $\Delta r = \sqrt{(2\Delta t D)}$, where Δt is the time for a particle to deposit, $D = CkT/(3\pi d\eta)$ is the Stokes-Einstein diffusion coefficient for nanoparticles of diameter d, viscosity η, and empirical slip correction factor C. Maximum

deviation considering a Newtonian trajectory will occur at the center, where the field strength is smaller and where the time to deposit will be increased. The electric field along the central particle path, $E_s = \Delta V/(\pi r)$, will cause the particle to follow the trajectory with a terminal velocity $v_t = CqE_s/(3\pi d\eta) = qE_sD/(kT)$. Substituting $\Delta t = r/v_t$ yields a normalized half-width of the Gaussian bell curve in the form of Equation (1):

$$\frac{\Delta r}{r} = \sqrt{\frac{2kT}{qrE_s}} = 2.507\sqrt{\frac{kT}{q\Delta V}} \tag{1}$$

Equation (1) provides a number of important insights into electric-field-directed self-assembly processes. First, the key measure of the expected focusing will be the potential difference between charged and uncharged areas. Values of $q\Delta V$ larger than kT are desired. Second, the relative precision is independent of the size of the pattern and therefore scaleable. Third, the precision can be increased by increasing the particle charge.

Following initial focused depositon the process is allowed to continue until deposited conductive nanoparticles eventually alter the electric field lines. The towers grow with electric field lines pointing towards the tops of the nanoparticle towers which exceed the height of the confining charged resist. Due to this increased distance between depositing nanoparticle and charged resist, nanoparticle mass transport becomes more poorly focused to the center of the resist openings resulting in mushroom-shaped nanomaterial towers.

Figure 6-5 shows a process and results of programmable deposition of three different materials Au, ZnO, and Ge using sequentially biased electrodes, and the concept of programmable deposition is applied to produce a multimaterial sensor array with humidity and photosensitive regions. The illustrations (A, B and C) depict the concept. First gold nanoparticles are plated on a grounded organic conductor P3HT (poly 3-hexylthiophene) while nearby P3HT lines and glass surfaces (preparation details in Experimental section) electrically float up to a sufficiently high electrical potential preventing gold nanoparticle deposition in the surrounding area. Resistance measured for the initial P3HT line exceeded 10MΩ. Covering the P3HT line with Au nanoparticles reduced the resistance to 2.9kΩ. The Au line was 3 mm long, ~500 nm wide, and plated

be 1 μm thick. Applying Ohms Law yields a measured resistivity of $4.8*10^{-5}$ Ω-cm which is close to $2.26*10^{-6}$ Ω-cm (accepted value for Au at 298K). After the Au line deposition the arc electrodes were replaced to deposit ZnO onto a separate originally floating P3HT line which is now grounded while everything else is left floating (Figure 6-5B). ZnO nanoparticles now deposit selectively onto the grounded electrodes as before in the case of Au. The ZnO example illustrates what happens after 30 minutes of deposition. The films begin to overgrow the grounded region forming roughly a hemi-cylindrical structure.

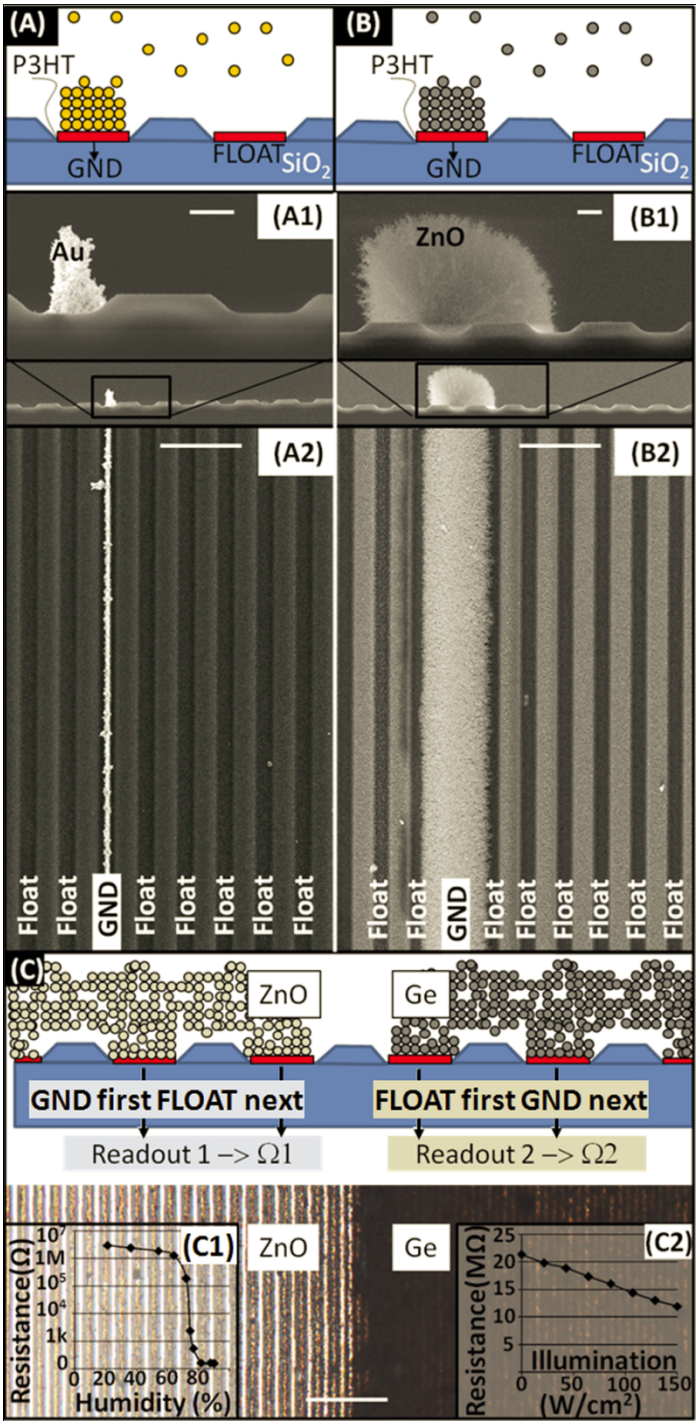

Figure 6-5. *Concept and results of programmable multi-material (Au, ZnO, Ge) deposition forming (A) conducting and (B) semiconducting traces, or (C1) humidity and (C2) light sensitive areas. (A,B) Grounded 1 µm wide P3HT lines attract nanoparticles forming a continuous interconnected structure as illustrated in the cross-sectional (A1,B1) and top-down (A2, B2) SEM images. Au particles pack into denser structures*

than ZnO and yield smaller line widths for identical deposition time (30min) and arc power (10W). (C) Programmable deposition procedure using sequentially grounded electrodes applied to form sensing layers where the same electrodes are subsequently used for readout. During the first deposition cycle all the electrodes on the left side are connected to ground until ZnO forms a merged film on the left side. This is reversed in the second cycle to the right until Ge covers the right side of the chip which is visible in the darker appearance of Ge under an optical microscope. The two film regions bridge the electrodes underneath and yield a characteristic resistance which reduces with humidity for ZnO (C1) and illumination for Ge (C2). 1μm scale bars in (A1,B1), 10μm scale bars in (A2,B2), and 20 μm scale bar in (C).

This concept of programmable deposition and overgrowth bridging nearby electrodes can be used to program the deposition of multimaterial sensor arrays while providing a parallel readout on a single chip. The concept is illustrated for ZnO and Ge in Figure 6-5C which results in a continuous interconnected film of ZnO on the left and Ge on the right. The films bridge adjacent conductive lines (preparation details in Experimental section) whereby the bridge resistance varies with exposure to light (Ge) and humidity (ZnO). The magnitude of the resistance change in Ge due to illumination is attributed to long minority carrier lifetimes in the crystalline Ge. The large increase in the conductivity for ZnO is likely directly related to the high porosity and large surface area which is apparent in the cross-sectional SEM image (B1) discussed before.

To understand why a uniform deposition is observed and what the potential limitations might be the thickness of the space charge sheaths surrounding the sample surface has to be considered. These sheaths were depicted in Fig. 6-3D and are analogous to the double layers surrounding the surfaces in the liquid phase and thicknesses are on the order of the Debye length.[142] Adjacent areas on the sample within the distances of the characteristic Debye length will compete to attract nanoparticles which arrive at this boundary layer primarily driven by diffusion.[144] As in the liquid phase the Debye radius r_D is inversely proportional to the square root of the average number concentration n_0 of charged particles above the sample surface and is given for the gas phase by Equation (2).

$$r_D = \sqrt{\frac{1}{n_o}}\sqrt{\frac{k\varepsilon_0}{e^2(1/T_e + 1/T_i)}} \quad (2)$$

For Equation (2), k is the Boltzmann constant, ε_0 is the free space permittivity, and e is the elementary charge. T_e and T_i are the electron and ion temperatures which are assumed to be at room temperature in the aerosol regime. The number concentration n_0 of charged particles that can be supported was estimated using conductivity measurements as described in the supplementary information controlling the distance to the arc and the arc current. Typical values ranged between 10^9cm^{-3} to 10^7cm^{-3} corresponding to a Debye length in the range of 50-500μm, respectively. These n_0 values are close to previously published values of (10^9cm^{-3}) recorded near charging sources in atmospheric pressure aerosol.[145] The numbers are in contrast to the situation in standard vacuum deposition systems where the Debye length easily exceeds the dimensions of the deposition system by orders of magnitudes since the number concentration of gas molecules drops proportionally with pressure. At the same time the Debye length remains orders of magnitudes larger than the sub micrometer values found in liquid phase. Despite this important difference it has become small enough to enable in-situ selected area deposition. While adjacent areas on the sample compete for nanoparticles within the Debye radius the formation of arbitrary patterns (Figure 6-4) can still be achieved. The implication of a sufficiently small Debye length attained at high pressure is that the electrostatic deposition behavior becomes decoupled from the source. Less stringent requirements for symmetric designs with respect to the particle source are a direct result.

Figure 6-6 investigates the presence of stray particles testing the deposition on isolated lines and interdigitated electrode structures. The dimensions of the patterns are scaled to provide a larger field of view showing 15 μm (A) and 80 μm (B) pitched patterns. Nanoparticle deposition selectivity is high: even after extended deposition times these test structures did not produce an observable amount of stray particles onto the insulating surfaces or floating metal lines. The correctly deposited Au was 3μm tall which represents at least 100 particle layers. We expect the selectivity of sequential deposition steps with multiple material types to be nearly as high as the selectivity of a single step since crosstalk between lines appears to be minimal.

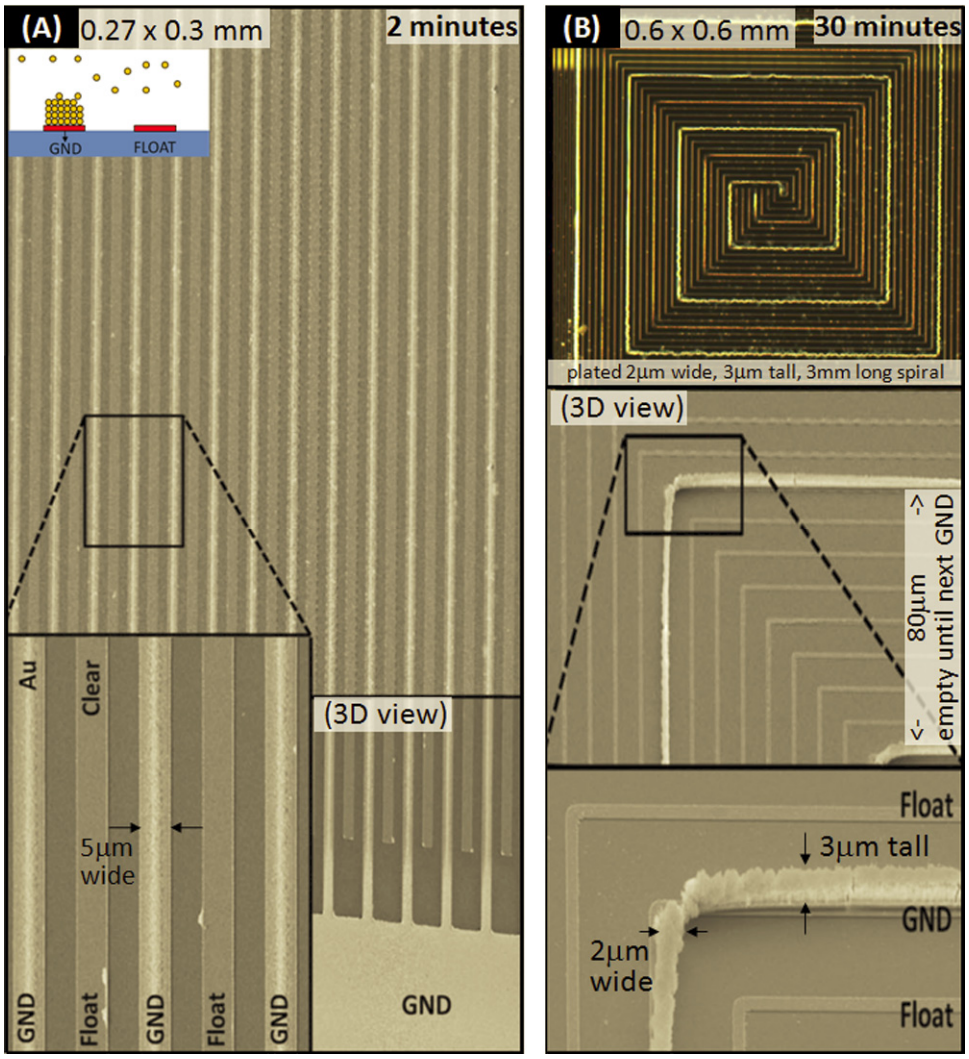

Figure 6-6. *Schematic and results of programmable selected area gas-phase electrodeposition after 2 min (A) and 30 min (B) deposition. The pad region in (A, bottom inset) shows the level of uniformity transitioning from a large (150x150 µm^2) single domain to spatially separated 5µm wide lines. Deposition occurs only on grounded areas; floating conductors and insulating surfaces remain empty. Increasing the size of the empty regions from 15 µm (A) to 80 µm (B) maintains this selectivity. The optical microscope image (B) depicts a spiral interspaced with 7 empty ones that were left floating yielding a single 2 µm wide, 3 µm tall, and 3 mm long Au line.*

6.3 Conclusions

Comparable to liquid phase electrodeposition, the reported gas phase analogue can deposit material into addressable areas forming vias, interconnects, or patterned multimaterial films in a programmable fashion. The process was tested using a limited set of technologically relevant functional materials including Au, Si, Ge, TiO_2, and ZnO at sizes of 20nm and below as confirmed by TEM, SAED, EDX, and XRD. We anticipate that the process can be extended to other materials and gas phase systems with some alterations. The uniformity on a macroscale is presently limited by diffusion since we use a single point source fixed in space. Scaling to larger sample areas would require the use of either multiple sources or translational motion analogous to what has been used in other gas phase deposition systems. The ability to maintain uniformity when developing arbitrary patterns on a nanoscale requires a sufficiently small Debye length which in turn favors higher pressure aerosols to provide a high concentration of charged particles/ions and deposition rate. The estimated values are sufficient to support selected area programmable deposition of a variety of different patterns including text, connected and disconnected structures. Operating a system at atmospheric pressure has the advantage of simplicity since neither vacuum pumps nor high pressure enclosures are required. Pressurized systems, however, would likely further increase the area selective deposition rate beyond the current 100 nm/min value. The current area selective rate is in between the 10 nm/min rate of non-selective vacuum deposition systems and typical 1 μm/min rate of area-selective electroplating methods. Variations in the film thickness, extension to large area deposition using multiple spatially separated discharge regions, passivation of surface and interface states are important aspects that will require further research and new and improved designs.

A potential future application of the gas phase electrodeposition technique can be found in the field of printable electronics. It contrasts the use of solution processable electronic inks and inkjet type printing concepts to deposit nanomaterials. Current inkjet based deposition systems have low resolution and throughput. The inks require surface functionalization to stabilize the particles which often interferes with the desired electronic properties. Alternatively the discussed *in-situ* gas phase synthesis and deposition system offers a more parallel route to the formation, deposition and integration

of higher performance materials than liquid phase concepts. High temperature processes can be used to produce the materials that can then be deposited onto low temperature substrates eliminating any extra processing steps or a transition into the liquid phase. As such the present technique is highly parallel and does not require the use and alignment of scanning nozzles or the formulation of stable liquid particle suspensions. These advantages come at the cost of needing pre-patterned substrates to direct the deposition.

6.4 Experimental Section

Nanoparticle deposition system: The apparatus was enclosed in a sealed polypropylene desiccator to prevent nanoparticle inhalation and to provide an inert experimental environment (Ar, He, and N_2 gases). We used a 10kV 100mA controlled current power supply (Gamma High Voltage Research Inc., 1kW model RR5-120R/CPC/M994) to ignite and maintain a 1-100W DC arc discharge between two identical consumable electrodes. For consumable electrode materials we used Au, Ti, Zn in wire form (2 to 5 mm in diameter) and Si and Ge wafer segments 4 cm long and 1 cm wide. The materials were attached using a slit type clamp cut into 15 mm diameter copper rods that allowed us to adjust the separation.

Substrates for selected area deposition: Patterned PMMA layer (A,B) and 500 nm thick S1805 photoresist sections were used to define the resist openings. A brief 30s 49% HF wet etch was used to remove the native silicon oxide layer. Samples were thoroughly rinsed with deionized water and blown dry by ultrahigh purity nitrogen (99.998%) and allowed to rehydrate for up to 15 minutes in ambient humidity environments typically ranging from 10% to 20% as measured by a humidity probe (Fisher Scientific, model S11120). Results in Figs. 6-3 and 6-4.

Substrates for programmable selected area deposition: PECVD was used to coat a Si substrate with 500nm SiO_2. The SiO_2 layer was patterned by photolithography and plasma etched by a mix of CF_4, CHF_3, and Ar at 150W power. The plasma etch was used to generate the trench features, such that even at the bottom of the trenches SiO_2 remained. The photoresist was finally stripped. Following SiO_2 patterning, the substrate was covered with a thick layer of P3HT, which was carefully etched back by O_2 plasma RIE until only P3HT in the trenches remained. Results in Figs. 6-5A,B.

Substrates for multimaterial sensor formation: 20nm Cr/200nm Cu was evaporated onto a photolithographically patterned pyrex wafer. Undesired Cr/Cu was removed by liftoff with acetone acting as the resist stripper and sonication to aid the process. The remaining metal was rinsed with methanol and IPA. Then the substrate was exposed to an oxygen plasma descum to remove any resist residue. Finally, the substrate was rinsed with deionized water and N_2 blown dry to remove any dust particles before nanoparticle collection. Results in Fig. 6-5C.

6.5 Supplementary Information

EDX (Energy Dispersive X-ray Spectroscopy) of the nanoparticles produced using the Ge, Ti show the presence of oxygen in addition to the electrode material (**Figure 6-S1**). The XRD (X-ray Diffraction) data which is sensitive to material deeper than the surface shows strong Ge peaks and absence of any significant GeO_2, suggesting that the Ge particles have crystalline Ge cores with GeO_2 surfaces. This contrasts the case when Ti electrodes where used; here XRD suggests nearly complete oxidation forming TiO_2 in the semiconducting rutile crystal form. XRD for Au was omitted since EDX showed no oxygen peak.

This section provides details on a second control experiment to determine the polarity of the particles and other supporting measurements which were omitted from the main part in the interest of brevity. The additional measurements include the measurement of the floating point potential and effective charge density n_0 above the sample used to calculate the Debye length. The experimental procedure employs a Langmuir probe shown in **Figure 6-S2**. A Langmuir probe is classically used in the field of plasma physics to characterize the plasma through measurement of charged particle fluxes to the walls as a function of probe voltage but can also be used within the aerosol to determine both the polarity and concentration of free charges. We fashioned our probe from a steel wire and inserted the wire through a tapered glass tube such that approx. 1.5mm of wire extended through the opening. The other end was connected in series to a 10MΩ resistor, followed by a DC power supply, and finally to ground. A digital multimeter was used to measure the voltage drop over the resistor yielding the current through the probe as a function of applied DC voltage.

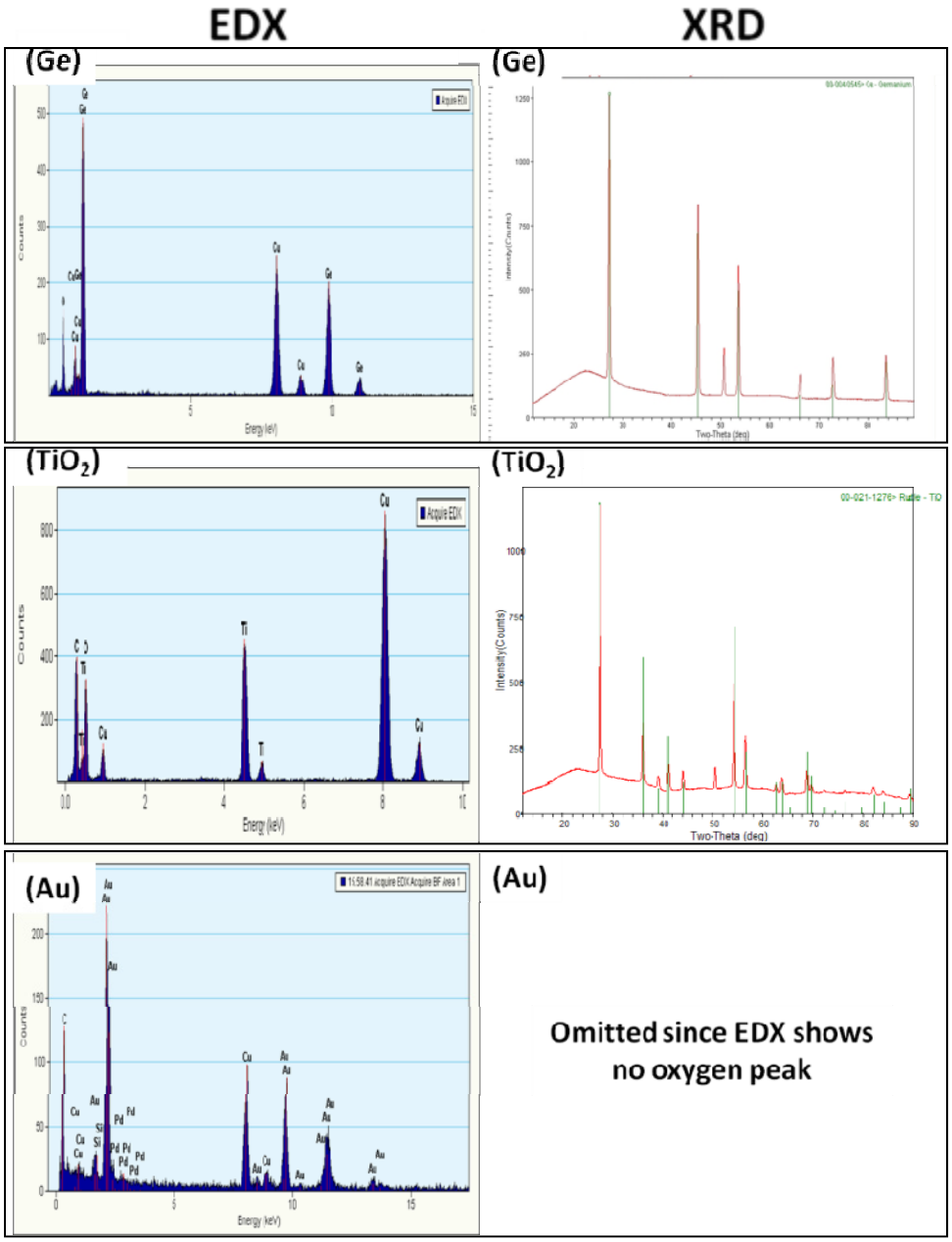

Figure 6-S1. *EDX, XRD data for Ge, TiO_2, and Au.*

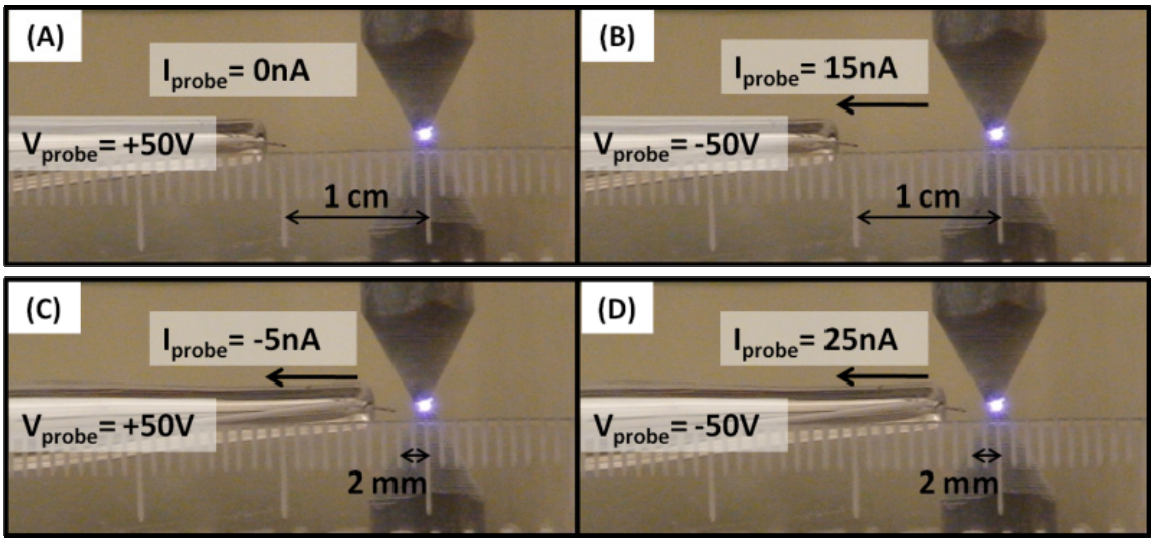

Figure 6-S2. *Langmuir probe measurement used to determine the polarity of both the ion current and floating point potential.*

We first determined the floating point potential V_p of the aerosol at the location where the sample would be located in an actual deposition experiment. The floating point potential is the required external potential which needs to be applied to the probe to null the recorded probe/ion current. Recorded values were always positive and were 50V and 3V, 10 mm and 2 mm away, respectively. A positive value means that the electrostatic potential of the particles is above ground level within this region. A grounded sample that is introduced to this location will be surrounded by a sheath of space charge. Such a sheath was illustrated in the schematic of figure 2 in the main body describing the deposition process.

A second part of this measurement was to record whether both negative and positive particles contributed to the current at this region or not. At distances exceeding 4 mm and a favorable positive bias of 50 V for electron collection (A) we were not able to draw a negative current from the region, suggesting a strong depletion of electrons. Appling a negative polarity (B) yielded >15 nA of positive current which suggest strong accumulation of positive charge. The strong asymmetry and depletion of electrons was relaxed at shorter distance. At 2 mm (C,D) the pair of currents were -5nA and +20nA for +50V and -50V bias, respectively. The detection limit was 0.05nA. The combination of the results of the first and second measurement, confirms that the aerosol at distances

1cm away from the arc has (i) a positive potential with respect to ground, and (ii) contains positively charged particles, being depleted of negative particles including electrons.

Finally we carried out another current measurement to estimate the effective volume number concentration n_0 in the aerosol region using known space-charge limited ion velocities.[146] We used $u_{ib} = \sqrt{\frac{2k_B T_e}{m}}(0.9107 + 0.2363\beta)$ to approximate the ion velocity where $\beta = T_b/T_e$=1 for assumed thermal equilibrium in the room temperature aerosol. We then back-calculated n_i from our measured ion current density j_i using $j_i(n_i = n_{ib}) = en_b u_{ib}$ to yield a range of n_i depending on position variant values of j_i as discussed previously.

Chapter VII

Nanocontact Electrification through Forced Delamination of Dielectric Interfaces

Jesse J. Cole, Chad R. Barry, Xinyu Wang, and Heiko O. Jacobs

Reproduced with permission from:

ACS Nano 4(12), 7492-7498 (2010)

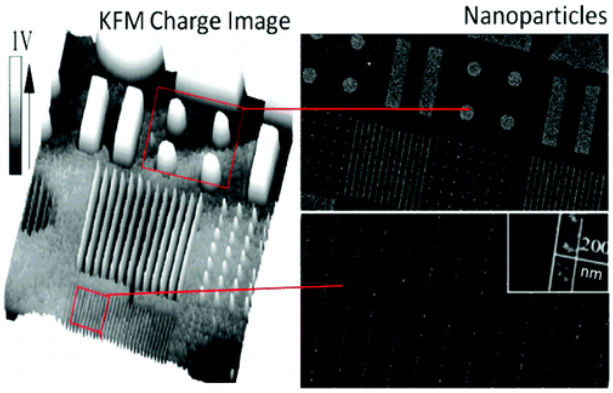

© 2011 American Chemical Society

7.1 Introduction

Charge transfer upon contact between the surfaces of two electrically neutral materials through contact electrification is a well known phenomenon which can be attributed to three fundamental processes; transfer of electrons, ions, or charged material. Contact electrification leads to uncompensated surface charges that significantly impact the force of adhesion. These forces can be very large. Measurements using point contacts between crossed cylinders recorded record levels where the electrostatic forces exceeded 6 joules per m^2 which is in the range of fracture energies for covalently bonded materials.[147] Considering the context of soft-lithography,[148] nanoimprint lithography, and nanotransfer printing,[149] the formation and fracture of conformal contacts have become mainstream and are no longer limited to single point contacts between crossed cylinders. Many techniques currently exist for the patterning of charges on a surface including direct writing[16] charges by AFM, parallel patterning[150] by contact with a thin flexible gold electrode, exposure to electron[27] and ion[151] beams, applying the photovoltaic[152] effect, and jet printing[153] of a charged solvent. The applications for these charged surfaces have been directed primarily towards the assembly of oppositely charged nanoparticles from the gas and liquid phases. When immobilized in a predetermined location nanoparticles could form the building blocks of next generation nanoelectronic devices that take advantage of nanoparticle properties including high crystallinity and large surface area. This motivates a new set of investigations into the fundamental science and applications of contact electrification at these interfaces over extended surfaces using multiple contacts of different size and shape.

This article reports a first set of experiments and results of high levels of contact electrification which occurs between poly(dimethylsiloxane) (PDMS) stamps that are brought in contact with silicon dioxide (SiO_2) and poly(methyl methacrylate) (PMMA). The experiments yield charged surfaces and associated fields that exceed the breakdown strength of air leading to strong long range adhesive forces. Proton exchange reactions established in solution chemistry are proposed to explain the observed interfacial charging. The process finds several applications. It is applied to the printing of charge, printing of nanoparticles, and charge based doping to shift the threshold voltage of thin

film transistors. Regarding the charge patterning application, the chemically driven process eliminates the need for prior[150, 154-156] conducting electrodes and external voltages to deliver and pattern charge. The charge patterns attract nanoparticles and support ~100 nm resolution prints containing <50nm Ag particles. Finally, in the context of printable electronics it is demonstrated that a contact with PDMS leads to high levels of uncompensated surface charge which affects transport in nearby semiconducting device layers which is measured in terms of transistor threshold voltage shifts which exceeded 500mV in the MOSFET devices that have been tested.

7.2 Results and Discussion

Figure 7-1 illustrates the nanocontact electrification process between insulating surfaces. PDMS was chosen as the primary contacting material and was either patterned in topography through molding[150, 154] to provide small contact areas surrounded by unchanged surface areas or it was left flat to lay down a uniform layer of charge. To clean and activate the PDMS surface (Figure 7-1A) we used a pure oxygen plasma etcher (SPI Plasma Prep II) operating at 80-100 watts at 10 Torr for 40 seconds. This process is used because it creates an energetic, hydrophilic surface that reduces transfer of uncured material during contact when compared to untreated PDMS.[157-160] Untreated PDMS did not result in high levels of charge transfer. As electrets we tested PMMA and SiO_2. The PMMA was spin-coated and baked according to standard procedures to produce a film thickness of 200 nm. The SiO_2 layer was a 160 nm thick and was generated by dry thermal oxidation. The nanocontact electrification process involves bringing the two dielectric surfaces in conformal contact (Figure 7-1B), leaving the surface in contact to react for 1 minute, and delamination. The delamination process (Figure 7-1C) yields oppositely charged surfaces patterns on each side which are characterized using Kelvin Probe Force Microscopy (KFM).[161] In addition to the KFM measurements we used a balance to record long range electrostatic attraction as a function of separation. The balance (Ohaus Adventurer) was used in combination with a micromanipulator to record force distance curves described later. In the force measurement experiments the contacting structure is mounted onto the plate of a microbalance which records a weight reduction after forced delamination.

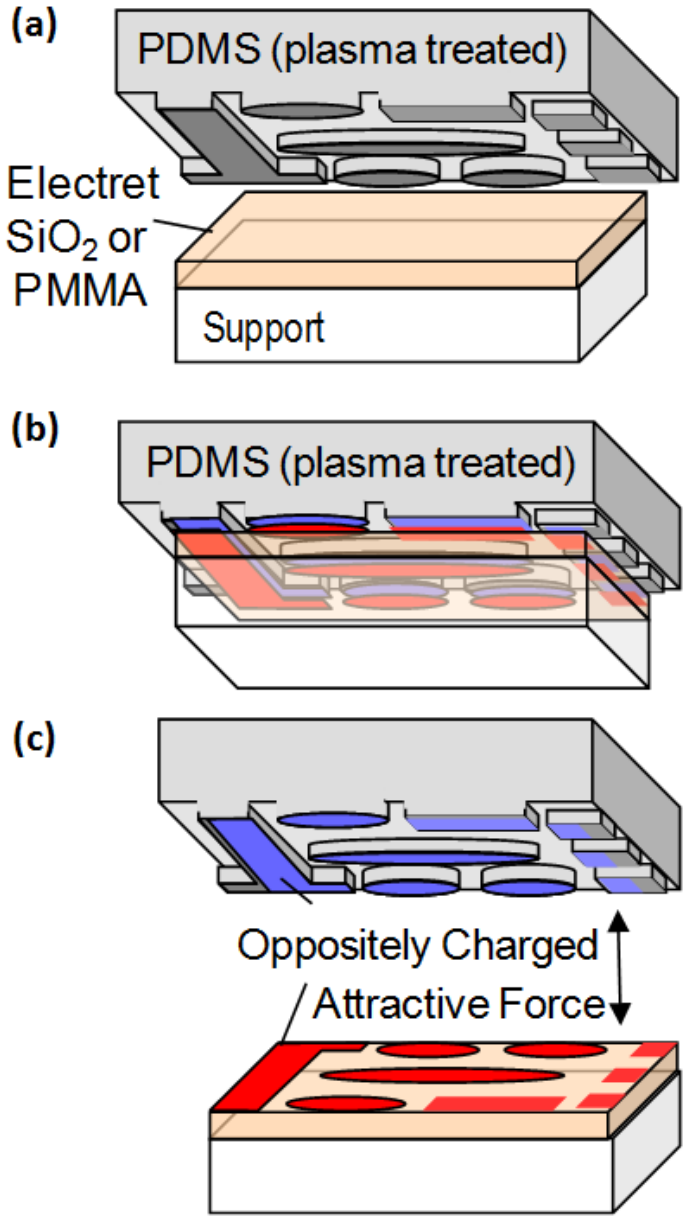

Figure 7-1. *Contact electrification process. (A) A dielectric coated substrate is placed in contact with an oxygen plasma treated, patterned PDMS stamp. (B) Charge transfer occurs at the areas of contact between both materials and leads to an increase in short range adhesion. (C) Forced delamination yields oppositely charged surfaces and long range attractive force.*

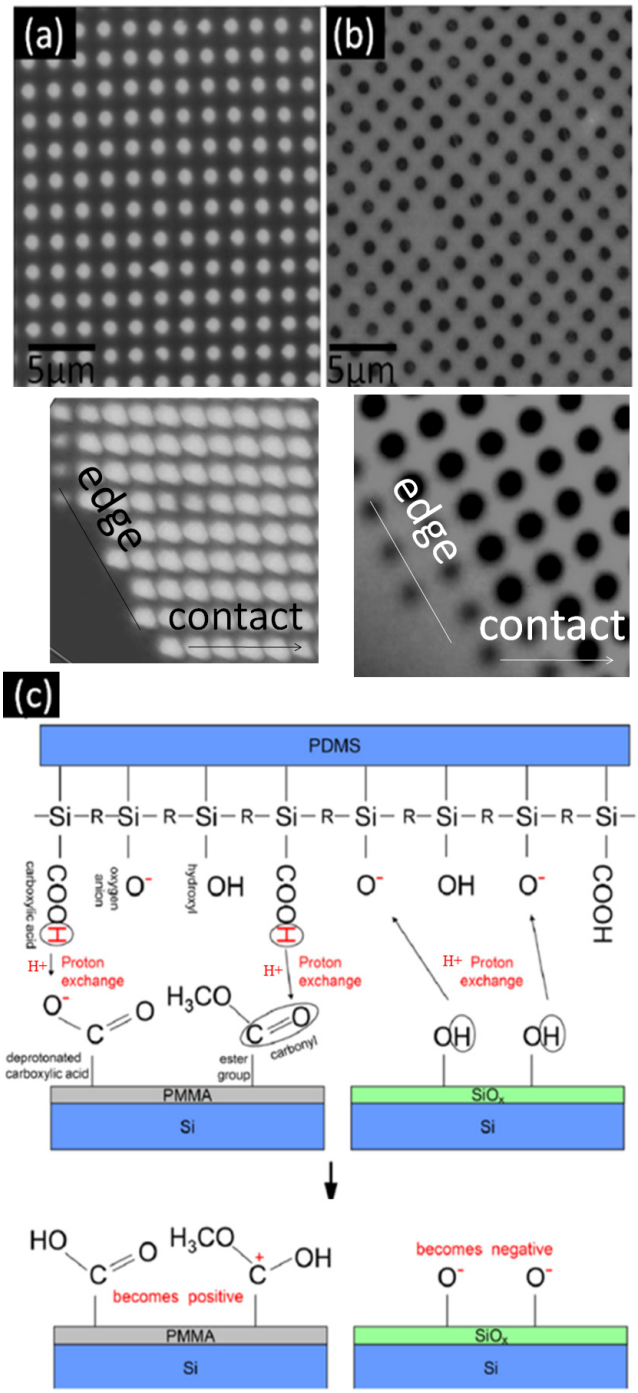

Figure 7-2. *KFM contact electrification results and charge transfer theory. (A,B) KFM images of 1 μm pitched dot patterns showing the influence of material on the polarity. (A) PMMA charged positively and (B) SiO_2 charged negatively upon contact with the same plasma activated PDMS stamp. The edge of stamp-contacted region was recorded to determine the extent of lateral charge diffusion. (C) Proposed proton exchange reaction. In the case of PMMA, hydrogen protons dissociate from the PDMS surface and attach to*

a deprotonated carboxylic acid or carbonyl site within the ester groups on the PMMA surface. The situation is reversed for SiO_2 due to the abundance of hydroxyl groups on the SiO_2 surface.

Figure 7-2 depicts the KFM images of (A) PMMA versus (B) SiO_2 surfaces after being brought in contact with PDMS and our hypothesis of the charging mechanism. Experimentally we find that PMMA charged positively at contacted areas while SiO_2 charged negatively. Localized electrification is observed after conformal contacts are delaminated. The edge of stamp-contacted region was recorded as well since it is an area where the periodic potential is disturbed. Even this region shows minimal lateral charge diffusion, however no charge patterns are observed in regions where the PDMS did not contact. The uncontacted substrate areas serve as control areas for reference to the charge patterns in the contacted areas. The recorded potential difference in KFM studies can be used as a first order estimate of the trapped surface charge density. In the illustrated example we recorded +250 mV potential difference for the 200 nm thick PMMA film which represents a charge density of 3.25 nC/cm^2 and -300 mV for the 160 nm thick SiO_2 film which represents 7.3 nC/cm^2.[46] The charging could in principle be attributed to a number of factors including material transfer. To determine if material transfer played an important role we conducted several atomic force microscopy (AFM) and x-ray photon spectroscopy (XPS) studies (shown in supplemental figure 7-S1). We found no measurable material transfer between plasma treated PDMS and untreated PMMA which is consistent with prior XPS studies by others.[157-160] Yet PMMA charges highly upon contact as shown in supplemental figure S2. In the case of SiO_2 things are more complicated and are more sensitive to the details of oxygen plasma treatment. We tested two types of plasmas with different oxygen concentrations and pressure. Specifically a 1 minute 100% oxygen plasma treatment at 100 mTorr which is used for etching (STS RIE etcher) was found to lead to covalent bonding between the PDMS and SiO_2 with a detectable amount of PDMS transferred upon forced delamination. Yet these PDMS stamps did not provide the highest level of charge and could not be used repeatedly. In contrast at 10 Torr air based 20% oxygen plasma treatment (SPI Plasma Prep II) for the same time allowed delamination of the PDMS from SiO_2 producing high charge levels

and low material transfer. The latter PDMS stamps could be used multiple times to charge a surface as will be discussed in figure 7-3. The lack of correlation between charge and material transfer combined with the ability to support successive charging leads to the conclusion that material transfer is not the dominant charging mechanism.

The working hypothesis for the charging mechanism is illustrated in Figure 7-2C and involves hydrogen proton exchange at the interface. It is known that plasma treatment attacks the Si-CH_3 bonds on the surface of the PDMS leaving very reactive silyl radicals that capture O, OH, COOH, and oxygen radicals, forming a mildly acidic and highly polar surface.[157, 159] PMMA on the other hand can be considered as being "less acidic" than plasma treated PDMS since it contains fewer surface hydrogen atoms. This creates a chemical potential difference that allows hydrogen protons to transfer during contact. After separation, the hydrogen atoms remain trapped on the PMMA surface leaving these areas positively charged. In accordance with this hydrogen proton exchange reaction theory; silicon dioxide was tested as it should yield the opposite polarity since the oxidized surface of the SiO_2 substrate has an abundance of hydroxyl groups making it "more acidic" than PDMS.

In terms of the degradation of the charging ability of the PDMS as a function of use, we found that plasma activated PDMS can be used multiple times before it needs reactivation; no measurable degradation was observed after 10 charging experiments. This observation can be explained if we compare the estimated surface charge densities (3-7 nC/cm^2) with the intermolecular spacing of the reactive sites that are available. 7 nC/cm^2 is a high level of charge which appears to be self-limited by the dielectric breakdown strength of air as will be discussed below. From a molecular standpoint, however, 7 nC/cm^2 is only one elementary charge per 40 nm by 40 nm sized area. For example, the area per silanol group is estimated to be 0.7 nm x 0.7 nm. This leads to an abundance of surface groups on the PDMS that can continue to take part in the reaction. The large quantity of surface groups supports the observation that the PDMS can be used as a charge source multiple times.

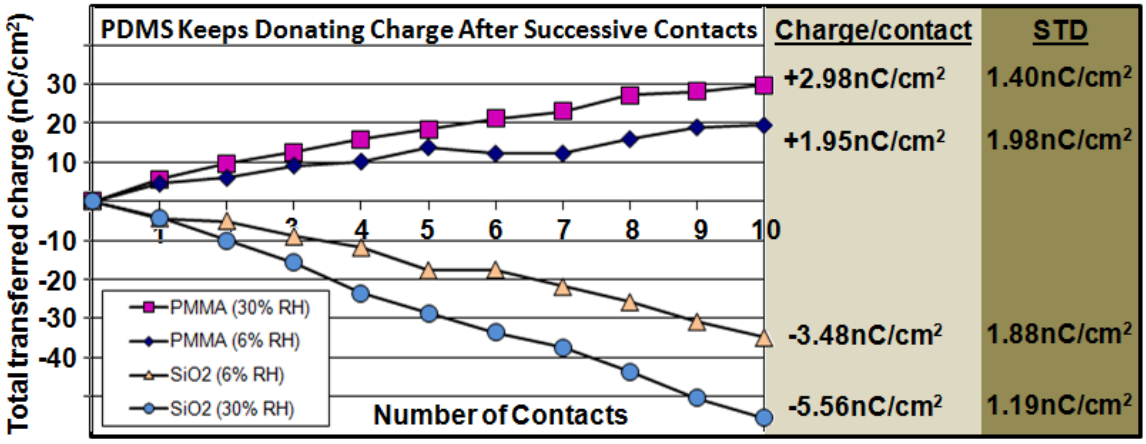

Figure 7-3. *Cumulative donated charge from a single piece of PDMS to PMMA and SiO_2 at 6% and 30% relative humidity. Repeated contact to fresh PMMA and SiO_2 surfaces resulted in continued charge transfer. The average charge per contact and standard deviation per contact are displayed next to their respective lines.*

Figure 7-3 plots the resulting amount of charge that was donated by a single piece of PDMS over successive contacts. The amount of charge that is donated in each step can be monitored by placing each freshly charged sample on a Faraday cup. The Faraday cup is connected to a Keithley 6517A electrometer which records the induced image charge which provides a direct measure of how much charge has been donated to the two dielectrics, PMMA or SiO_2. Each time the same piece of PDMS contacted a fresh dielectric surface. The figure shows PMMA in the upper half and SiO_2 in the lower half. The results show that increasing the humidity from 6% to 30% increased the amount of overall charge transferred. It has previously been reported that water plays an important role in triboelectric charging of toner particles and polymers[162-164] where faster charging was observed[165] at higher relative humidity. A similar trend was observed in a more recent and unrelated study that reported that surface can be charged through gas-surface reactions. The authors changed the relative humidity[166, 167] and found higher levels of uncompensated surface charge at raised humidity. In our case the increased charge levels could be explained by the polymeric amorphous and hydrophilic structure of oxygen plasma treated PDMS which leads to a greater uptake of water and ionic species to participate in the ion transfer.

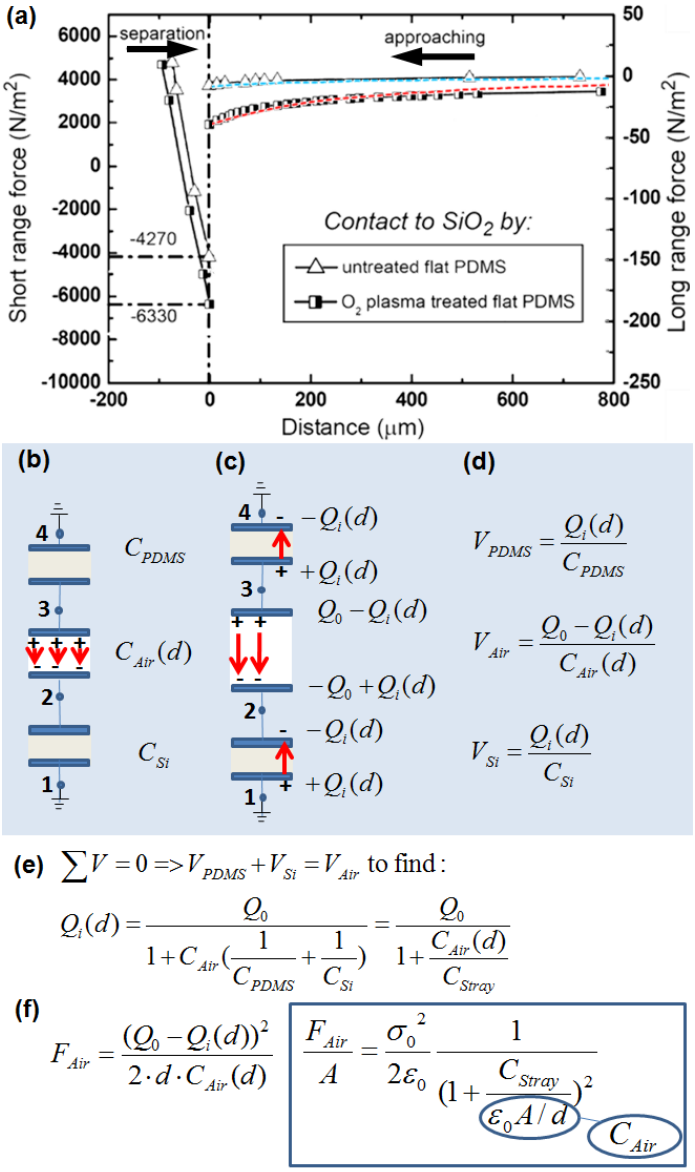

Figure 7-4. *(A) A force distance curve for conformal contact between SiO_2 and plasma treated PDMS next to untreated PDMS. The left side depicts short range adhesive forces. The right side depicts long range Coulomb attraction and is fit to a stray capacitance model (blue and red dashed lines). As the two surfaces are separated (B,C) charges in nearby grounded copper plates are drawn resulting in a separation-dependent electric field. (D) The potentials on these surfaces can be related capacitively to the plate charges such that (E) applying Kirchhoff's voltage law allows an estimate of the reduced electric field and (F) corresponding reduction in force.*

Using the KFM based estimated 3-7 nC/cm^2 of uncompensated surface charge we can evaluate the resulting electric field $\boldsymbol{E=\sigma/\varepsilon_0}$ where $\boldsymbol{\sigma}$ is the surface charge density, and $\boldsymbol{\varepsilon_0}$ is the permittivity of air gap that is formed. The estimated values for the electric field are 3.5 x10^6 V/m for PMMA and 8x10^6 V/m for SiO_2 which exceeds the dielectric breakdown strength of air (~3x10^6 V/m) published for macroscopic electrodes. The closeness of these values to the theoretical limit raises the issue if the observed charge levels are limited or self-regulated by dielectric breakdown strength of air. In principle it could be possible that electrostatic discharge takes place during charge separation which limits the charge level to the reported values. Short range discharge phenomena between separating surfaces have been reported by Horn *et al.*[147] using surface force apparatus measurements; the observed abrupt reductions in the Coulomb attraction were attributed to a stepwise reduction in the remaining uncompensated charges. These types of discharges occur over short distances and may therefore not be accompanied with light flashes and popping sounds that can be detected by simple observation. While discharges may be present and self-limiting they did not result in localized pockets where complete neutralization took place.

A consequence of separated charges at the interface will be an attractive force which can be estimated using $\boldsymbol{F/A = \sigma^2/2\varepsilon_0}$ where $\boldsymbol{A}$ is the contact area. The estimated electrostatic attraction based in KFM data exceeds 100 N/m^2 suggesting that the charged surface could lift ~9 kg/m^2. To directly measure this estimated attraction we mounted the contacting structure on a balance which monitors the produced lift force after separation. **Figure 7-4A** shows the force-distance curves which were measured by recording the weight reduction as a function of separation for SiO_2 substrates after contact with untreated and oxygen plasma treated PDMS. The reference is untreated PDMS which provides low levels of contact electrification and low Coulomb attraction. The left side of the graph plots the overall adhesive force before separation occurs (no airgap, short range force scale to the left). The right side of the graph plots the attractive Coulomb force as the substrates reapproach the previously contacted PDMS surfaces (with airgap, long range force scale to the right). The required force to pull the two plane-parallel surfaces apart (left) is typically two orders of magnitude larger than the maximum long range attractive force with an airgap in place (right). At present the long range attractive

force across an airgap reaches 50 N/m^2 before the two surfaces snap into contact. This is the highest possible data point we have recorded so far. The last data point is difficult to record as it depends on how parallel the surface are when they reapproach each other which may also explain the discrepancy between this ~50 N/m^2 value and the KFM based estimate which predicted >100 N/m^2. However, both KFM and direct force measurements confirm that the values for the charge density, electric field, and forces are near the theoretical limit set by the dielectric breakdown of air.

In our force-distance measurements the PDMS and electret surfaces were mounted on grounded copper plates as depicted schematically in figure 7-4B which act as Faraday cups which provide the ability to monitor image charges. Image charges are a direct result of stray capacitances to nearby conductors and dielectric materials that surround the charged layers. Figure 7-4C shows that any stray capacitance will reduce the measured long-range force of adhesion as the separation is increased. In other words the force is not constant as suggested by the previously discussed equation where the force density $\boldsymbol{F/A=\sigma^2/2\varepsilon_0}$ is independent of separation *d*. A more accurate model for the force-distance curves can be found following figure 7-4D and 7-4E. The result is shown in figure 7-4F using $\boldsymbol{F/A= \sigma^2/2\varepsilon_0 * 1/(1 + C_{stray}/ [\varepsilon_0 A/d])^2}$ where $\boldsymbol{C_{stray}}$ is related to stray capacitance of the charged surfaces to both grounded copper plates. The model is derived by applying the integral form of Gauss' law around the top and bottom electrodes followed by superposition of the respective electric fields. For the $\boldsymbol{d=0}$ limit case the force reduces to the equation $\boldsymbol{F/A=\sigma^2/2\varepsilon_0}$ discussed earlier to estimate transferred charge densities and the image charges in the nearby copper mounting plates are negligible.

Figure 7-5 discusses applications of uncompensated surface charges. Figure 7-5A shows an application where the recorded charge pattern (left, KFM image) is used to attract nanoparticles (right, SEM image). In the given example, <50 nm sized negatively charged silver particles were deposited directly from the gas phase using a previously reported nanomaterial source.[154, 155] The image demonstrates that the field is strong enough to attract the particles to the charged areas with 200nm resolution.

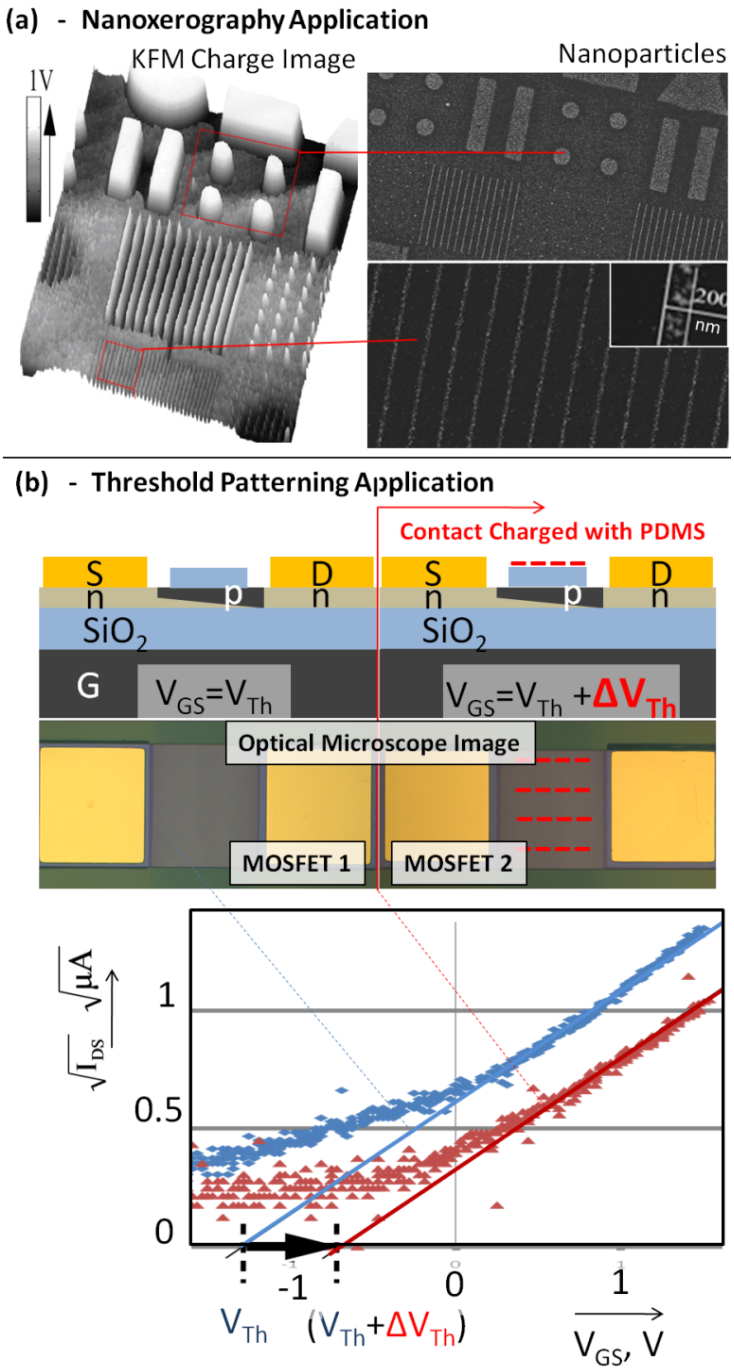

Figure 7-5. *Applications of contact electrification in nanoxerography and thin film electronics. (A) KFM charge images and corresponding 200 nm resolution nanoxerography nanoparticle prints. (B) Thin film electronics application showing schematic, optical microscope image, and* $\sqrt{I_{DS}}$ *vs.* V_{GS} *plot of charge patterned MOSFETs achieving a threshold voltage shift of 580mV.*

Figure 7-5B shows that contact electrification can also be used to alter electronic transport in nearby semiconducting device layers. In the demonstrated application patterning of charge is used to alter the threshold voltage of thin film Si transistors from one area to another. Figure 7-5B shows a device schematic before (left) and after contact (right); full fabrication details are described in the methods section. The I_{DS} vs. V_{GS} transistor curves shown were taken using the handle wafer as a back gate. We used the x-axis intercept of $\sqrt{I_{DS}}$ vs. V_{GS} line to evaluate the threshold voltage.[168] For SiO_2 the threshold voltage applied to the back gate shifts to a 580mV higher voltage which is consistent with the expected presence of negative surface charge on the SiO_2 surface.

7.3 Conclusion

In conclusion the cleavage of conformal contacts, which has become a common procedure in areas of soft-lithography and other soft-printing processes, typically leaves behind large amounts of surface charge as the surfaces are delaminated. While these surface charges remain undetected with most commonly applied spectroscopic measurement techniques including XPS and FTIR, direct evidence can be gained through Kelvin probe force microscopy and force distance curve measurements. The recorded charging levels can be very high and the upper levels seem to be self-limited by the dielectric breakdown strength of air. The separated charges give rise to an electrostatic force of adhesion that can be detected over millimeter distances, exceeding 50 N/m^2 in some cases. The corresponding force distance curves depict a phenomenological relationship between short and long-range attractive forces. The presented explanation suggests a two-step process whereby the formation and delamination of interfaces bonded by ions precedes contact electrification and the generation of long-range electrostatic forces. SiO_2, PS, PAA, PMMA, and SU-8 are all commonly used in the processing of semiconductor devices. We therefore expect that our findings will impact areas which go beyond the demonstrated charge directed assembly and transfer applications. Specifically the emerging field of printable and flexible electronics could be impacted, where contact printing methods and delamination of interfaces are used to print and transfer materials. We anticipate that the presence of high levels of uncompensated charges may alter the

functionality of various electronic devices including FETs unless models take these extra gate charges into account. The additional challenges are particularly relevant in the context of flexible electronics where thin semiconductors, polymer insulators, and conformal contacts are widely employed.

7.4 Experimental Methods

PDMS fabrication and surface treatments: PDMS fabrication for this study was unaltered from the commonly accepted technique. Specifically we mixed 30g elastomer (Sylgard 184) and 3g curing agent (also Sylgard 184) together for about 2 minutes at room temperature. Mixing caused gas bubbles to form, so uncured PDMS was degassed in a vacuum chamber at ~30 Torr for 20 minutes. The uncured PDMS was poured onto silanized silicon, then degassed again for 1 hour at ~20 Torr. (The silicon may also be patterned with S1813 photoresist prior to treatment with octadecyltrichlorosilane if features were desired for the finished PDMS.) The degassed PDMS is cured in a convection oven at 60^{o}C for 12 hours. The cured PDMS was inserted into a commercially available plasma cleaner (SPI, model Plasma Prep II) for oxygen plasma treatment. The system was purged with 99.99% oxygen, then the 80-100W 13.56MHz RF plasma was operated at 10 Torr for 40 seconds.

Thin-SOI MOSFET fabrication: Fabricating the charge-sensitive thin-SOI MOSFETs involved n-well doping, mesa etching, contact deposition, annealing, and insulator deposition. Each step used a pattern and etch-back process to avoid any debris that may be caused by liftoff processes. Beginning with 150mm diameter p-type Si on insulator wafers (SOITEC, inc.) with a 100nm Si device layer on a 200nm buried oxide, we deposited 300nm SiO_2 by PECVD at 340°C. To define the dopant mask S1805 photoresist was photolithographically patterned then given a 30s oxygen plasma descum, and the underlying SiO_2 was etched in 10:1 buffered oxide etch (a mix of HF and NH_4F in H_2O) for 150s. The photoresist was removed by rinsing with acetone, methanol, and isopropyl alcohol. Phosphorus containing n-type spin-on dopant was spun on the wafer and then driven in by rapid thermal annealing at 900°C for 10s under 6sLpm flow of 10% oxygen in nitrogen. The oxidized spin-on dopant was stripped in 49% HF for 120s. The sample was coated with 50nm SiO_2 by PECVD at 340°C to prevent metal from

contacting p-Si, then windows to the n-wells were opened in the SiO_2 by photolithography, 30s oxygen plasma descum, and etching 30s in 10:1 BOE. Photolithography and oxygen descum was used to define ribbons of p-n-p silicon then 10:1 BOE removed the oxide, a 30s 20W 40mTorr $SF_6/Ar/O_2$ plasma etch removed silicon down to the buried oxide, and the photoresist was removed. Metal contacts were deposited by DC sputtering using a quartz crystal monitor to measure the film thicknesses. Both top(source/drain) and back(gate) contacts were 150nm Au with a 5nm Cr adhesion layer. The contacts were patterned by photolithography, oxygen plasma descum, etching 25min in 10:1 DI H_2O:GE-6 gold etchant, and a 60s dip in 4:1 DI H_2O:CR-12S chrome etchant. The contacts were annealed by RTA at 400°C for 20s in 8sLpm forming gas (5%H_2 / 95%N_2).

7.5 Supplemental Information

The XPS studies of PDMS material transfer to PMMA by contact were performed by tracking Si content. Supplemental figure 7-S1 depicts XPS data showing Si content on (A) the PDMS surface with greatest intensity at 103.4eV which corresponds to the Si $2p^3$ peak. Since PMMA (chemical formula $[C_5H_8O_2]_n$) contains no Si and PDMS (chemical formula $[C_2H_6OSi]_n$) does contain Si it is possible to use XPS to track material transfer. As a control sample Si was not detected (B) on the PMMA surface before contact. Following contact with oxygen plasma treated PDMS (C) the surface still did not show any Si-related peaks with the conclusion that no PDMS material transferred to the PMMA.

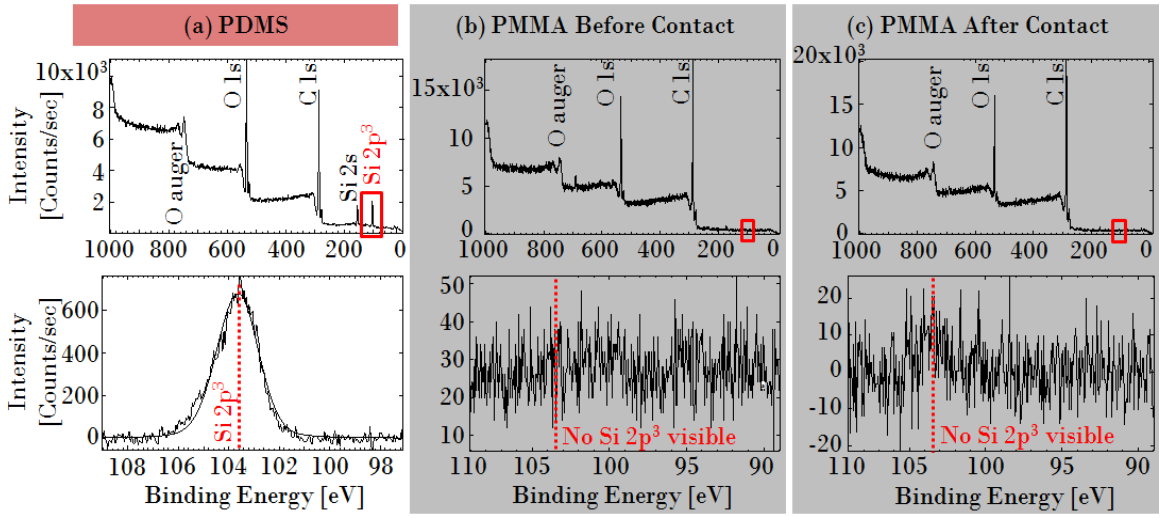

Figure 7-S1. *XPS study of material transfer from PDMS (A) to PMMA (B,C) by contact. Carbon and oxygen peaks are visible in each case, but only PDMS showed silicon peaks below 200eV. (Top row) The overall traces were narrowed (red boxes, top row) to determine peaks in the appropriate range (bottom row) for the binding energy range for Si. The silicon content of PDMS* $[C_2H_6OSi]_n$ *is measurable as a* $2p^3$ *peak at 103.4eV (red dotted line, bottom row). The plots show the lack of Si content on PMMA (B) before and (C) after contact with PDMS so it is concluded that no PDMS material transferred to the PMMA.*

As shown in supplemental figure 7-S2 (top row) the AFM traces (A) for PMMA contacted by PDMS show no topography which supports the lack of material transfer by contact even with levels of transferred charge near +1V as measured by KFM (B). For the case of SiO_2 we observed material transfer to depend strongly on plasma parameters such that exposure to O_2 and N_2 containing air plasma for 1min or less reduced material transfer below AFM resolution limits as indicated in the supplemental figure 7-S2 (bottom row).We found that higher plasma O_2 content and longer treatment times resulted in increased PDMS material transfer to the SiO_2 such that the amount of material was visible in AFM scans. These structures were not always charged and the PDMS stamps could not be used repeatedly. Best charging results in terms of repeatability and amount of charge transferred were achieved using a 10 Torr air based 20% oxygen plasma treatment (SPI Plasma Prep II) for 1 minute which allowed clean delamination and uniform charging as shown in the figure.

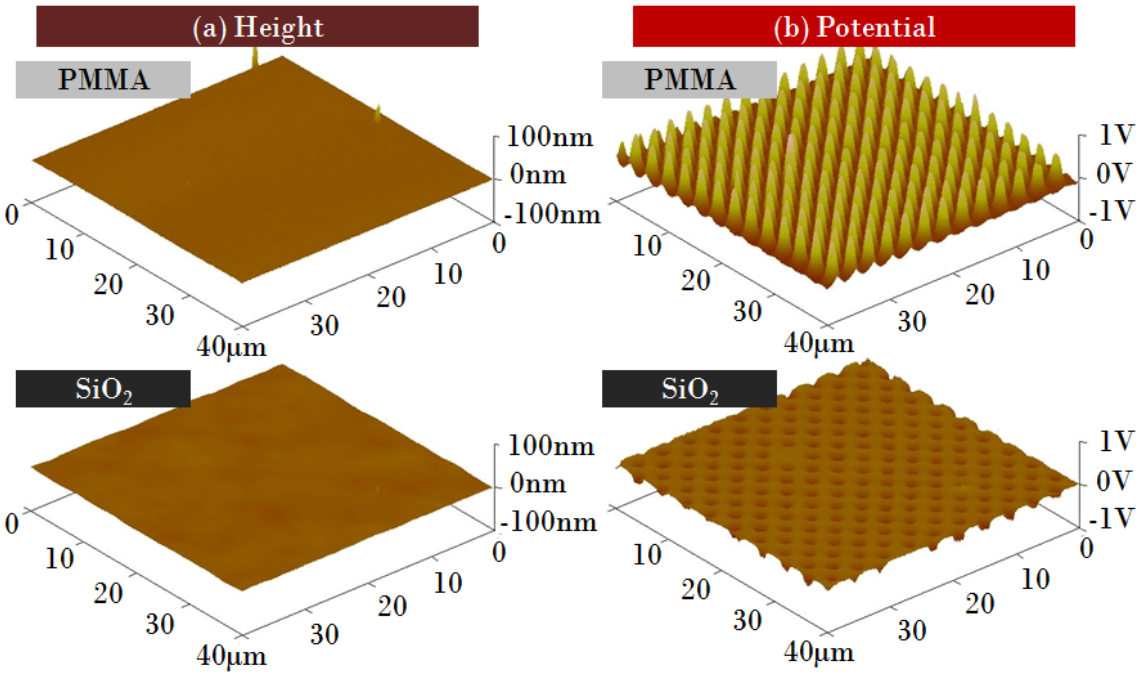

Figure 7-S2. *(A) AFM topography data with (B) corresponding KFM charge data for PMMA (top) and SiO_2 (bottom) after contact with PDMS. Lack of topography in both cases indicates minimal if any material transfer occurred during contact while the charge patterns are well resolved and opposite in polarity.*

Chapter VIII

Nanocontact Electrification: Patterned Surface Charges Affecting Adhesion, Transfer, and Printing

Jesse J. Cole, Chad R. Barry, Robert J. Knuesel, Xinyu Wang, and Heiko O. Jacobs,

Reproduced with permission from:

Langmuir 27(11), 7321-7329 (2011).

© American Chemical Society 2011

8.1 Introduction

The basic phenomenon of electrification by contact is well known and can be attributed to three fundamental processes: material transfer, ion transfer, or electron transfer. Electron transfer dominates if at least one of the materials is a semiconductor or a metal with free electrons.[103] If both materials are insulators, the fundamental charge transfer mechanism cannot be explained on the basis of electronegativity alone and requires the consideration of the chemical nature of all functional groups.[104] This becomes increasingly complicated if polymeric insulators are used. In all cases, contact electrification leads to uncompensated surface charges that impact the force of adhesion. For example, surface force apparatus measurements by Horn et al.[105] demonstrated that the electrostatic force of adhesion between crossed insulating cylinders can exceed 6 joules per m^2 which is comparable to the fracture energies of covalently bonded materials. We note that the reported values [105] were exceptionally large, exceeding anything that had been reported before and perhaps possible considering the breakdown strength of air. Considering the context of soft-lithography[106], nanoimprint lithography, and nanotransfer printing[107], the formation and fracture of conformal contacts have become mainstream and are no longer limited to single point contacts. This enables a new set of investigations into the fundamental science and applications of contact electrification over extended surfaces using multiple contacts of different size and shape.

As a first step in this direction we report on controlled delamination experiments between polydimethylsiloxane (PDMS) and other common dielectrics to quantify and monitor charge transfer and the subsequent electrostatic force of adhesion. In addition to the commonly used tables of electronegativity, we identified that proton exchange reactions established in solution chemistry provide the best approach to explain interfacial charging between the dielectrics that we investigated so far. The dielectrics include polymethyl methacrylate (PMMA), epoxy photoresist (SU-8), polystyrene (PS), polyacrylic acid (PAA), and silicon oxide (SiO_2). The magnitude of electrification can be adjusted through surface functionalization of the PDMS and reach values close to the physical limit near the dielectric breakdown strength of air. The uncompensated charges yield a long range electrostatic attractive force of 150 N/m^2. Corresponding force

distance curves show a phenomenological relationship between long and short range attractive forces where a controlled increase in the recorded long range electrostatic force equates to a stronger short range adhesion. The gained knowledge finds several applications: in the context of laterally confined charge patterning with sub 100 nm lateral resolution, it extends previously reported serial scanning probe[16] and electric nanocontact charging techniques as it can pattern samples that are at least 100 times larger than what has been reported while maintaining the same high lateral resolution. Moreover previous[12, 14-16, 108] charging processes required a conducting substrate underneath the dielectric. The reported process eliminates this requirement as well as the requirement that an external voltage has to be applied to the sandwiched structures to inject and transfer charge at the interface. In the context of Nanoxerography, it is demonstrated that the chemically driven charge patterned surfaces prepared by nanocontact electrification can be developed into visible patterns using charge directed deposition of nanoparticles. In the context of transfer printing, it is demonstrated that the strong adhesive forces that stem from uncompensated surface charges can be used to transfer semiconducting components from one substrate to another whereby the size of the components can span 3 orders of magnitudes. Finally, in the context of printable electronics it is demonstrated that a contact with PDMS leads to high levels of uncompensated surface charge which affects transport in nearby semiconducting device layers which is measured in terms of transistor threshold voltage shifts which exceeded 500mV in the MOSFET devices that have been tested. Threshold voltage shifts were found to depend on the covering material such that threshold voltage was adjusted positively (or negatively) after contacting SiO_2 (or PMMA) covering the n-channel FET.

8.2 Results and Discussion

Figure 8-1 illustrates the basic nanocontact electrification measurement procedure. PDMS was chosen as the primary contacting material because of its wide use in today's scientific world. For lateral charge patterning experiments PDMS stamps were prepared with raised posts through molding[12, 14] which provides small contact areas alongside an unchanged reference. For transfer experiments we left the surface flat and unpatterned. To investigate the transfer of charge, electret coated chips (PMMA, SU-8, PS, PAA, and SiO_2) with film thicknesses around 100-200 nm[169] were placed onto the PDMS stamps and left in contact for 1 minute before forced delamination. Untreated PDMS substrates left residues on the contacted surfaces and did not provide reproducible results. To clean and activate the PDMS surface we used a pure oxygen plasma etcher (SPI Plasma Prep II) operating at 80-100 watts at 10 Torr for 40 seconds. This process is commonly used because it creates an energetic, hydrophilic surface that reduces transfer of uncured material during contact when compared to untreated PDMS.[170-173]

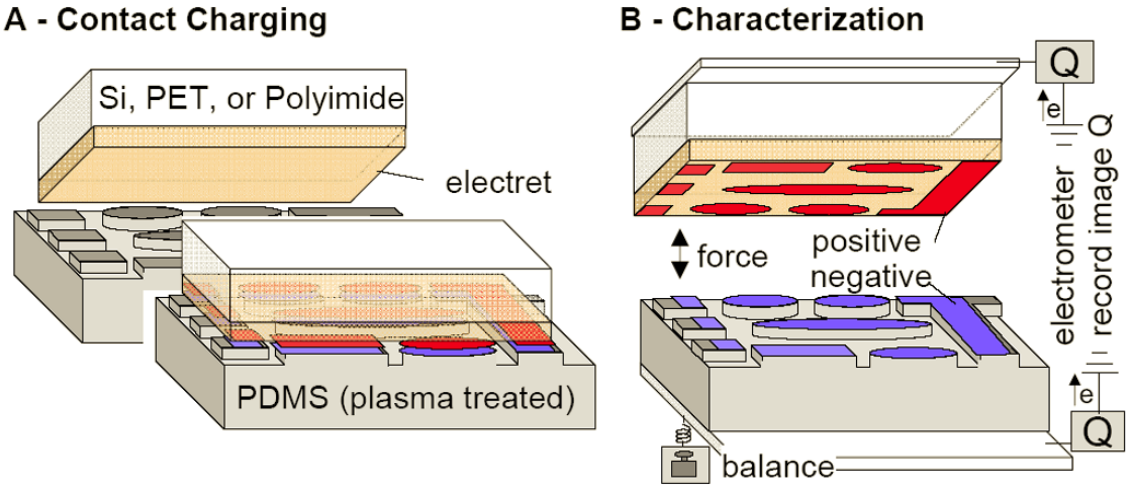

Figure 8-1. *Contact electrification process and measuring procedure. A) A dielectric coated substrate is placed in contact with an oxygen plasma treated, patterned PDMS stamp. Charge transfer occurs at the areas of contact between both materials. B) An electrometer records the amount of accumulated image charges on metallic plates holding both the substrate and stamp. A connected balance records the weight reduction of the stamp as the charged substrate is separated, and then again during re-approach (see Figure 8-S1 for a photograph of the actual implementation).*

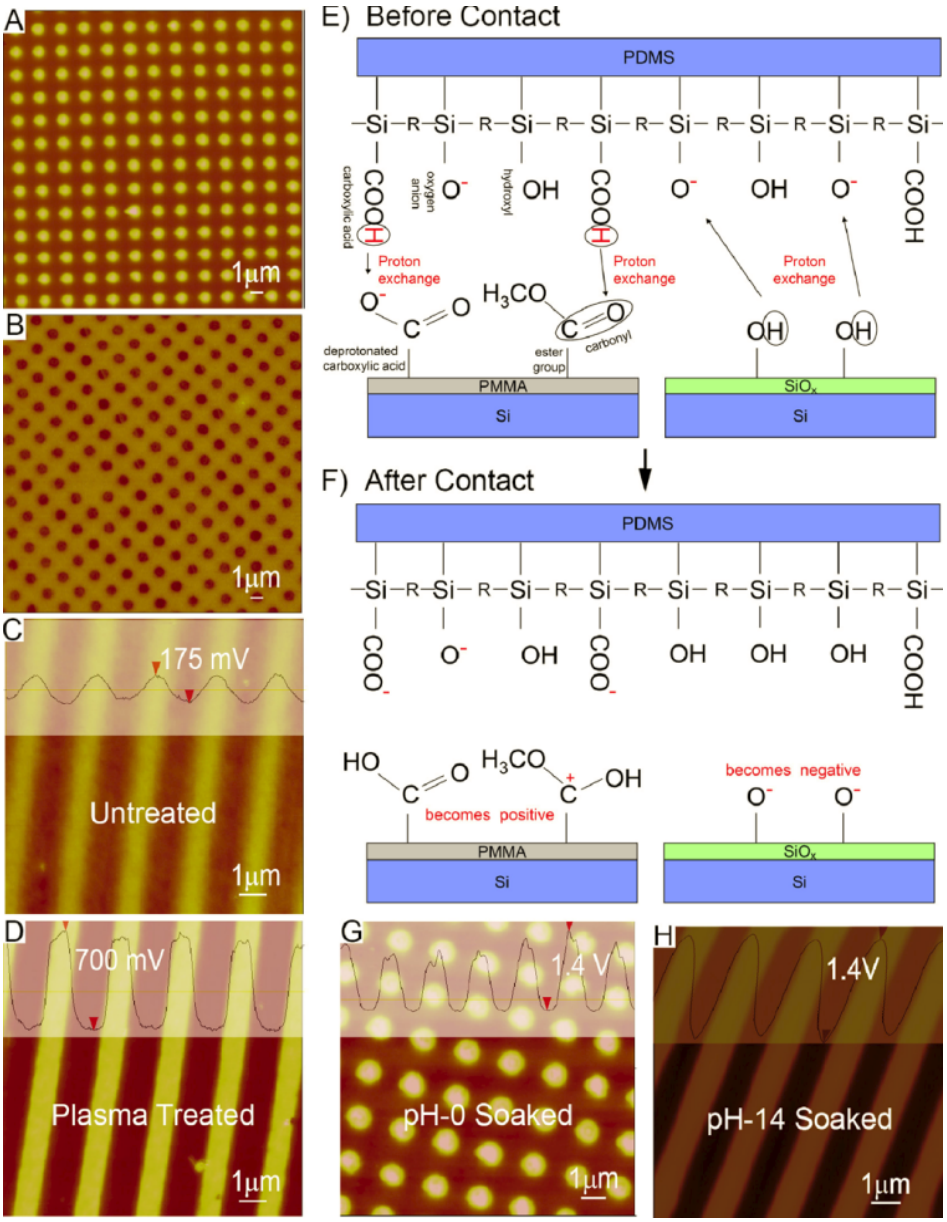

Figure 8-2. *KFM contact electrification results, charge transfer theory, and control experiments. (A-D) KFM images of 1 μm pitched dot and line type patterns showing the influence of material and plasma treatment on the polarity and charge concentration. (A) PMMA charged positively and (B) SiO_2 charged negatively upon contact with the same plasma activated PDMS stamp.(C, D) Plasma treatment of the PDMS yields a 4 fold increase in the surface charge on PMMA. (E, F) Proposed proton exchange reaction between plasma treated PDMS and both PMMA and SiO_2. In the case of PMMA, hydrogen protons dissociate from the PDMS surface and attach to a deprotonated carboxylic acid or carbonyl site within the ester groups on the PMMA surface. The*

situation is reversed for SiO_2 due to the abundance of hydroxyl groups on the SiO_2 surface. (G, H) KFM control experiments to enhance charge transfer by pH surface treatment of the PDMS stamp prior to contact. (G) pH0 treatment increases the positive surface charge on PMMA and (H) pH14 treatment increases the negative surface charge on SiO_2.

To quantify the level of contact electrification as a result of forced delamination, we analyzed all samples using Kelvin probe force microscopy (KFM) immediately after cleavage. KFM records the surface potential distribution and provides a direct measure of the amount of electrification with respect to areas that have not been contacted.[174] While the level and polarity varied, localized electrification is observed at high levels after conformal contacts are delaminated. During the formation and delamination process, no lateral frictional forces or sliding motion was applied which is different from other more classical implementations also aimed at producing high levels of uncompensated charge. **Figures 8-2(A, B)** illustrate the associative effect of the electret material, in this case PMMA versus SiO_2, on the polarity of the produced patterns. Specifically, PMMA charged positively at contacted areas while SiO_2 charged negatively. Figures 8-2(C, D) reveal the effect of plasma treatment of the PDMS on the charge concentration. Without plasma activation (Fig. 8-2C) the highest level of charge was at least a factor of four smaller than that achieved by contacting the samples with plasma treated stamps (Figs. 8-2A, B, D, G, H).

The illustrated nanocontact electrification process could in principle be attributed to a number of factors including material transfer. To determine if substantial material transfer is required and involved we conducted several AFM topography measurement and x-ray photon spectroscopy (XPS) studies. We found that no substantial material transfer is required to cause charging as shown in Figures 8-S2 and 8-S3. For example, no measurable material transfer after contact between plasma treated PDMS and untreated PMMA was recorded which is consistent with prior XPS studies done by Uhrich *et al.*[173, 175]. Yet high levels of contact electrification was observed for this interface as shown in Figure 2D which means that the charging cannot be explained by simple material transfer. Since a measureable amount of material transfer (i.e. more than

a single monolayer) is not required the process must be dominated by small molecular changes such as interfacial ion or electron transfer.

The working hypothesis of the charging mechanism for the materials studied is illustrated in Figures 8-2(E, F) and involves hydrogen proton exchange reactions at the interface similar to acid-base reactions in solution chemistry. While we limit our discussion to PMMA and SiO_2, the other tested materials follow the same general theme: chemically driven proton exchange more suitably explains the observed results than looking at the macroscopic electronegativity alone. In this case, plasma treatment attacks the $Si\text{-}CH_3$ bonds on the surface of the PDMS leaving very reactive silyl radicals that capture O, OH, COOH, and oxygen radicals, forming a mildly acidic and highly polar surface.[170, 172] Many polymers, such as PMMA, contain polar end groups that can participate in ionic charging and interfacial reactions. The ester end group in PMMA for example is slightly positive. PMMA can also be considered as being "less acidic" than plasma treated PDMS since it contains fewer surface hydrogen atoms. This creates a chemical potential difference that allows hydrogen protons to transfer during contact as illustrated in the schematic (left sides of Fig. 8-2E,F). After separation (Fig. 8-2F), the hydrogen atoms remain trapped on the PMMA surface leaving these areas positively charged as observed in Fig. 8-2A. In accordance with this hydrogen proton exchange reaction concept; silicon dioxide (right sides of Fig. 8-2E,F) should yield the opposite polarity since the oxidized surface of the SiO_2 substrate has an abundance of hydroxyl groups making it "more acidic" than PDMS. The hydroxyl groups provide hydrogen ions to react with the oxygen ions on the PDMS, leaving a negative charge on the SiO_2 surface as observed in Fig. 8-2B. In short, the deprotonated PMMA accepts protons from the PDMS while the SiO_2 donates protons to the PDMS.

We tested protonation/deprotonation further by loading the PDMS with acids and bases. In the case of PMMA (proton acceptor), contact to a highly protonated PDMS stamp (referred to as pH0 treated) increased the amount of positive charge transfer to the PMMA (Fig. 8-2G). In the case of SiO_2 (proton donor), contact to a highly deprotonated

PDMS stamp (referred to as pH14 treated) increased the amount of negative charge transfer to the SiO_2 (Fig. 8-2H). In these depicted results we soaked the stamps for 1 hour in an acidic buffer solution of 1M hydrochloric acid in water in one case (pH0 treated) and a basic solution of 1M sodium hydroxide in water in the other (pH14 treated). After removing the stamp from the pH solutions we quickly (2 seconds) rinsed the surface with deionized water and then blew it dry with nitrogen. The rinsing of the pH14 treated PDMS stamp removes any potential salt residues which would otherwise prevent formation of uniform conformal contacts. Our interpretation of the observed increase in charging (Fig. 8-2G,H) is that the 2s rinsing step does not completely remove the level of protonation/deprotonation acquired during the 1h pH soaking step of the permeable plasma-treated PDMS surface layer.

The recorded potential difference in KFM studies can be used as a first order estimate of the trapped surface charge density. For example a recorded 1.5V potential difference (Fig. 8-2G) for a 200 nm thick PMMA film represents a charge density of ~10 nC/cm^2.[176] Faraday cup and force-distance measurements can also be used to confirm these values. The electrometers and microbalance shown in Figure 8-1B and the photograph Figure 8-S1 were added to the experimental process to measure the amount of charge that is transferred at the interface and the subsequent electrostatic force of adhesion. In the electrometer arrangement, both stamps and substrates are placed onto metallic plates which act as Faraday cups that accumulate image charges equal but opposite in sign to the charge on the surface of the materials.[177]

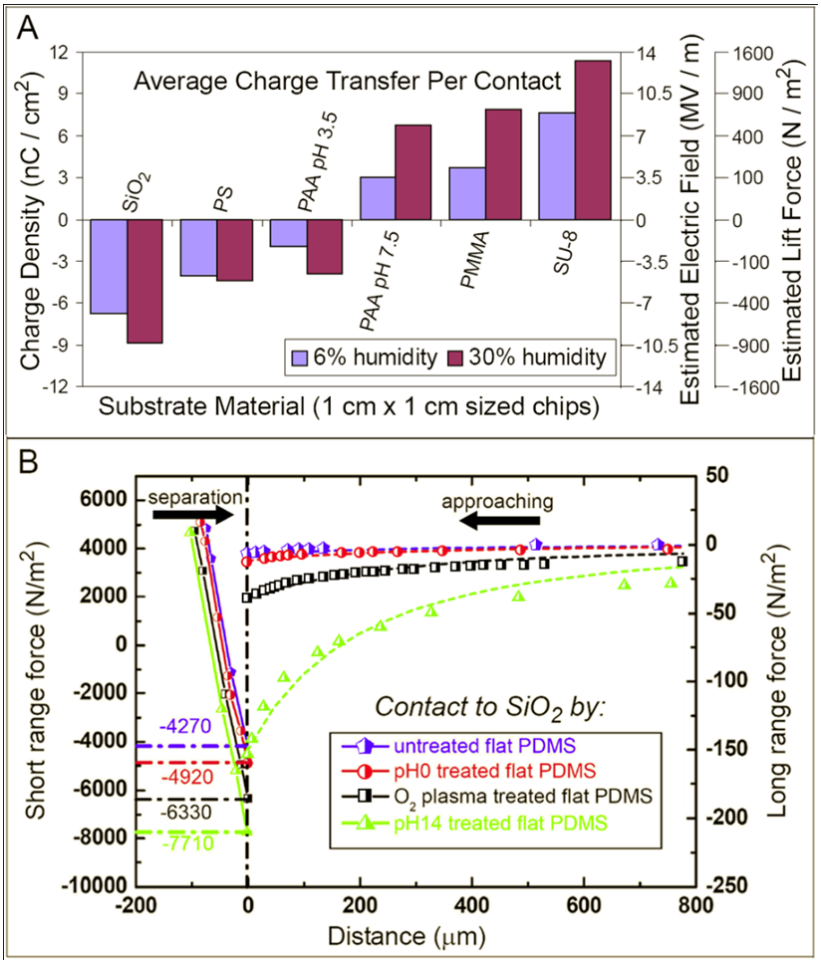

Figure 8-3. *Recorded charge levels on various materials and resulting short and long range force. A) Average Faraday cup electrometer recordings at 6 and 30% relative humidity for six different electret materials after contact electrification with oxygen plasma treated PDMS. Electric field and adhesive force values estimated from the charge density measurements are also displayed. B) Force distance curves have two regimes that describe the force distance relationship up to the point of separation (left, short-range) and during re-approach (right, long range). The curves show untreated, pH0 treated, O2 plasma treated and pH14 treated PDMS that is brought in contact with SiO_2. The long range force distance curves follow a stray capacitance model (dashed lines) which considers the coupling of the printed charges to nearby conducting surfaces which reduce the attractive force as the separation is increased.*

Figure 8-3A provides a summary of the recorded charge levels for six different electret materials (SiO_2, PS, PAA at pH 3.5, PAA at pH 7.5, PMMA, and SU-8) contacted by plasma treated PDMS at 6 and 30% relative humidity. Out of the six different electrets materials SiO_2 charged the most negative and SU-8 the most positive. Polyacrylic acid (PAA, from Sigma Aldrich) was used as an example where the polarity of charge transfer can be altered. Polyacrylic acid was originally purchased in a pH 7.5 formulation and then the pH was adjusted to 3.5 by the addition of dilute hydrochloric acid HCl as measured by a silver ion pH meter. We tested 100 nm of spin coated PAA with a pH of 3.5 which predictably resulted in a negative charge on the PAA surface after contact with PDMS (Fig. 8-3A); the more acidic PAA-3.5 has more hydrogen protons to donate to the PDMS which means that contacted areas become negatively charged. In a second experiment we reverse the contact charge polarity by using polyacrylic acid thin film that was prepared using a PAA solution with an increased pH of 7.5. This can again be explained because the now deprotonated PAA-7.5 receives hydrogen protons from PDMS during contact resulting in the acquired positive charge.

As shown by the chart (Fig. 8-3A) the contact charging process depends on the relative humidity. Increasing the relative humidity from 6% to 30% increased the charge differential for all materials. The changes were not as dramatic outside the 6-30% window. This dependence again points towards charging that is driven by ion exchange rather than material or electron transfer; higher humidity will increase the amount of surface water which mediates the diffusion of ions across the interface as the chemically different surfaces are brought into contact. The chart also shows values for the estimated electric field strength, **E**, and estimated electrostatic force of adhesion, ***F***, which can be directly calculated from the electrometer measurements using $E=\sigma/\varepsilon$ and $F=A\sigma^2/\varepsilon$, where A is the contact area, σ is the surface charge density, and ε is the permittivity of air. The calculated electric field strength based on the measured charge density ranged between 1-4 times the dielectric breakdown strength of air (~$3x10^6$ V/m) published for macroscopic electrodes. Interestingly the values for the charge levels are very large but less than record levels by Horn *et al.*[105] that imply even higher electric fields. We believe that the closeness to the breakdown strength of air in our case points to a self-limiting behaviour. The closeness suggests that the upper level may be limited by

partial discharge across the air gap as it forms; the existence of partial discharge has previously been reported[105]. In our case the calculated electrostatic force of adhesion, $\mathbf{F}=A\sigma^2/\varepsilon$, using the measured charge densities is estimated to exceed 500 N/m^2 providing a lift of 50 kg/m^2. This is a large force and it should be possible to measure this directly using a balance. This was done by attaching the substrate chip to a balance / micromanipulator arrangement (Figs. 8-1, 8-S1). This modified apparatus allows us to record force-distance curves.

Figure 8-3B shows the force-distance curves for SiO_2 substrates after contact with plasma activated PDMS at ~30% relative humidity. The curves were recorded by measuring the microbalance weight reduction as a function of separation. The left side of the graph plots the overall adhesive force after contact up to separation whereas the right side of the graph plots the attractive Coulomb force as the substrate re-approaches the previously contacted PDMS. The graph shows a phenomenological relationship between short and long-range forces. Such a phenomenological relationship has been observed before.[105] Specifically high levels of short-range force (adhesion) corresponds to larger long-range force, but the short-range force is much larger in magnitude. The link has not yet been explained. A possible explanation is that for an ionically bonded surface, delamination results in separation of ions. Not every ion is separated, and gas discharge always provides the upper limit to the level of remaining uncompensated ions and long range electrostatic force that can remain. A higher final concentration of uncompensated surface charge (and long range forces) would imply that it originated from a higher initial concentration of ionic bonds (and short range forces).

Surfaces treated to enhance the strength of the long range electrostatic attractive force are much harder to delaminate. The pH treatment resulted in an increase in both the short and long-range forces for SiO_2 (Fig. 8-3B, green triangles). The recorded long-range electrostatic force increased by a factor of 5 with a maximum value approaching 150 N/m^2, leading to an estimated field of (~4.1x10^6 V/m) using $E=\sigma/\varepsilon$. The value remains higher than the breakdown strength of air but is about a factor of 2 smaller than what we anticipated based on the charge measurement alone (Fig. 8-3A). Experimentally

it is a challenge to record the last data point at the smallest separation before the surfaces jump into conformal contact.

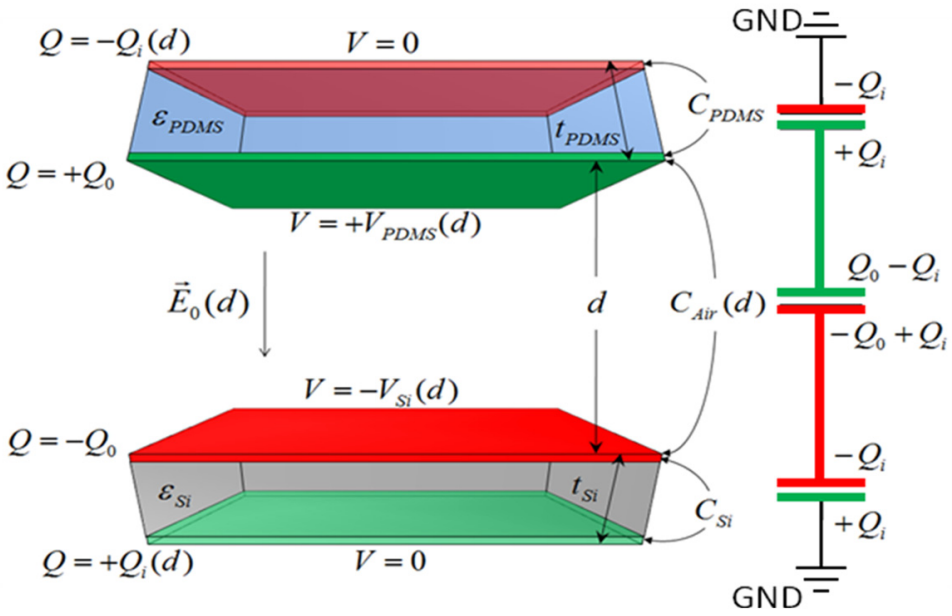

Figure 8-4. *Electrode arrangement and coupling considering stray capacitance. Q_0 and $-Q_0$ represents the respective charge on the insulating PDMS (top green) and SiO_2 (bottom red) surface after contact electrification. Q_0 is fixed and not a function of the distance. Image charges Q_i are drawn into the conductive mounting plates which alters the field distribution. The equivalent circuit model for the depicted capacitances is shown on the right. The total charge on the red and green plates remains Q_0. The value of Q_i depends on the separation d.*

The recorded long range electrostatic force in figure 8-3 is a function of the separation distance between the contacted surfaces which cannot be explained using a simple parallel plate model where the attractive force density is commonly calculated using $\boldsymbol{F/A = \sigma^2/2\varepsilon_0}$ which is independent of distance. Instead the recorded data fits a more accurate model that considers stray capacitances to nearby grounded plates which reduce the electric field in the air gap in between the charged layers as shown in **figure 8-4**. After contact electrification, image charges $\boldsymbol{Q_i(d)}$ are drawn from ground to flow to nearby metal plates. The amount of image charge $\boldsymbol{Q_i(d)}$ increased as the separation *d* increases. To understand the rebalancing of charges and fields it is important to consider

how the capacitance changes as the air gap increases. For example the capacitance across an increasingly large air gap drops while the coupling capacitances to the grounded metal plates remains unchanged. Utilizing the grounded metal plates as boundary condition with an electric potential of $V=0$ and applying Kirchhoff's Voltage Law yields a relationship for the respective voltages $V_{Air}=V_{PDMS}+V_{Si}$. Using $V_{Air}=(Q_0-Q_{i(d)})/C_{Air(d)}$, $V_{PDMS}=Q_{i(d)}/C_{PDMS}$, and $V_{Si}=Q_{i(d)}/C_{Si}$ the equation expands to $(Q_0-Q_{i(d)})/C_{Air(d)}= Q_{i(d)}/C_{PDMS}+ Q_{i(d)}/C_{Si}$ which yields the relationship for the image charges:

$$Q_{\mathrm{i}}(d)=\frac{Q_0}{1+C_{\mathrm{Air}}/C_{\mathrm{PDMS}}+C_{\mathrm{Air}}/C_{\mathrm{Si}}}=\frac{Q_0}{1+C_{\mathrm{Air}}/C_{\mathrm{Stray}}} \tag{8-1}$$

as well as the charges $Q_0-Q_{i(d)}$ which couple the PDMS surface with the SiO_2 surface as the distance is increased:

$$Q_0-Q_{\mathrm{i}}(d)=\frac{Q_0}{1+C_{Stray}d/(\varepsilon_0 A)} \tag{8-2}$$

The previously introduced equation $F/A = \sigma^2/2\varepsilon_0 = Q^2/(2\,\varepsilon_0\,A^2)$ can now be applied if we substitute Q with the relevant charge $Q_0-Q_{i(d)}$ which is the charge that is responsible for the electric field and force that couples the PDMS surface with the SiO_2 surface. The substitution delivers the force per unit area as a function of separation d:

$$\frac{F_{Air}}{A}=\frac{\sigma_0^2}{2\varepsilon_0}\frac{1}{(1+C_{Stray}d/(\varepsilon_0 A))^2} \tag{8-3}$$

Equation 8-3 provides an accurate model of the force versus distance curves. For very small distances d it approaches a constant value of $\sigma_0^2 / 2\varepsilon_0$ which represents the maximum force value that can be anticipated. At larger distances the force drops inversely proportional to the square of the distance. Equation 3 was used to fit the measured force-distance data (Fig. 8-3B, dashed lines) which provides values of the actual stray capacitance of our system. The model represented by equation 8-3 is in good agreement with the experimental data.

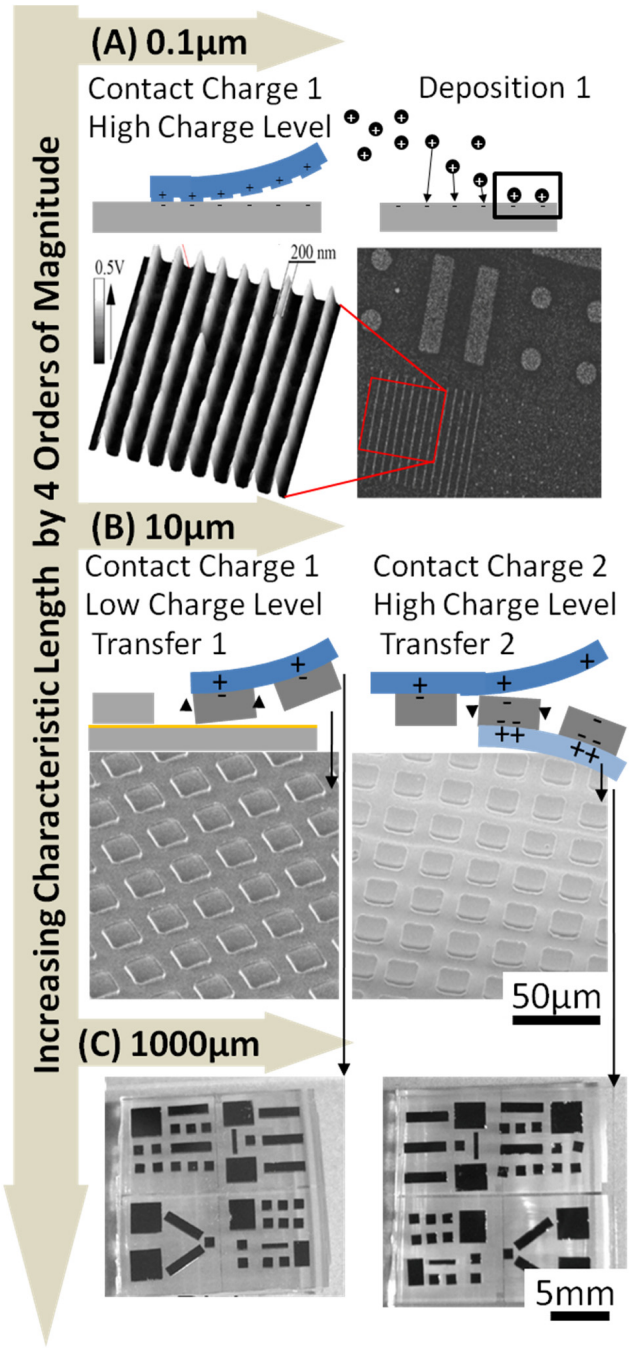

Figure 8-5. *Implications of forces originating from uncompensated surface charges on objects spanning 4 orders of magnitude in size. A) Charge pattern as recorded by KFM (left) which attracts 5-50 nm silver nanoparticles (right). (B,C) Two contact charging steps showing selective transfer of micrometer and millimeter sized silicon chips from an initial rigid substrate onto pH0 treated PDMS (using a low interfacial charge level) and finally to pH14 treated PDMS (using a high interfacial charge level).*

Figure 8-5 shows that nanocontact electrification can be used to produce laterally confined charge patterns which can attract nanoparticles and large components. To give a qualitative comparison to prior parallel charge patterning concepts,[12, 14, 15, 108] nanocontact electrification provides a higher charge density with values close to the breakdown limit. The process provides an equally high lateral resolution but eliminates the need for fragile metallization on PDMS stamps that was previously required to produce conformal electrical contacts to inject charge by applying an external voltage. As a direct result the areas are no longer limited to 1 cm^2; we have tested 100 cm^2 samples observing uniform patterns in the tested areas. Other differences are that the use of an external bias voltage and a conducting substrate underneath the electret are also no longer required. In terms of the degradation of the charging ability of the PDMS as a function of use, we found that plasma activated PDMS can be used multiple times before it needs reactivation; no measurable degradation was observed after 50 charging experiments. This observation can be explained if we compare a typical value of the recorded surface charge density with the intermolecular spacing of the reactive sites that are available; observed levels of charge of about 10 nC/cm^2 reflects about 1 elementary charge per 40 nm by 40 nm sized area. This is a large spacing from a molecular standpoint. For example, the area per silynol group is estimated to be 0.7 nm x 0.7 nm. This leads to an abundance of surface groups on the PDMS that can take part in the reaction and supports the observation that the PDMS can be used multiple times. The plasma activated PDMS, however, aged with time, losing most of the charging ability after 5 days. The aging can be linked to an earlier unrelated study[178] and involves the diffusion of oligomers over time from the bulk to the surface of the PDMS, returning it to its pre-treated state.

The reported process impacts areas from the nanoscopic up to the macroscopic range. Figure 8-5A shows that the produced patterns of charge (left) can be develop into patterns of printed nanoparticles (right). In the given example, 5-50 nm sized silver nanoparticles were deposited directly from the gas phase using a previously reported nanomaterial source.[14, 15] The strength of the effect is not limited to nanoscopic objects. Micro and millimeter sized objects can be transferred from one substrate to another by tailoring the electrostatic force of adhesion. For example, the adhesive forces exceeded the weight

(1.6g) of the 2 x 2 cm, 4 mm thick PDMS stamps used in the experiments. After contact and separation, the stamp can be picked up on re-approach without bringing it into conformal contact. Figures 8-5(B, C) show more practical examples in the area of flexible electronics that are selected based on the discussed force distance curves (Fig. 8-3B). Silicon components with a native oxide were picked up from a donor wafer using an initial piece of PDMS (pH0 treated, low interfacial charging) and subsequently transferred to another piece of PDMS (pH14 treated, high interfacial charging) that showed the strongest force of adhesion. The components ranged in size from 1-5 mm wide and 300 μm thick silicon blocks (Fig. 8-5B) to 20 x 20 μm Si chiplets that were 2 μm thick (Fig. 8-5C). The components were picked up and transferred over a 2 x 2 cm area with yields of 100% and 99% respectively.

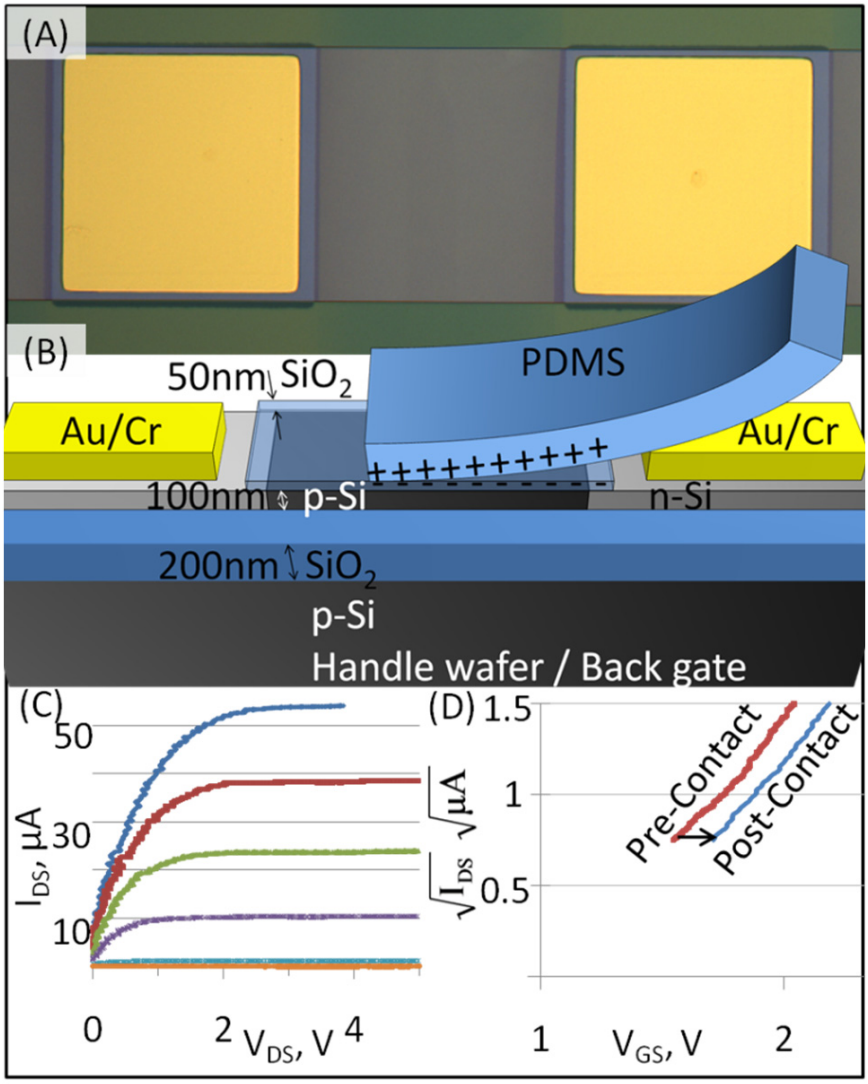

Figure 8-6. *Contact electrification impacting electrical performance of thin Si FETs. A) Top-down optical microscope image next to a B) cross-sectional schematic of device. C) I_{DS} vs. V_{DS} curves showing field effect sensitivity to the back gate. D) $\sqrt{I_{DS}}$ vs. V_{GS} plot showing the threshold voltage shift before and after contact and delamination.*

Figure 8-6 shows that contact electrification by touching electronic devices with PDMS will affect transport in nearby semiconducting device layers which can be directly witnessed in terms of transistor threshold voltage shifts. The optical microscope image (Fig. 8-6A) shows a thin silicon-on-insulator field effect transistor (FET) which was used as test structure. The device was fabricated using a commercially available silicon-on-insulator substrate were the thin 100nm silicon device layer was supported by 200nm of

buried silicon dioxide. Figure 6B shows a device schematic; full fabrication details are described in the methods section. The device layer of the FET was coated with SiO_2 or PMMA with respective negative and positive charging characteristics to observe if a contact with PDMS would alter the threshold voltage. The I_{DS} vs. V_{GS} transistor curves shown in Figure 6C were taken using the handle wafer as a back gate. We used the x-axis intercept of $\sqrt{I_{DS}}$ vs. V_{GS} line to evaluate the threshold voltage which retains accuracy even for added series resistances of SOI FETs.[168] For SiO_2 the threshold voltage applied to the back gate shifts to a higher voltage which implies the presence of negative surface charge on the SiO_2 surface. In other words the presents of negative surface charges need to be compensated by an extra positive gate voltage to turn ON the device. In the illustrated case (Fig. 8-6D) we recorded ΔV_{th} of 127mV for a d=50nm SiO_2 film which leads to a charge density of $\sigma = -\varepsilon(\Delta V_{th} / d) = -8.78\text{nC/cm}^2$ by modelling the surface potential as a floating body effect.[179] The sign and charge density agrees very well with figure 3A recorded values (a range of -7 to -9 nC/cm^2 was observed). For a 48nm PMMA film ΔV_{th} shifts negative by 60mV which means $+2.76\text{nC/cm}^2$ of surface charge. Again polarity and magnitude are in good agreement. For PDMS contact directly to a silicon n-FET with only its native oxide, the threshold voltage increased by 580mV.

8.3 Conclusion

In conclusion the cleavage of conformal contacts, which has become a common procedure in areas of soft-lithography and other soft-printing processes, typically leaves behind large amounts of surface charge as the surfaces are delaminated. While these surface charges remain undetected with most commonly applied spectroscopic measurement techniques including XPS and FTIR, direct evidence can be gained through Kelvin probe force microscopy and force distance curve measurements. The recorded charging levels can be very high and the upper levels seem to be self-limited by the dielectric breakdown strength of the air gap that forms as the materials are delaminated. The separated charges give rise to an electrostatic force of adhesion that can be detected over millimeter distances, exceeding 150 N/m^2 in some cases. The corresponding force distance curves depict a phenomenological relationship between short and long-range

attractive forces. The presented explanation suggests a two-step process whereby the formation and delamination of interfaces bonded by ions precedes contact electrification and the generation of long-range electrostatic forces. SiO_2, PS, PAA, PMMA, and SU-8 are all commonly used in the processing of semiconductor devices. We therefore expect that our findings will impact areas which go beyond the demonstrated charge directed assembly and transfer applications. Charge printing is likely possible for other semiconductor substrates with a thin surface oxide including native oxides. For example, we found that the native oxide on Si is still prone to charging despite the fact that it is much thinner than the 160 nm thick thermal silicon oxide that was used in this study. The results reported here are especially meaningful in the context of soft lithography where PDMS contact to devices with thin oxides may result in altered threshold voltages. Specifically the emerging field of printable and flexible electronics could be impacted, where contact printing methods and delamination of interfaces are used to print and transfer materials. We anticipate that the presence of high levels of uncompensated charges may alter the functionality of various electronic devices including FETs unless models take these extra gate charges into account. The additional challenges are particularly relevant in the context of flexible electronics where thin semiconductors, polymer insulators, and conformal contacts are widely employed.

8.4 Experimental Methods

PDMS fabrication and surface treatments: PDMS fabrication for this study was unaltered from the commonly accepted technique. Specifically we mixed 30g elastomer (Sylgard 184) and 3g curing agent (also Sylgard 184) together for about 2 minutes at room temperature. Mixing caused gas bubbles to form, so uncured PDMS was degassed in a vacuum chamber at ~30 Torr for 20 minutes. The uncured PDMS was poured onto silanized silicon, then degassed again for 1 hour at ~20 Torr. (The silicon may also be patterned with S1813 photoresist prior to treatment with octadecyltrichlorosilane if features were desired for the finished PDMS.) The degassed PDMS is cured in a convection oven at 60^{o}C for 12 hours. The cured PDMS was inserted into a commercially available plasma cleaner (SPI, model Plasma Prep II) for oxygen plasma treatment. The

system was purged with 99.99% oxygen, then the 80-100W 13.56MHz RF plasma was operated at 10 Torr for 40 seconds.

For pH treatment, the cured PDMS was immersed into a high molarity acid or base bath. The bath was contained in a high density polymer (Nalgene) to minimize solvent-container reactions and the bath was covered to minimize evaporation. We used 1M HCl as a strong acid or 1M NaOH as a strong base. Direct measurement of the solvent pH was performed with pH indicator paper which showed pH <1 and pH >13 for HCl and NaOH respectively. Brief exposures of an electronic pH probe to the highly acidic and basic solutions support these pH values as well. For ease of reference we named the solutions "pH0" or "pH14." Cured PDMS pieces were soaked in one of these solutions for one hour before use.

Electrometer charge measurement: When determining the quantity of transferred charge we removed the PDMS a distance of at least 10cm to ensure that printed charges were electrostatically coupled only to the grounded metal mounting plate which was in turn connected to the electrometer. The recorded level of uncompensated charge on the sample using the electrometer is fairly constant and only drops slightly over time at a rate which was less than 50pC per minute. The drop can be explained by the attraction of charged species from the environment. The electrometer measurements were conducted in a Faraday cage (shown in supplemental figure 8-S1) and the accuracy of the properly shielded instruments exceeds 1pC (Keithley, Model 6517). Most substrates charged up by at least 1nC which is well above the noise level of the instrument. Variations in recorded values between experiments, however, were found to be larger than the noise level and ranged between 20-300 pC. Variations in the recorded values repeating the same experiments cannot be considered as a measurement error and are believed to be associated primarily to partial discharge by attraction of gas ions from the gas environment, handling, time and variations in the PDMS thickness which alters the coupling to the grounded metal plates that act as faraday cups in the illustrated case. A fully automated system that takes the human interaction out of the loop and places the system inside a sealed environment to minimize airflow would allow a more accurate

measurement. Such an improvement is not going to change the general trends found in this study.

Delamination procedure: Separation of the PDMS was performed by pulling the PDMS stamp upwards in a plane-parallel fashion. This leads to fast moving delaminating fronts which break the conformal contact. Complete separation of the interface is estimated to be in the range of 50-500ms. The plane parallel separation occurs faster than conventional peeling and was chosen to minimize the risk of a partial discharge or arcing across the forming gap due to the high electric field that will be present at low separation distances. We have not observed the visual effects of arcing. We acknowledge, however, that there might be a dependency between the level of the recorded charge and the peel rate which has not yet been investigated in detail. An approach to determine this relationship would be to use rolling cylinders with different roll speeds. Although viscoelastic effects are well known to play a role in the physical adhesion of PDMS to surfaces, we did not observe that the peel rate has a strong affect on the level of charge transfer. Instead the properties of PDMS and the material being contacted played much stronger roles as reported here. Moreover it would be interesting to control the environment beyond the humidity and for example perform measurements under vacuum or different gas environments to test if higher levels of charge are possible. This would provide further insights into the process which limits the amount of charge across the interface. Extending the present study in such a manner, however, would require the installation of a completely different apparatus.

Si component fabrication: The fabrication of the Si components involved electron-beam deposition of Si onto Au-coated pillars of SU-8. Specifically we first fabricated the SU-8 pillars on a <100> p-type 4" Si carrier substrate. The carrier substrate was cleaned for 15 minutes in a 120^{o}C Piranha bath solution composed of 3 parts H_2SO_4 (99%) and 1 part H_2O_2 (30% in H_2O). The cleaned substrate was spincoated with Omnicoat (an SU-8 adhesion promoter) which a spinner speed of 2500RPM for 30s. The adhesion layer was baked on at 200^{o}C for 1 min. SU-8 was spincoated on top of the Omnicoat at 2500RPM for 30s then softbaked at 65^{o}C for 1min and then 95^{o}C for 2min. The SU-8 was soft contact exposed for 11s under about 12mW/cm^2 i-line illumination. The SU-8 was given

a post exposure bake identical to the softbake and then developed for 4min in PGMEA (propylene glycol monomethyl ether acetate). Excess Omnicoat was removed by exposure to 100W 100mTorr oxygen plasma for 40s. Using an electron-beam evaporator, 20nm Cr and then 200nm Au were deposited on the SU-8 pillars. Then 2μm of Si were deposited by e-beam evaporation on top of the Au coated SU-8.

The chemical bond of Si to the Au beneath is well-known to be weak. Increasing the chemical adhesion of materials to Au typically requires an additional adhesion layer such as the Cr used on the SU-8 pillars. In absence of any adhesion layer beneath the Si components, the Si components are easily delaminated from the Au and picked up by the weak electrostatic charge on the pH0 treated PDMS. Following Si component pickup by PDMS, an optical microscope confirmed that the gold layer remained on the SU-8 pillars. The components then were transferred to a second piece of PDMS which was treated with pH14.

Thin SOI MOSFET fabrication: Fabricating the charge-sensitive thin-SOI MOSFETs involved n-well doping, mesa etching, contact deposition, annealing, and insulator deposition. Each step used a pattern and etch-back process to avoid any debris that may be caused by liftoff processes. Beginning with 150mm diameter p-type Si on insulator wafers (SOITEC, inc.) with a 100nm Si device layer on a 200nm buried oxide, we deposited 300nm SiO_2 by PECVD at 340°C. To define the dopant mask S1805 photoresist was photolithographically patterned then given a 30s oxygen plasma descum, and the underlying SiO_2 was etched in 10:1 buffered oxide etch (a mix of HF and NH_4F in H_2O) for 150s. The photoresist was removed by rinsing with acetone, methanol, and isopropyl alcohol. Phosphorus containing n-type spin-on dopant was spun on the wafer and then driven in by rapid thermal annealing at 900°C for 10s under 6sLpm flow of 10% oxygen in nitrogen. The oxidized spin-on dopant was stripped in 49% HF for 120s. The sample was coated with 50nm SiO_2 by PECVD at 340°C to prevent metal from contacting p-Si, then windows to the n-wells were opened in the SiO_2 by photolithography, 30s oxygen plasma descum, and etching 30s in 10:1 BOE. Photolithography and oxygen descum was used to define ribbons of p-n-p silicon then 10:1 BOE removed the oxide, a 30s 20W 40mTorr $SF_6/Ar/O_2$ plasma etch removed

silicon down to the buried oxide, and the photoresist was removed. Metal contacts were deposited by DC sputtering using a quartz crystal monitor to measure the film thicknesses. Both top(source/drain) and back(gate) contacts were 150nm Au with a 5nm Cr adhesion layer. The contacts were patterned by photolithography, oxygen plasma descum, etching 25min in 10:1 DI H_2O:GE-6 gold etchant, and a 60s dip in 4:1 DI H_2O:CR-12S chrome etchant. The contacts were annealed by RTA at 400°C for 20s in 8sLpm forming gas (5%H_2 / 95%N_2). For the PMMA coated devices, the top SiO_2 was removed by etching in 10:1 BOE then 495K molecular weight PMMA diluted in anisole (roughly 1.5% mixture by weight) was spin-coated at 3000 rpm for 30s and softbaked at 180°C for 1 min. SiO_2 and PMMA thicknesses were monitored during processing by ellipsometry.

The mobility of these devices was estimated using a linear fit to $\sqrt{I_{DS}}$ vs. V_{GS} (Fig. 5D) for the SiO_2-covered case, $\mu_{FET} = 2/C_{BOX} * (\partial\sqrt{I_{DS}} / \partial V_{GS})^2 = 307 cm^2V^{-1}s^{-1}$. For the PMMA-covered case μ_{FET} after contact was found to be $125 cm^2V^{-1}s^{-1}$. We expect the <1 order of magnitude difference in channel mobility is likely due to local chemical reactions at the p-Si/dielectric interface since the PMMA was spin-coated and SiO_2 was deposited by PECVD. An increased number of ionized traps in the PMMA case would explain the lower mobility.

8.5 Supplemental Information

For the arrangement shown in Figure 8-S1, electrometers record the initial charge on the substrate and the stamp as well as the charge transfer after contact. The attractive force between the charged surfaces is recorded using a microbalance. The microbalance records the weight reduction of the stamp due to the attractive pull as the surfaces are separated and then slowly reapproached. A micromanipulator was used to adjust the separation with ~5 μm accuracy and to reduce angular mismatch, azimuth and zenith to be < 0.5^{o} prior to contact. In addition, the setup was placed inside a Faraday cage to increase accuracy of charge measurements.

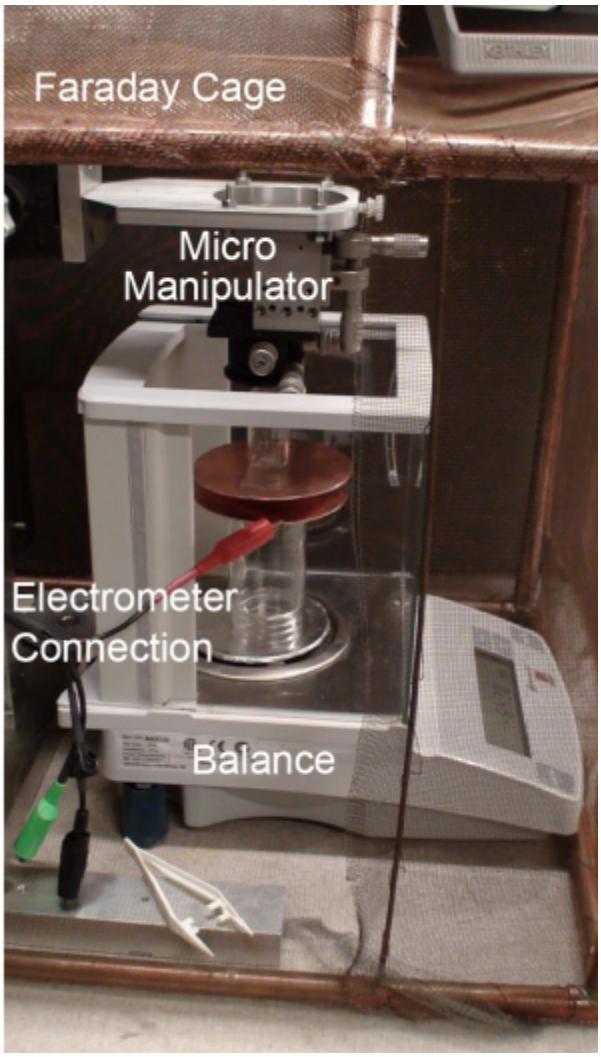

Figure 8-S1. *Force-Distance experimental setup.*

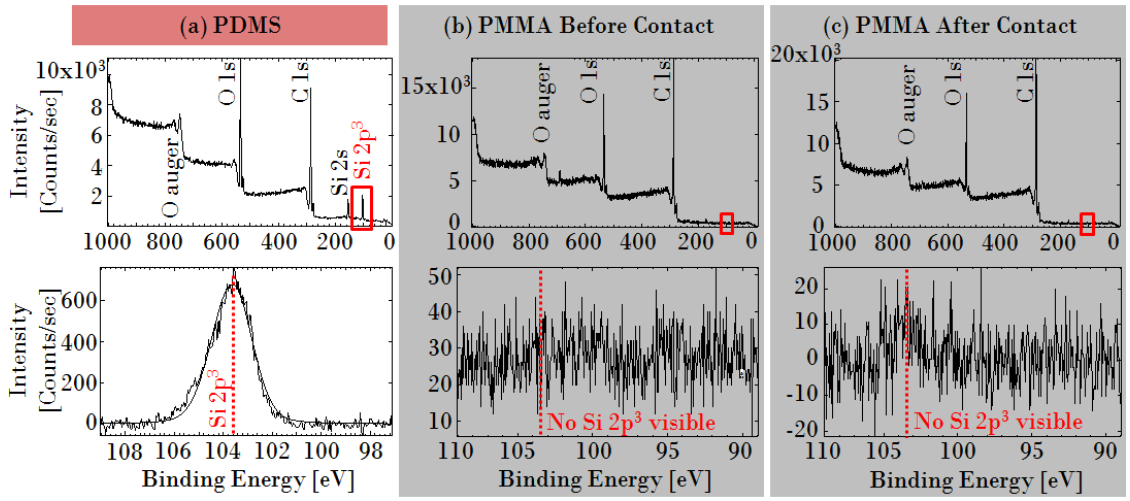

Figure 8-S2. *XPS study of material transfer from PDMS (a) to PMMA (b,c) by contact. Carbon and oxygen peaks are visible in each case, but only PDMS showed silicon peaks below 200eV. (Top row) The overall traces were narrowed (red boxes, top row) to determine peaks in the appropriate range (bottom row) for the binding energy range for Si. The silicon content of PDMS $[C_2H_6OSi]_n$ is measurable as a $2p^3$ peak at 103.4eV (red dotted line, bottom row). The plots show the lack of Si content on PMMA (b) before and (c) after contact with PDMS so it is concluded that no PDMS material transferred to the PMMA.*

The XPS studies of PDMS material transfer to PMMA by contact were performed by tracking Si content. Figure 8-S2 depicts XPS data showing Si content on (a) the PDMS surface with greatest intensity at 103.4eV which corresponds to the Si $2p^3$ peak. Since PMMA (chemical formula $[C_5H_8O_2]_n$) contains no Si and PDMS (chemical formula $[C_2H_6OSi]_n$) does contain Si it is possible to use XPS to track material transfer. As a control sample Si was not detected (b) on the PMMA surface before contact. Following contact with oxygen plasma treated PDMS (c) the surface still did not show any Si-related peaks with the conclusion that no PDMS material transferred to the PMMA.

As shown in Figure 8-S3 (top row) the AFM traces (a) for PMMA contacted by PDMS show no topography which supports the lack of material transfer by contact even with levels of transferred charge near +1V as measured by KFM (b). For the case of SiO_2 we observed material transfer to depend strongly on plasma parameters such that exposure to O_2 and N_2 containing air plasma for 1min or less reduced material transfer below AFM resolution limits as indicated in the figure 8-S3 (bottom row). We found that higher plasma O_2 content and longer treatment times resulted in increased PDMS material transfer to the SiO_2 such that the amount of material was visible in AFM scans. These

structures were not always charged and the PDMS stamps could not be used repeatedly. Best charging results in terms of repeatability and amount of charge transferred were achieved using a 10 Torr air based 20% oxygen plasma treatment (SPI Plasma Prep II) for 1 minute which allowed clean delamination and uniform charging as shown in the figure.

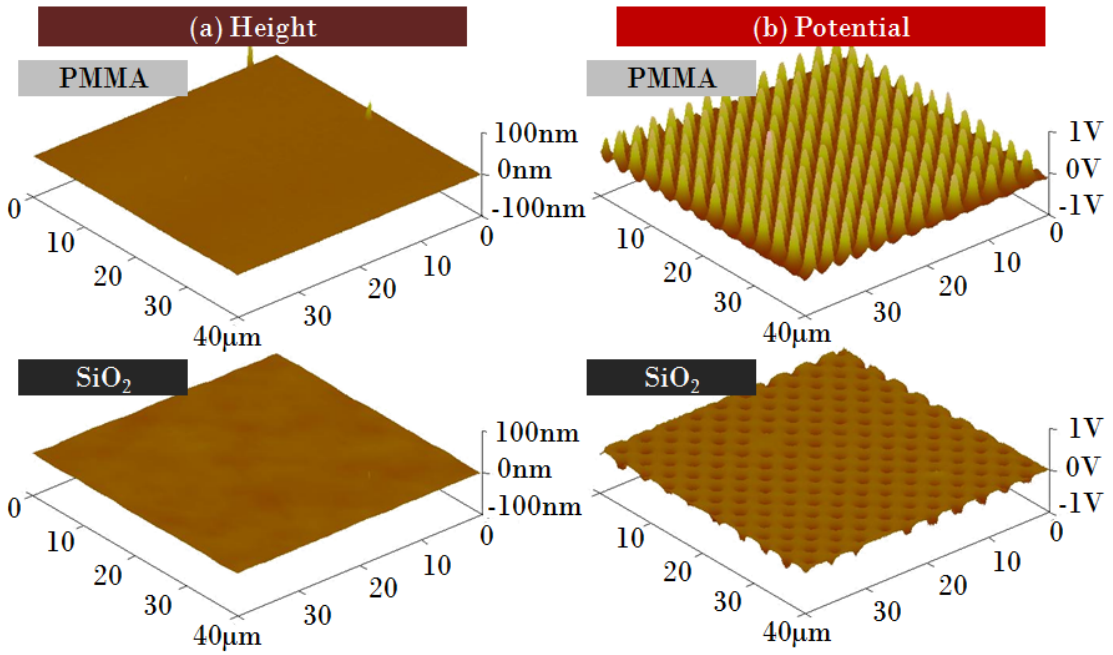

Figure 8-S3. *(a) AFM topography data with (b) corresponding KFM charge data for PMMA (top) and SiO_2 (bottom) after contact with PDMS. Lack of topography in both cases indicates minimal if any material transfer occurred during contact while the charge patterns are well resolved and opposite in polarity.*

Chapter IX

Conclusion

In summary, the reported ZnO nucleation and growth process provides a new route towards the production of ZnO micro and nanostructures at known locations (0.7% STD) with well defined dimensions (<1% STD). The process produces high quality ZnO where deep-level radiative defects are eliminated. In addition to the demonstrated micro-LEDs and micro-photovoltaic cells we anticipate that these two features are attractive for a number of other applications that aim at integrating ZnO based devices such ultraviolet LEDs[73-75], laser cavities[121], waveguides[54, 110-112], high gain photodetectors[116], photovoltaic cells[113-115], sensors, piezoelectric actuators[120] or micro-power generators[119] at exact known locations on a surface. Control over location lead to the hexagonal light emission (Fig. 4-2B) and can ultimately be used to study coupling of light and lasing. It supports the ability to individually contact single ZnO crystals and learn how light propagates form one isolated domain to another. Moreover, it was possible to transfer single crystal domains from one substrate to another though interfacial delamination which finds applications in the field of flexible transparent electronics.

Comparable to liquid phase electrodeposition, the reported gas phase analogue can deposit material into addressable areas forming vias, interconnects, or patterned multimaterial films in a programmable fashion. The process was tested using a limited set of technologically relevant functional materials including Au, Si, Ge, TiO_2, and ZnO at sizes of 20nm and below as confirmed by TEM, SAED, EDX, and XRD. We anticipate that the process can be extended to other materials and gas phase systems with some alterations. The uniformity on a macroscale is presently limited by diffusion since we use a single point source fixed in space. Scaling to larger sample areas would require the use of either multiple sources or translational motion analogous to what has been used in other gas phase deposition systems. The ability to maintain uniformity when developing arbitrary patterns on a nanoscale requires a sufficiently small Debye length which in turn favors higher pressure aerosols to provide a high concentration of charged particles/ions

and deposition rate. The estimated values are sufficient to support selected area programmable deposition of a variety of different patterns including text, connected and disconnected structures. Operating a system at atmospheric pressure has the advantage of simplicity since neither vacuum pumps nor high pressure enclosures are required. Pressurized systems, however, would likely further increase the area selective deposition rate beyond the current 100 nm/min value. The current area selective rate is in between the 10 nm/min rate of non-selective vacuum deposition systems and typical 1 μm/min rate of area-selective electroplating methods. Variations in the film thickness, extension to large area deposition using multiple spatially separated discharge regions, passivation of surface and interface states are important aspects that will require further research and new and improved designs.

A potential future application of the gas phase electrodeposition technique can be found in the field of printable electronics. It contrasts the use of solution processable electronic inks and inkjet type printing concepts to deposit nanomaterials. Current inkjet based deposition systems have low resolution and throughput. The inks require surface functionalization to stabilize the particles which often interferes with the desired electronic properties. Alternatively the discussed *in-situ* gas phase synthesis and deposition system offers a more parallel route to the formation, deposition and integration of higher performance materials than liquid phase concepts. High temperature processes can be used to produce the materials that can then be deposited onto low temperature substrates eliminating any extra processing steps or a transition into the liquid phase. As such the present technique is highly parallel and does not require the use and alignment of scanning nozzles or the formulation of stable liquid particle suspensions. These advantages come at the cost of needing pre-patterned substrates to direct the deposition.

We also reported that the cleavage of conformal contacts, which has become a common procedure in areas of soft-lithography and other soft-printing processes, typically leaves behind large amounts of surface charge as the surfaces are delaminated. While these surface charges remain undetected with most commonly applied spectroscopic measurement techniques including XPS and FTIR, direct evidence can be gained through Kelvin probe force microscopy and force distance curve measurements. The recorded charging levels can be very high and the upper levels seem to be self-

limited by the dielectric breakdown strength of the air gap that forms as the materials are delaminated. The separated charges give rise to an electrostatic force of adhesion that can be detected over millimeter distances, exceeding 150 N/m^2 in some cases. The corresponding force distance curves depict a phenomenological relationship between short and long-range attractive forces. The presented explanation suggests a two-step process whereby the formation and delamination of interfaces bonded by ions precedes contact electrification and the generation of long-range electrostatic forces. SiO_2, PS, PAA, PMMA, and SU-8 are all commonly used in the processing of semiconductor devices. We therefore expect that our findings will impact areas which go beyond the demonstrated charge directed assembly and transfer applications. Charge printing is likely possible for other semiconductor substrates with a thin surface oxide including native oxides. For example, we found that the native oxide on Si is still prone to charging despite the fact that it is much thinner than the 160 nm thick thermal silicon oxide that was used in this study. The results reported here are especially meaningful in the context of soft lithography where PDMS contact to devices with thin oxides may result in altered threshold voltages. Specifically the emerging field of printable and flexible electronics could be impacted, where contact printing methods and delamination of interfaces are used to print and transfer materials. We anticipate that the presence of high levels of uncompensated charges may alter the functionality of various electronic devices including FETs unless models take these extra gate charges into account. The additional challenges are particularly relevant in the context of flexible electronics where thin semiconductors, polymer insulators, and conformal contacts are widely employed.

Bibliography

1. Piner, R.D., et al., *\"Dip-pen\" nanolithography.* Science (Washington, D. C.), 1999. **283**(5402): p. 661-663.
2. Bullen, D., et al., *Parallel dip-pen nanolithography with arrays of individually addressable cantilevers.* Applied Physics Letters, 2004. **84**(5): p. 789-791.
3. Baur, C., et al., *Nanoparticle manipulation by mechanical pushing: underlying phenomena and real-time monitoring.* Nanotechnology, 1998. **9**(4): p. 360-364.
4. de Gans, B.-J., P.C. Duineveld, and U.S. Schubert, *Inkjet printing of polymers: State of the art and future developments.* Advanced Materials (Weinheim, Germany), 2004. **16**(3): p. 203-213.
5. Magdassi, S. and M. Ben Moshe, *Patterning of Organic Nanoparticles by Ink-jet Printing of Microemulsions.* Langmuir, 2003. **19**(3): p. 939-942.
6. Loo, Y.-L., et al., *Additive, nanoscale patterning of metal films with a stamp and a surface chemistry mediated transfer process: Applications in plastic electronics.* Applied Physics Letters, 2002. **81**(3): p. 562-564.
7. Jeon, S., et al., *Three-dimensional nanofabrication with rubber stamps and conformable photomasks.* Advanced Materials (Weinheim, Germany), 2004. **16**(15): p. 1369-1373.
8. Wright, W.M.D. and D.G. Chetwynd, *Can charge writing aid nanotechnological manipulation.* Nanotechnology, 1998. **9**(2): p. 133-142.
9. Niemeyer, C.M., et al., *Site-selective immobilization of gold nanoparticles functionalized with DNA oligomers.* Colloid & Polymer Science, 2001. **279**(1): p. 68-72.
10. Rao, S.G., et al., *Nanotube electronics: large-scale assembly of carbon nanotubes.* Nature (London, United Kingdom), 2003. **425**(6953): p. 36-37.
11. Yellen, B.B. and G. Friedman, *Programmable assembly of heterogeneous colloidal particle arrays.* Advanced Materials, 2004. **16**(2): p. 111-115.
12. Jacobs, H.O. and G.M. Whitesides, *Submicrometer patterning of charge in thin-film electrets.* Science, 2001. **291**(5509): p. 1763-1766.
13. Jacobs, H.O., S.A. Campbell, and M.G. Steward, *Approaching NanoXerography: The use of Electrostatic Forces to Position Nanoparticles with 100 Nanometer Scale Resolution.* Advanced Materials, 2002. **14**(21): p. 1553-1557.
14. Barry, C.R., et al., *Printing nanoparticles from the liquid and gas phases using nanoxerography.* Nanotechnology, 2003. **14**(10): p. 1057-1063.
15. Barry, C.R., et al., *Printing nanoparticle building blocks from the gas-phase using nanoxerography.* Appl. Phys. Lett., 2003. **83**: p. 5527.
16. Mesquida, P. and A. Stemmer, *Attaching silica nanoparticles from suspension onto surface charge patterns generated by a conductive atomic force microscope tip.* Advanced Materials (Weinheim, Germany), 2001. **13**(18): p. 1395-1398.
17. Naujoks, N. and A. Stemmer, *Micro- and nanoxerography in liquids - controlling pattern definition.* Microelectronic Engineering, 2005. **78-79**: p. 331-337.
18. Krinke, T.J., et al., *Positioning of nanometer-sized particles on flat surfaces by direct deposition from the gas phase.* Applied Physics Letters, 2001. **78**(23): p. 3708-3710.

19. Chothia, C. and J. Janin, *Principles of protein-protein recognition.* Nature, 1975. **256**(5520): p. 705-8.
20. Dabrowski, M.J., et al., *Strategies for protein-based nanofabrication: Ni2+-NTA as a chemical mask to control biologically imposed symmetry.* Chemistry & Biology, 1998. **5**(12): p. 689-697.
21. Braun, E., et al., *Dna-templated assembly and electrode attachment of a conducting silver wire.* Nature, 1998. **391**(6669): p. 775-778.
22. Huang, Y., et al., *Dielectrophoretic cell separation and gene expression profiling on microelectronic chip arrays.* Analytical Chemistry, 2002. **74**(14): p. 3362-3371.
23. Winningham, T.A., et al., *Formation of ordered nanocluster arrays by self-assembly on nanopatterned Si(100) surfaces.* Surface Science, 1998. **406**(1-3): p. 221-228.
24. Cui, Y., et al., *Integration of Colloidal Nanocrystals into Lithographically Patterned Devices.* Nano Letters, 2004. **4**(6): p. 1093-1098.
25. Li, D., et al., *Collecting Electrospun Nanofibers with Patterned Electrodes.* Nano Letters: p. ACS ASAP.
26. Mueller, T., et al., *High-frequency electric-field trap for micron and submicron particles.* Nuovo Cimento della Societa Italiana di Fisica, D: Condensed Matter, Atomic, Molecular and Chemical Physics, Fluids, Plasmas, Biophysics, 1995. **17D**(4): p. 425-32.
27. Fudouzi, H., M. Kobayashi, and N. Shinya, *Assembling 100 nm scale particles by an electrostatic potential field.* Journal of Nanoparticle Research, 2001. **3**(2-3): p. 193-200.
28. Velev, O.D., B.G. Prevo, and K.H. Bhatt, *On-chip manipulation of free droplets.* Nature (London, United Kingdom), 2003. **426**(6966): p. 515-516.
29. Littau, K.A., et al., *A Luminescent Silicon Nanocrystal Colloid via a High-Temperature Aerosol Reaction.* J. Phys. Chem., 1993. **97**: p. 1224-1230.
30. Ostraat, M.L., et al., *Synthesis and characterization of aerosol silicon nanocrystal nonvolatile floating-gate memory devices.* Applied Physics Letters, 2001. **79**(3): p. 433-435.
31. Ostraat, M.L., et al., *Ultraclean two-stage aerosol reactor for production of oxide-passivated silicon nanoparticles for novel memory devices.* Journal of the Electrochemical Society, 2001. **148**(5): p. G265-G270.
32. Onischuk, A.A., et al., *Aerosol formation under heterogeneous/homogeneous thermal decomposition of silane: experiment and numerical modeling.* Journal of Aerosol Science, 2000. **31**(8): p. 879-906.
33. Batson, P.E. and J.R. Heath, *Electron energy loss spectroscopy of single silicon nanocrystals: the conduction band.* Physical Review Letters, 1993. **71**(6): p. 911-14.
34. Huisken, F., et al., *Nanostructuration with visible-light-emitting silicon nanocrystals.* New Journal of Physics, 2003. **5**: p. 1-10, Paper No. 10.
35. Ledoux, G., et al., *Photoluminescence of size-separated silicon nanocrystals: Confirmation of quantum confinement.* Applied Physics Letters, 2002. **80**(25): p. 4834-4836.

36. Ledoux, G., et al., *Photoluminescence properties of silicon nanocrystals as a function of their size.* Physical Review B, 2000. **62**(23): p. 942-951.
37. Ehbrecht, M. and F. Huisken, *Gas-phase characterization of silicon nanoclusters produced by laser pyrolysis of silane.* Physical Review B: Condensed Matter and Materials Physics, 1999. **59**(4): p. 2975-2985.
38. Li, X., et al., *Process for Preparing Macroscopic Quantities of Brightly Photoluminescent Silicon Nanoparticles with Emission Spanning the Visible Spectrum.* Langmuir, 2003. **19**(20): p. 8490-8496.
39. Shen, Z., U. Kortshagen, and S.A. Campbell, *Electrical characterization of amorphous silicon nanoparticles.* Journal of Applied Physics, 2004. **96**(4): p. 2204-2209.
40. Shen, Z. and U. Kortshagen, *Experimental study of the influence of nanoparticle generation on the electrical characteristics of argon-silane capacitive radio-frequency plasmas.* Journal of Vacuum Science & Technology, A: Vacuum, Surfaces, and Films, 2002. **20**(1): p. 153-159.
41. Stoykov, S., C. Eggs, and U. Kortshagen, *Plasma chemistry and growth of nanosized particles in a C2H2 RF discharge.* Journal of Physics D-Applied Physics, 2001. **34**(14): p. 2160-2173.
42. Bhandarkar, U.V., et al., *Modelling of particle nucleation in low-pressure silane plasma.* J. Phys. D: Appl. Phys., 2000. **33**: p. 2731-2746.
43. Kortshagen, U. and U. Bhandarkar, *Modeling of particulate coagulation in low pressure plasmas.* Physical Review E. Statistical Physics, Plasmas, Fluids, & Related Interdisciplinary Topics, 1999. **60**(1): p. 887-98.
44. Kortshagen, U.R., et al., *Generation and growth of nanoparticles in low-pressure plasmas.* Pure & Applied Chemistry, 1999. **71**(10): p. 1871-1877.
45. Dong, Y., et al., *The Generation of Free-Standing Single Crystal Silicon Nanoparticles.* J. Vac. Sci. and Technol. B, 2004. **44**(4): p. 1923-30.
46. Bapat, A., et al., *Plasma synthesis of single-crystal silicon nanoparticles for novel electronic device applications.* Plasma Physics and Controlled Fusion, 2004. **46**(12B): p. B97-B109.
47. Campbell, S.A., et al., *The Production and Electrical Characterization of Free Standing Cubic Single Crystal Silicon Nanoparticles.* Journal of Materials, 2004.
48. Bhandarkar, U., U. Kortshagen, and S.L. Girshick, *Gas temperature effects on particle generation in an argon-silane low-pressure plasma.* J. Phys. D: Appl. Phys., 2003.
49. Bapat, A., et al., *Synthesis of highly oriented, single-crystal silicon nanoparticles in a low-pressure, inductively coupled plasma.* J. Appl. Phys., 2003. **94**(3): p. 1969-1974.
50. Shen, Z., et al., *Formation of highly uniform silicon nanoparticles in high density silane plasmas.* J. Appl. Phys., 2003. **94**(4): p. 2277-2283.
51. Bhandarkar, U., U. Kortshagen, and S. Girshick, *Gas Temperature and Carrier Gas effects on nanoparticle formation in silane plasmas.* Proceedings of 55th Annual Gaseous Electronics Conference, Minneapolis, MN, 2002.
52. Wang, Z.L. and Z. Pan, *Nanobelts of semiconductive oxides: a structurally and morphologically controlled nanomaterials system.* International Journal of Nanoscience, 2002. **1**(1): p. 41-51.

53. Wu, Y. and P. Yang, *Germanium nanowire growth via simple vapor transport.* Chemistry of Materials, 2000. **12**(3): p. 605-607.
54. Yang, P., et al., *Controlled growth of ZnO nanowires and their optical properties.* Advanced Functional Materials, 2002. **12**(5): p. 323-331.
55. Greene, L.E., et al., *Low-temperature wafer-scale production of ZnO nanowire arrays.* Angewandte Chemie, International Edition, 2003. **42**(26): p. 3031-3034.
56. Cozzoli, P.D., A. Kornowski, and H. Weller, *Low-Temperature Synthesis of Soluble and Processable Organic-Capped Anatase TiO2 Nanorods.* Journal of the American Chemical Society, 2003. **125**(47): p. 14539-14548.
57. Devoret, M.H. and R.J. Schoelkopf, *Amplifying quantum signals with the single-electron transistor.* Nature, 2000. **406**(6799): p. 1039-1046.
58. Junno, T., et al., *Single-electron devices via controlled assembly of designed nanoparticles.* Microelectronic Engineering, 1999. **47**(1-4): p. 179-183.
59. Schoelkopf, R.J., et al., *The radio-frequency single-electron transistor (rf-set) - a fast and ultrasensitive electrometer.* Science, 1998. **280**(5367): p. 1238-1242.
60. Ding, Y., et al., *Field-Effect Transistor Built with a Single Crystal Si Nanoparticle.* Proceedings of 2005 NSF DMII Grantees Conference, Scottsdale, Arizona,January 3-6, 2005.
61. Menard, E., et al., *A printable form of silicon for high performance thin-film transistors on plastic substrates.* Applied Physics Letters, 2004. **84**(26): p. 5398-5400.
62. Bjork, M.T., et al., *One-dimensional heterostructures in semiconductor nanowhiskers.* Applied Physics Letters, 2002. **80**(6): p. 1058-1060.
63. Fafard, S., et al., *Red-emitting semiconductor quantum dot lasers.* Science, 1996. **274**(5291): p. 1350-1353.
64. Faist, J., et al., *Quantum cascade laser.* Science, 1994. **264**(5158): p. 553-556.
65. Xia, Y.N., B. Gates, and Z.Y. Li, *Self-assembly approaches to three-dimensional photonic crystals.* Advanced Materials, 2001. **13**(6): p. 409-413.
66. Phely-Bobin, T.S., et al., *Preferential self-assembly of surface-modified Si/SiOx nanoparticles on UV/ozone micropatterned poly(dimethylsiloxane) films.* Advanced Materials, 2000. **12**(17): p. 1257-+.
67. Norris, D.J. and Y.A. Vlasov, *Chemical approaches to three-dimensional semiconductor photonic crystals.* Advanced Materials, 2001. **13**(6): p. 371-376.
68. Yang, P.D., et al., *Patterning porous oxides within microchannel networks.* Advanced Materials, 2001. **13**(6): p. 427-431.
69. Petit, C., A. Taleb, and M.P. Pileni, *Self-organization of magnetic nanosized cobalt particles.* Advanced Materials, 1998. **10**(3): p. 259 ff.
70. Yang , P., *Wires on Water.* Nature, 2003. **425**: p. 243-244.
71. Li, D., Y. Wang, and Y. Xia, *Electrospinning of Polymeric and Ceramic Nanofibers as Uniaxially Aligned Arrays.* Nano Letters, 2003. **3**(8): p. 1167-1171.
72. Duan, X., et al., *Indium phosphide nanowires as building blocks for nanoscale electronic and optoelectronic devices.* Nature (London), 2001. **409**(6816): p. 66-69.
73. Vispute, R.D., et al., *Heteroepitaxy of ZnO on GaN and its implications for fabrication of hybrid optoelectronic devices.* Applied Physics Letters, 1998. **73**(3): p. 348-350.

74. Wang, X., et al. *ZnO Nanowire/p-GaN Heterojunction LEDs*. in *Mater. Res. Soc. Symp. Proc.* 2007. Warrendale, PA.
75. Wang, X., J. Cole, and H.O. Jacobs. *Electroluminescence of ZnO Nanowire/p-GaN Heterojunction Light Emitting Diodes*. in *Proc. 2007 NSTI Nanotechnology Conference*. 2007. Santa Clara, CA.
76. Alivov, Y.I., et al., *Fabrication and characterization of n-ZnO/p-AlGaN heterojunction light-emitting diodes on 6H-SiC substrates.* Applied Physics Letters, 2003. **83**(23): p. 4719-4721.
77. Alivov, Y.I., et al., *Observation of 430 nm electroluminescence from ZnO/GaN heterojunction light-emitting diodes.* Applied Physics Letters, 2003. **83**(14): p. 2943-2945.
78. Osinsky, A., et al., *MgZnO/AlGaN heterostructure light-emitting diodes.* Applied Physics Letters, 2004. **85**(19): p. 4272-4274.
79. Park, W.I. and G.-C. Yi, *Electroluminescence in n-ZnO nanorod arrays vertically grown on p-GaN.* Advanced Materials (Weinheim, Germany), 2004. **16**(1): p. 87-90.
80. Jeong, M.-C., et al., *Electroluminescence from ZnO nanowires in n-ZnO film/ZnO nanowire array/p-GaN film heterojunction light-emitting diodes.* Applied Physics Letters, 2006. **88**(20): p. 202105/1-202105/3.
81. Hsu, J.W.P., et al., *Directed spatial organization of zinc oxide nanorods.* Nano Letters, 2005. **5**(1): p. 83-86.
82. Masuda, Y., et al., *Site-Selective Deposition and Morphology Control of UV- and Visible-Light-Emitting ZnO Crystals.* Crystal Growth & Design, 2006. **6**(1): p. 75-78.
83. Greene, L.E., et al., *General Route to Vertical ZnO Nanowire Arrays Using Textured ZnO Seeds.* Nano Letters, 2005. **5**(7): p. 1231-1236.
84. Andeen, D., et al., *Lateral epitaxial overgrowth of ZnO in water at 90 Deg.* Advanced Functional Materials, 2006. **16**(6): p. 799-804.
85. Kim, J.H., D. Andeen, and F.F. Lange, *Hydrothermal growth of periodic, single-crystal ZnO microrods and microtunnels.* Advanced Materials (Weinheim, Germany), 2006. **18**(18): p. 2453-2457.
86. Nakamura, S., et al., *InGaN/GaN/AlGaN-based laser diodes with modulation-doped strained-layer superlattices grown on an epitaxially laterally overgrown GaN substrate.* Applied Physics Letters, 1998. **72**(2): p. 211-213.
87. Jang, K.-J. and J.-M. Nam, *Direct-write nanoparticle microarrays for cell assays.* Small, 2008. **4**(11): p. 1930-1935.
88. Barry, R.A., III, et al., *Direct-Write Assembly of 3D Hydrogel Scaffolds for Guided Cell Growth.* Advanced Materials (Weinheim, Germany), 2009. **21**(23): p. 2407-2410.
89. Gratson, G.M., et al., *Direct-write assembly of three-dimensional photonic crystals: conversion of polymer scaffolds to silicon hollow-woodpile structures.* Advanced Materials (Weinheim, Germany), 2006. **18**(4): p. 461-465.
90. Meitl, M.A., et al., *Transfer printing by kinetic control of adhesion to an elastomeric stamp.* Nature Materials, 2006. **5**(1): p. 33-38.

91. Kravchenko, T.A., et al., *The influence of the ion-exchange groups nature and the degree of chemical activation by silver on the process of copper electrodeposition into the ion exchanger.* Electrochimica Acta, 2007. **53**(2): p. 330-336.
92. Sun, M., et al., *Electrodeposition of highly uniform magnetic nanoparticle arrays in ordered alumite.* Applied Physics Letters, 2001. **78**(19): p. 2964-2966.
93. Bera, D., et al., *Palladium nanoparticle arrays using template-assisted electrodeposition.* Applied Physics Letters, 2003. **82**(18): p. 3089-3091.
94. Ohgai, T., et al., *Magneto-sensitive nickel nanowires fabricated by electrodeposition into multi- and single-ion track templates.* Journal of Applied Electrochemistry, 2006. **36**(10): p. 1157-1162.
95. Jaworek, A., A. Krupa, and T. Czech, *Modern electrostatic devices and methods for exhaust gas cleaning: A brief review.* Journal of Electrostatics, 2006. **65**(3): p. 133-155.
96. Kraetschmer, W., et al., *Solid C60: a new form of carbon.* Nature (London, United Kingdom), 1990. **347**(6291): p. 354-8.
97. Iijima, S., *Helical microtubules of graphitic carbon.* Nature (London, United Kingdom), 1991. **354**(6348): p. 56-8.
98. Ebbesen, T.W. and P.M. Ajayan, *Large-scale synthesis of carbon nanotubes.* Nature (London, United Kingdom), 1992. **358**(6383): p. 220-2.
99. Journet, C., et al., *Large-scale production of single-walled carbon nanotubes by the electric-arc technique.* Nature (London), 1997. **388**(6644): p. 756-758.
100. Han, W., et al., *Synthesis of GaN-carbon composite nanotubes and GaN nano-rods by arc discharge in nitrogen atmosphere.* Applied Physics Letters, 2000. **76**(5): p. 652-654.
101. Bera, D., et al., *In-situ synthesis of palladium nanoparticles-filled carbon nanotubes using arc-discharge in solution.* Chemical Physics Letters, 2004. **386**(4-6): p. 364-368.
102. Liu, S.-M., et al., *Synthesis of silicon nanowires and nanoparticles by arc-discharge in water.* Chemical Communications (Cambridge, United Kingdom), 2005(37): p. 4690-4692.
103. Lowell, J. and A.C. Rose-Innes, *Contact electrification.* Advances in Physics, 1980. **29**(6): p. 947-1023.
104. Duke, C.B. and T.J. Fabish, *Charge-induced relaxation in polymers.* Physical Review Letters, 1976. **37**(16): p. 1075-8.
105. Horn, R.G., D.T. Smith, and A. Grabbe, *Contact electrification induced by monolayer modification of a surface and relation to acid-base interactions.* Nature (London, United Kingdom), 1993. **366**(6454): p. 442-3.
106. Xia, Y.N. and G.M. Whitesides, *Soft lithography.* Annual Review of Materials Science, 1998. **28**: p. 153-184.
107. Loo, Y.-L., et al., *Interfacial Chemistries for Nanoscale Transfer Printing.* Journal of the American Chemical Society, 2002. **124**(26): p. 7654-7655.
108. Barry, C.R., J. Gu, and H.O. Jacobs, *Charging Process and Coulomb-Force-Directed Printing of Nanoparticles with Sub-100-nm Lateral Resolution.* Nano Letters, 2005. **5**(10): p. 2078-2084.
109. Fan, Z. and J.G. Lu, *Zinc oxide nanostructures: Synthesis and properties.* Journal of Nanoscience and Nanotechnology, 2005. **5**(10): p. 1561-1573.

110. Yan, H., et al., *ZnO nanoribbon microcavity lasers.* Advanced Materials (Weinheim, Germany), 2003. **15**(22): p. 1907-1911.
111. Hauschild, R. and H. Kalt, *Guided modes in ZnO nanorods.* Applied Physics Letters, 2006. **89**(12): p. 123107/1-123107/3.
112. van Vugt, L.K., S. Ruehle, and D. Vanmaekelbergh, *Phase-Correlated Nondirectional Laser Emission from the End Facets of a ZnO Nanowire.* Nano Letters, 2006. **6**(12): p. 2707-2711.
113. Law, M., et al., *Nanoribbon Waveguides for Subwavelength Photonics Integration.* Science (Washington, DC, United States), 2004. **305**(5688): p. 1269-1273.
114. Leschkies Kurtis, S., et al., *Photosensitization of ZnO nanowires with CdSe quantum dots for photovoltaic devices.* Nano Letters, 2007. **7**(6): p. 1793-8.
115. Levy-Clement, C., et al., *CdSe-sensitized p-CuSCN/Nanowire n-ZnO heterojunctions.* Advanced Materials (Weinheim, Germany), 2005. **17**(12): p. 1512-1515.
116. Soci, C., et al., *ZnO Nanowire UV Photodetectors with High Internal Gain.* Nano Letters, 2007. **7**(4): p. 1003-1009.
117. Ju, S., et al., *Low Operating Voltage Single ZnO Nanowire Field-Effect Transistors Enabled by Self-Assembled Organic Gate Nanodielectrics.* Nano Letters, 2005. **5**(11): p. 2281-2286.
118. Futua, M., et al., *Zinc oxide thin-film transistors (ZnO-TFTs) for active-matrix liquid crystal displays.* Materials Integration, 2006. **19**(10): p. 10-16.
119. Schrier, J., et al., *Optical Properties of ZnO/ZnS and ZnO/ZnTe Heterostructures for Photovoltaic Applications.* Nano Letters, 2007. **7**(8): p. 2377-2382.
120. Wang, X., et al., *Piezoelectric field effect transistor and nanoforce sensor based on a single ZnO nanowire.* Nano Letters, 2006. **6**(12): p. 2768-72.
121. Huang, M.H., et al., *Room-temperature ultraviolet nanowire nanolasers.* Science (Washington, DC, United States), 2001. **292**(5523): p. 1897-1899.
122. Bao, J., et al., *Broadband ZnO Single-Nanowire Light-Emitting Diode.* Nano Letters, 2006. **6**(8): p. 1719-1722.
123. Fan, H., et al., *Self-assembly of ordered, robust, three-dimensional gold nanocrystal/silica arrays.* Science (Washington, DC, United States), 2004. **304**(5670): p. 567-571.
124. Ma, L.-C., et al., *Electrostatic Funneling for Precise Nanoparticle Placement: A Route to Wafer-Scale Integration.* Nano Letters, 2007. **7**(2): p. 439-445.
125. Schutze, A., et al., *The atmospheric-pressure plasma Jet. A review and comparison to other plasma sources.* IEEE Transactions on Plasma Science, 1998. **26**(6): p. 1685-1694.
126. Chang, J.S., P.A. Lawless, and T. Yamamoto, *Corona discharge processes.* IEEE Transactions on Plasma Science, 1991. **19**(6): p. 1152-66.
127. Tendero, C., et al., *Atmospheric pressure plasmas: A review.* Spectrochimica Acta, Part B: Atomic Spectroscopy, 2006. **61B**(1): p. 2-30.
128. Redwitz, M., O. Langenscheidt, and J. Mentel, *Spectroscopic investigation of the plasma boundary layer in front of HID-electrodes.* Journal of Physics D: Applied Physics, 2005. **38**(17): p. 3143-3154.

129. Lenggoro, I.W., H.M. Lee, and K. Okuyama, *Nanoparticle assembly on patterned \"plus/minus\" surfaces from electrospray of colloidal dispersion.* Journal of Colloid and Interface Science, 2006. **303**(1): p. 124-130.
130. Naujoks, N. and A. Stemmer, *Charge patterns as templates for the assembly of layered biomolecular structures.* Journal of Nanoscience and Nanotechnology, 2006. **6**(8): p. 2445-2450.
131. Peters, J., J. Heberlein, and J. Lindsay, *Spectroscopic diagnostics in a highly constricted oxygen arc.* Journal of Physics D: Applied Physics, 2007. **40**(13): p. 3960-3971.
132. Smirnov, B.M., *Physics of Ionized Gases*, ed. H.R. Reiss. 2001, New York: John Wiley & Sons, Inc. 381.
133. Barry, C.R., et al., *Printing nanoparticle building blocks from the gas phase using nanoxerography.* Applied Physics Letters, 2003. **83**(26): p. 5527-5529.
134. Tsai, D.H., et al., *Electrostatic-directed deposition of nanoparticles on a field generating substrate.* Nanotechnology, 2005. **16**(9): p. 1856-1862.
135. Characteristic spectral emission from pure Ar discharges includes red-purple emission peaks at 697nm due to ionization of Ar molecules into Ar+ and 481nm for Ar++, while blue-white O2 discharges contain ionized peaks at 419nm due to O2+ and 646 and 777nm due to the dissociation of the O2 molecule into atomic O. The noble gases that we used to provide an inert environment discussed later (Ar, He) show similar basic arc characteristics and are also known to release electrons by charging to a positively ionized state.
136. High current 100A arc discharges classically referred to as high temperature thermal plasmas or plasma sprays describe a case where the electrons and ions are in thermal equilibrium and sufficiently hot to quickly evaporate the cathode material. However, erosion and the production of nanoparticles has been reported even under corona discharge conditions which sustain much smaller currents, typically less than 500 μA. The input power that we used in the experiments reported here ranged between 1-100W with controlled arc currents of less than 100mA which is quite similar to what is used in atmospheric pressure arc discharge lamps. We anticipate that higher current levels are likely going to work as well.
137. Considering that nanoparticles originate from the grounded cathode and do not deposit on insulating surfaces leads to the conclusions that Coulomb forces dominate the deposition process and that nanoparticles charge to be unipolar prior to deposition on the sample electrode. If neutral particles were present they would coat the insulating surfaces and this is not the case. If the aerosol were to have both positive and negatively charged particles above the sample surface we would again anticipate that the insulating surface would build up a particle layer, contrary to observation. The material flux forming the deposits (F,G) together with the recorded positive ion current and absence of deposition on the insulting surfaces can only be explained if the nanomaterials are predominantly positively charged. Insulating surfaces are initially uncharged and we would expect a limited amount of charged material to deposit until the insulator fully charges. Such deposition is not observed within the ~5 nm resolution limit of our SEM. This behavior can be explained if we consider the higher mobility of gas ions when

compared to nanoparticles. Gas ions such as Ar+ in Figure 3 are likely going to be responsible for establishing an equilibrium charge and potential distribution as the experiment is started. As indicated in Figure 3C Ar+ surrounding the insulator is expected to be responsible for preventing deposition of the positively charged M+ nanoparticles on the insulator.

138. Sheaths regions (purple near cathode and green near anode in Figure 5A) are confined to distances on the order of the Debye length of the high mobility electrons in the system. The anode sheath accumulates a negative space charge dominated by high mobility electrons whereas the cathode sheath is depleted of free electrons yielding a positive space charge region of primarily Ar+ considering the depicted argon plasma situation. We refer to Lichtenberg et al. for detailed calculations of the sheath region at the cathode of an arc discharge lamp. The Debye length is rD = sqrt[(k*epsilon_0/e2)(Te/ne)] where k is Boltzmann constant (8.62 * 10-5 eV/K) and epsilon_0 is permittivity of free space (8.854 * 10-12 F/m), and this electrostatic shielding length depends on the ratio between electron temperature Te and electron concentration ne. The range of possible values is great: ne = 10E16cm-3, Te = 22000K, rD = 200nm are common for a high 6A atmospheric pressure arc whereas ne = 10E8cm-3, Te = 11600K, rD = 0.7mm have been discussed for a lower current corona discharge.
139. Dabringhausen, L., et al., *Determination of HID electrode falls in a model lamp I: pyrometric measurements.* Journal of Physics D: Applied Physics, 2002. **35**(14): p. 1621-1630.
140. Luhmann, J., et al., *Determination of HID electrode falls in a model lamp II: langmuir-probe measurements.* Journal of Physics D: Applied Physics, 2002. **35**(14): p. 1631-1638.
141. Hinds, W.C., *Aerosol Technology*. 2nd ed. 1999, New York: John Wiley & Sons, Inc. 483.
142. Fridman, A. and L.A. Kennedy, *Plasma Physics and Engineering*. 2004, New York: Taylor & Francis Books, Inc. 853.
143. Barry, C.R. and H.O. Jacobs, *Fringing Field Directed Assembly of Nanomaterials.* Nano Letters, 2006. **6**(12): p. 2790-2796.
144. The competition between neighboring areas attracting materials within the Debye radius could in principle affect the deposition rate. However, we have not been able to increase the deposition rate going from a dense pattern to an isolated line which suggests that diffusion plays a role in the observed uniformity.
145. Romay, F.J., B.Y.H. Liu, and D.Y.H. Pui, *A sonic jet corona ionizer for electrostatic discharge and aerosol neutralization.* Aerosol Science and Technology, 1994. **20**(1): p. 31-41.
146. Lichtenberg, S., et al., *The plasma boundary layer of HID-cathodes. Modelling and numerical results.* Journal of Physics D: Applied Physics, 2005. **38**(17): p. 3112-3127.
147. Horn, R., D. Smith, and A. Grabbe, *Contact electrification induced by monolayer modification of a surface and relation to acid-base interactions.* Nature, 1993. **366**(6454): p. 442-3.
148. Xia, Y. and G. Whitesides, *Soft lithography.* Annu. Rev. Mater. Sci., 1998. **28**: p. 153-184.

149. Loo, Y., et al., *Interfacial Chemistries for Nanoscale Transfer Printing.* J. Am. Chem. Soc., 2002. **124**(26): p. 7654-7655.
150. Jacobs, H. and G. Whitesides, *Submicrometer patterning of charge in thin-film electrets.* Science, 2001. **291**(5509): p. 1763-1766.
151. Fudouzi, H., M. Kobayashi, and N. Shinya, *Site-controlled deposition of microsized particles using an electrostatic assembly.* Advanced Materials, 2002. **14**(22): p. 1649-1652.
152. Liang, S., et al., *Micro-patterning of TiO2 thin films by photovoltaic effect on silicon substrates.* Thin Solid Films, 2008. **516**(10): p. 3058-3061.
153. Park, J.-U., et al., *Nanoscale, Electrified Liquid Jets for High-Resolution Printing of Charge.* Nano Letters, 2010. **10**(2): p. 584-591.
154. Barry, C., et al., *Printing nanoparticles from the liquid and gas phases using nanoxerography.* Nanotechnology, 2003. **14**(10): p. 1057-1063.
155. Barry, C., et al., *Printing nanoparticle building blocks from the gas-phase using nanoxerography.* Appl. Phys. Lett., 2003. **83**: p. 5527.
156. Barry, C., J. Gu, and H. Jacobs, *Charging Process and Coulomb-Force-Directed Printing of Nanoparticles with Sub-100-nm Lateral Resolution.* Nano Lett., 2005. **5**(10): p. 2078-2084.
157. Youn, B. and C. Huh, *Surface analysis of plasma-treated polydimethylsiloxane by X-ray photoelectron spectroscopy and surface voltage decay.* Surf. Interface Anal., 2003. **35**(5): p. 445-449.
158. Kim, H., et al., *High-Brightness Light Emitting Diodes Using Dislocation-Free Indium Gallium Nitride/Gallium Nitride Multiquantum-Well Nanorod Arrays.* Nano Lett., 2004. **4**(6): p. 1059-1062.
159. Bhattacharya, S., et al., *Studies on surface wettability of poly(dimethyl) siloxane (PDMS) and glass under oxygen-plasma treatment and correlation with bond strength.* J. Microelectromech. S., 2005. **14**(3): p. 590-597.
160. Langowski, B. and K. Uhrich, *Oxygen Plasma-Treatment Effects on Si Transfer.* Langmuir, 2005. **21**(14): p. 6366-6372.
161. Jacobs, H., et al., *Surface potential mapping - a qualitative material contrast in spm.* Ultramicroscopy, 1997. **69**(1): p. 39-49.
162. Nomura, T., T. Satoh, and H. Masuda, *The environment humidity effect on the tribo-charge of powder.* Powder Technology, 2003. **135-136**: p. 43-49.
163. Nemeth, E., et al., *Polymer tribo-electric charging: dependence on thermodynamic surface properties and relative humidity.* Journal of Electrostatics, 2003. **58**(1-2): p. 3-16.
164. Albrecht, V., et al., *Some aspects of the polymers' electrostatic charging effects.* Journal of Electrostatics, 2009. **67**(1): p. 7-11.
165. Gouveia, R.F., C.A.R. Costa, and F. Galembeck, *Water Vapor Adsorption Effect on Silica Surface Electrostatic Patterning.* Journal of Physical Chemistry C, 2008. **112**(44): p. 17193-17199.
166. Gouveia, R.F. and F. Galembeck, *Electrostatic Charging of Hydrophilic Particles Due to Water Adsorption.* Journal of the American Chemical Society, 2009. **131**(32): p. 11381-11386.

167. Ducati, T.R.D., L.H. Simoes, and F. Galembeck, *Charge Partitioning at Gas-Solid Interfaces: Humidity Causes Electricity Buildup on Metals.* Langmuir, 2010. **26**(17): p. 13763-13766.
168. Wainright, S.P., S. Hall, and D. Flandre, *The effect of series resistance on threshold voltage measurement techniques for fully depleted SOI MOSFETs.* Solid State Electron., 1996. **39**(1): p. 89-94.
169. As electrets we tested polymethylmethacrylate (PMMA), polyacrylic acid (PAA), polystyrene (PS), MicroChem (SU-8) 2010 photoresist, and silicon dioxide (SiO2). All polymers were spin-coated and baked according to standard procedures to produce thicknesses on the order of 100-200 nm except for the SU-8 resist, which was approximately 10 mm thick. The SiO2 substrates (160 nm thick) were generated by dry thermal oxidation.
170. Youn, B.-H. and C.-S. Huh, *Surface analysis of plasma-treated polydimethylsiloxane by X-ray photoelectron spectroscopy and surface voltage decay.* Surface and Interface Analysis, 2003. **35**(5): p. 445-449.
171. Kim, H.-M., et al., *High-Brightness Light Emitting Diodes Using Dislocation-Free Indium Gallium Nitride/Gallium Nitride Multiquantum-Well Nanorod Arrays.* Nano Letters, 2004. **4**(6): p. 1059-1062.
172. Bhattacharya, S., et al., *Studies on surface wettability of poly(dimethyl) siloxane (PDMS) and glass under oxygen-plasma treatment and correlation with bond strength.* Journal of Microelectromechanical Systems, 2005. **14**(3): p. 590-597.
173. Langowski, B.A. and K.E. Uhrich, *Oxygen Plasma-Treatment Effects on Si Transfer.* Langmuir, 2005. **21**(14): p. 6366-6372.
174. Jacobs, H.O., et al., *Surface potential mapping - a qualitative material contrast in spm.* Ultramicroscopy, 1997. **69**(1): p. 39-49.
175. *XPS studies done by Uhrich et al show small amounts of PDMS on the surface of plasma treated PMMA after contact with plasma treated PDMS but not on untreated PMMA.*
176. For a double layer separated by a distinct distance d, the charge density σ can be calculated with $\sigma = \varepsilon(\Delta V/d)$, where ε is the permittivity, and ΔV is the voltage drop across the layer. For $\varepsilon = 2 \times 10\text{-}11$ C/Vm (relative permittivity of PMMA), $\Delta V = 2$ V (measured potential change), and d = 200 nm (assumed intermediate distance between the counter charges), we obtain a first order estimate of the effective charge density of $\sigma_{eff} = 12.5$ elementary charges per surface area of 100 nm x 100nm. The exact number depends on the actual distribution of the charges on the PMMA film and the Si substrate.
177. The image charges flow from the ground through the electrometer into the metallic plates. A sufficient separation, > 15 cm for 1 cm sized chips, between the two materials after contact ensures a correct charge reading. Accurate force distance measurements required the disconnection of the electrometers before contact in order to eliminate any possible change in the plate charge due to electron flow associated with the image charges.
178. Hillborg, H. and U.W. Gedde, *Hydrophobicity changes in silicone rubbers.* IEEE Transactions on Dielectrics and Electrical Insulation, 1999. **6**(5): p. 703-717.

179. Casse, M., et al., *Gate-induced floating-body effect in fully-depleted SOI MOSFETs with tunneling oxide and back-gate biasing.* Solid State Electron., 2004. **48**(7): p. 1243-1247.